SYNCHRONY AND CHAOS IN COUPLED OSCILLATORS AND NEURAL NETWORKS

A Dissertation

Submitted to the Graduate School
of the University of Notre Dame
in Partial Fulfillment of the Requirements
for the Degree of

Doctor of Philosophy

by

Sridhar Raghavachari, M.Sc., B.E.

James A. Glazier, Director

Department of Physics
Notre Dame, Indiana
March 1999

SYNCHRONY AND CHAOS IN COUPLED OSCILLATORS AND NEURAL NETWORKS

Abstract

by

Sridhar Raghavachari

This disssertation studies the dynamics of ensembles of coupled, dynamical elements with discrete and continuous time dynamics. Specific problems include the appearance of synchronous behavior in an ensemble of dynamical elements.

We show that the dynamics of coupled map lattices with connectivity that scales with inter-site distance exhibit a transition from spatial disorder to spatially uniform temporal chaos as the scaling is varied. We investigate the eigenvalue spectrum of the stochastic matrix characterizing fluctuations from the uniform state numerically and show that the spectrum is bounded,real and the largest eigenvalue (corresponding to the uniform solution) has a gap separating it from the remaining N-1 eigenvalues which correspond to non- uniform solutions. The width of this gap depends on the scaling exponent. We relate the stability of the uniform state with this gap and show that the state is globally stable even in a strongly chaotic region of the uncoupled map.

Bursting is a prototypical pattern of voltage oscillations of membrane potentials of biological cells, where the membrane potential alternates between fast oscillations and a slow drift. These complex oscillations arise as a result of interactions between the kinetics of fast and slow ion channels. While bursting in isolated cells is well understood, the study of populations of interacting bursters is less developed. We

study a one-dimensional continuum model of bursting and show that synchronous bursting is extinguished by a spatial wave of bursting separating active and quiescent cells when the coupling is weak. This result places bounds on the measured values of coupling strength between secretory cells in the pancreas.

Rhythmic behavior in animals, such as locomotion, digestion and respiration is controlled by the interactions of cellular and synaptic mechanisms acting on several time scales. We explore a simple rhythmic circuit model with two cells reciprocally inhibiting each other with fast and slow time scale inhibition. The interaction between the fast oscillations of the cells and the slow inhibition results in a complex pattern of bursting. This form of bursting originates from a network interaction, as isolated cells can only oscillate but not burst. This result is useful in understanding the design of central pattern generators in invertebrates where multiple time scale inhibition is common.

To my parents and Arpita.

CONTENTS

FIGURES

ACKNOWLEDGEMENTS

I am most grateful to my supervisor, Dr. James A. Glazier, for his encouragement, patience and latitude that he has allowed me in pursuing different areas of research.

I thank my committee for their painstaking scrutiny of this thesis and their invaluable comments. I deeply appreciate Dr. Gerald Jones, who taught me how to ask the right questions and contributed vitally to my develpment as a scientist. I acknowledge Burk and Rob for all the coffee breaks that kept me going in the last stages, and all the non-scientific discussions that kept things in perspective. I thank John Lisman, for his faith in my abilities as a researcher, and giving me a job. Graduating would not have been the same without one.

CHAPTER 1

INTRODUCTION

The subject of coupled dynamical elements has a rich and impressive history, impinging upon diverse fields as physics, chemistry, neurobiology and engineering. Christian Huygens [4] made the first recorded observation of two interacting oscillators, who noted that the pendula of two nearby clocks tended to synchronize in an antiphase, locked state, and returned to the locked state even after one pendulum was slightly perturbed. The clocks gradually drifted apart when moved to opposite sides of the room. Huygens concluded that the clocks must be coupled through small vibrations in the wall, and that the weak coupling allowed the clocks to frequency lock. However, we must distinguish between frequency locking, in which oscillators of different frequency establish an exact rational frequency ratio, but the relative phase can drift, and phase locking of identical oscillators, in which they oscillate in a fixed phase relation to each other.

Examples of oscillatory behavior abound in biology, from unicellular to multicellular organisms, with periods ranging from fractions of a second (neural rhythms) to years (oscillations in the populations of predators and prey) [5]. Oscillations can be simple, periodic or quasiperiodic. Oscillators in chemistry and biology have complex bursting patterns, with successive alternations between high frequency oscillations and quiescence. Finally, oscillations can be aperiodic or chaotic, with extreme sensitivity to initial conditions. Neurons and other biological oscillators communicate

with other oscillators through a variety of means. Thus, an understanding of coupled oscillators is vital to understand the dynamics of biological processes. The theory of nonlinear dynamical systems has helped provide a bridge between extremely detailed, mechanistic models that take into much of the known facts and data, and high level, canonical models, that although simpler, capture some essential features of the more comprehensive models, and in some cases, can be rigorously derived from the former, and allow analytic exploration of the dynamics.

We begin with a simple, interacting nonlinear dynamical system, the coupled logistic map. Most studies hitherto have focused on the characterization of dynamics in locally, (k-nearest neighbor connected) models or a mean field version of local models, the globally coupled model. The interactions in biological examples of coupled dynamical elements, such as the nervous systems of organisms or even the synchronous flashing of fireflies, have much randomness in their coupling topologies. Randomness notwithstanding, the coupling in naturally occurring populations is constrained by geometry and structural considerations. The coupling is sparse, with most elements connected to only a small fraction of the total number. Moreover, the network is spatially structured, constraining the majority of interactions to some local neighborhood. We introduce a sparse coupling scheme where the probability of connection decays with distance between the elements to study the effects of structured randomness on the collective behavior of dynamical elements in Chapter 2. The locally connected model and the mean field model are recovered as limiting cases of our coupling scheme.

The rhythmic output of secretory cells is critical for release of hormones that maintain the biochemical makeup of the body within a safe operating range. The β-cells in the pancreas, for example, release insulin in response to blood glucose. The electrical activity of the β-cells is a prototypical bursting pattern. Islets in

the pancreas are made up of large assemblies of coupled bursters. What are the dynamics of coupled bursters? We turn to this question in Chapter 3 and apply singular perturbation methods to answer this question and extend insights gained from networks of two coupled bursters to a large, spatially extended field of bursters. We use simple, canonical models, rather than specific biophysical ones to illustrate generic features of the dynamics.

How does a small insect like a centipede move its legs in a coordinated manner? How does a locust fly? What maintains the rhythm of our heartbeat? All these questions are different versions of the same underlying question: What controls the highly coordinated, rhythmic activity of animals? While the implementations differ in detail, some basic principles of control of rhythmic behavior have emerged. In vertebrates, rhythmic motor activity is controlled by large numbers of neurons making it hard to analyze in detail. Extensive experiments on invertebrate neural networks [6] have revealed simpler, smaller (10s of neurons) networks called Central Pattern Generators that are at the heart of motor pattern generation.

Neurobiologists have made enormous progress in identifying the intrinsic and network properties of CPGs and their component neurons. Further, they have related the cellular processes to their behavioral correlates. Nonlinear dynamics can help answer the question: how does the network generate a particular rhythm, given its component circuitry? Neurons are out-of-equilibrium systems with many degrees of freedom, and coupled neurons are even more complicated. Thus, for the sake of tractability, researchers often make several simplifying assumptions for their models. We study a network of two coupled, biophysically modeled neurons and show the existence of a striking, temporal pattern, which would be missed in a simplified model.

CHAPTER 2

COUPLED LOGISTIC MAPS

2.1 Introduction

The study of the collective behavior of large numbers of interacting elements has a rich history and such arrays occur in a variety of contexts in nature. The elements may be identical or have slightly different dynamics (due to a statistical spread of parameter values). A common theme is that the interactions among the elements cause the ensemble to self-organize into well-defined collective behaviors. Phase transitions in statistical mechanics are familiar examples of self-organization, where a macroscopic quantity, called the order parameter, assumes non-zero values continuously or discontinuously, under a smooth shift of parameters. A well defined free energy functional characterizes thermodynamic models and their collective states minimize the free energy. In essence, the dynamics determine how they approach these equilibrium free energy states. In contrast, we consider models which break the time translation invariance characteristic of equilibrium models. Such nonequilibrium models are dissipative and require sustained energy input to maintain nontrivial dynamics.

An extreme form of collective behavior is synchrony, where a large fraction of the elements behave identically. We can best obtain theoretical understanding of collective rhythmicity by studying the conditions of its onset. In the language of statistical mechanics, we can consider the onset of synchrony as a phase transition

from a disordered to an ordered state. We will consider the dynamics of populations of identical dynamical elements and study the effect of connectivity on the appearance of synchrony and of other, loosely defined, macroscopic order.

2.2 The Iterated Logistic Map

May [7] introduced the iterated logistic map as a simple model for the dynamics of predator-prey populations. It has become the canonical example of a nonlinear dynamical system that exhibits chaos. Just as the Ising model is a simplified model that has had enormous impact on the study of phase transitions, the logistic map has provided fundamental insight into aspects of the mathematical theory and the numerical methods relevant to deterministic chaos. In fact, a large proportion of chaotic phenomena in high dimensional models is already observable in the logistic map. The properties of the map are *universal*. Any C^1 unimodal map of the interval has the identical sequence of bifurcations and scaling of the parameter a for successive period doublings.

The most familiar version of the map is given by the following difference equation:

$$x_{n+1} = f(x_n) = 1 - ax_n^2, \tag{2.1}$$

where the index n represents the time step, and a is a parameter. Starting from a value $x_n \in I = (-1, 1)$, the nonlinear function $f(.)$ generates a number in I, *i.e.* it maps the interval into itself. A plot of the limiting behavior of the x_n for various values of a is usually referred to as a bifurcation diagram (Fig. 2.1). As the parameter a increases, the long-time behavior of the logistic map iterates become chaotic after successive period doublings. The period doubling route to chaos is one of several generic mechanisms by which the time evolution of a deterministic system becomes chaotic.

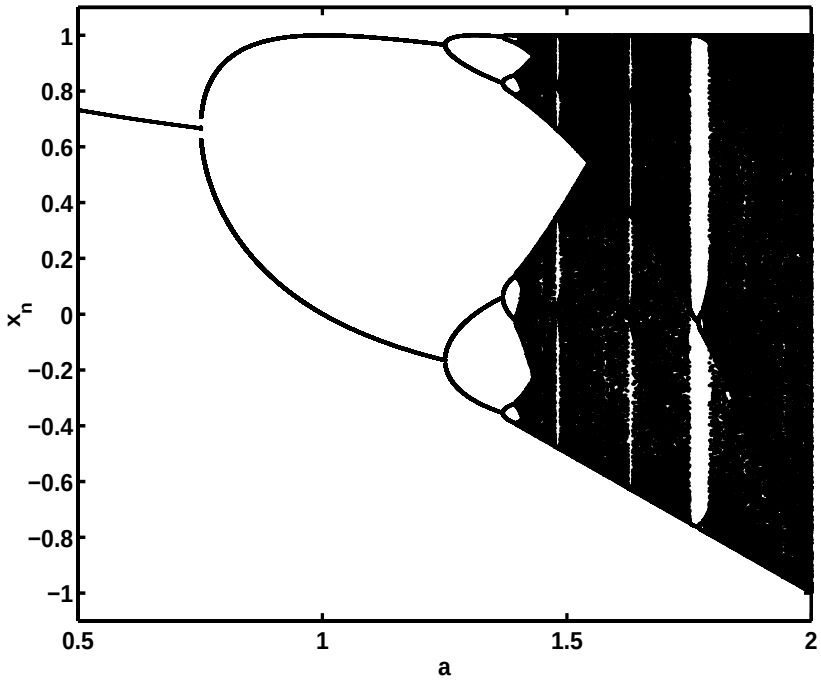

Figure 2.1. Bifurcation diagram of the logistic map showing the period doubling route to chaos

While the dynamics of 2.1 is interesting in its own right, it may be puzzling as to how the properties of one variable maps are relevant to continuous time, ordinary differential equations such as:

$$\frac{d\mathbf{x}}{dt} = F(\mathbf{x}, \mu), \tag{2.2}$$

where μ is a set of parameters, $F(.;.)$ is a smooth, differentiable nonlinear function (*i.e.* it is continuous and several times differentiable for all values of its arguments), and $\mathbf{x}(t)$ is a vector in $\mathbb{R}^d$. As μ varies, Eqn. 2.2 may undergo a series of abrupt changes in its long time behavior, called bifurcations. If $F(.;.)$ is strongly nonlinear, analytic solutions are hard to find, and we must resort to numerical techniques to classify the behavior of Eq. 2.2. A powerful technique is the concept of a Poincaré section, which is a stroboscopic projection of the time evolution of $\mathbf{x}(t)$. We construct a Poincaré section by recording as a time series, the values $\mathbf{x}(t)$ at time instants when $\mathbf{x}(t)$ crosses a (hyper)plane where a coordinate x has some fixed value. This method of observation reduces the continuous flow to a discrete time trace in a $d-1$ dimensional space, thereby reducing the dimension of the problem by one. We can now implicitly define a $d-1$ dimensional map f, (the first return map) of the $d-1$ dimensional hyperplane onto itself as $\mathbf{x}_{i+1} = f(\mathbf{x}_i)$. The dynamics and bifurcations on this $d-1$ dimensional subspace are strictly equivalent to the dynamics in the full d dimensional space (for almost all choices of the Poincaré section plane). Notice that the original continuous time equations now reduce to discrete time equations. So, for example, a periodic orbit of the full N dimensional equations reduces to a single point and doubly periodic motion with commensurate frequencies reduces to a finite set of points. Quasiperiodic motion becomes a dense curve and chaotic trajectories transform to a cloud of points by an appropriate choice of the sectioning hyperplane.

The choice of the sectioning plane depends on the dynamics. Hamiltonian systems have at least one conserved quantity, the energy, which restricts the motion to a $2N-1$ dimensional surface. The Poincaré section can be chosen so as to fix a value for the kinetic or potential energy. Additional conserved quantities result in further reduction of the full equations. The resulting map is often called a symplectic map when the equations are written in terms of action-angle variables [8]. This reduction technique is very useful in the study of Hamiltonian chaos. Dissipative dynamical systems do not conserve energy, and therefore the choice of the section plane depends on the details of the dynamics.

The Poincaré section technique allows us to relate the discrete time nature of the map to the continuous time evolution of the ODEs. An early example of this procedure can be seen in Guckenheimer's study of the Lorenz equations [9], where he reduced the 3 dimensional flow of the Lorenz equations to a one dimensional quadratic return map[1]. The Lorenz map correctly captures the sensitivity to initial conditions of the Lorenz equations, although, being a projection of a 2 dimensional Poincaré section, it misses important features of the ODEs. Several excellent books review iterated maps [10, 11].

Most physical systems of interest, however, also have spatial degrees of freedom, and are more appropriately described by partial differential equations (PDEs) which are continuous time, continuous space equations that in principle, are infinite dimensional. The Navier-Stokes equation for fluid motion is a familiar example. Fluid motion in experiments such as Rayleigh-Bénard convection (a very simplified model for atmospheric turbulence) is usually described by an appropriate reduction of the Navier-Stokes equation. Experiments on a fluid layer in a closed conducting box heated from below, show the following: initially, a small temperature difference

[1]Strictly speaking, the Lorenz map is only a 1-dimensional projection of the 2 dimensional Poincare map obtained from the original equations

between the top and bottom plates establishes a linear gradient of temperature (conducting state) as the thermal diffusion in the motionless fluid balances the buoyancy of the heated fluid. As we increase the temperature difference between the plates, an instability sets in at a threshold value, T_c, and the fluid begins to move, breaking the continuous translation invariance of the temperature field, forming rolls with an approximate wavelength selection.

Close to the onset of an instability which breaks a continuous symmetry such as translation invariance, the behavior of macroscopic quantities such as the temperature or velocity fields can be reduced to so-called amplitude equations by perturbative techniques [12]. These amplitude equations are a coarse grained description of the space-time evolution of macroscopic quantities, and the analysis of these equations has become a veritable industry in the last 30 years. The nonlinearity of these equations often makes their analysis rather complicated, underscoring the need for simpler models that have the same qualitative behavior as the amplitude equations. Substantial progress can be made if the infinite dimensions of the PDE can be approximated by ODEs or maps in some small finite number of dimensions. Can we construct a Poincaré map for the partial differential equations of fluid dynamics? Although no systematic procedure for doing so exists, Kaneko [13] proposed a phenomenological model combining the discrete time nature of the Poincaré map with discrete spatial degrees of freedom. The Coupled Map Lattice (CML) is a simple example of a discrete, spatially extended dynamical system, which captures the essential features of more complicated continuum models. The CML models spatially extended dynamics according to the following steps:

- Choose a set of macroscopic field variables on a lattice (*e.g.* the velocity or temperature field in a fluid or the chemical concentration in a chemical reaction). Choose the dimension and topology of the lattice to correspond to

the actual physical situation.

- Decompose the processes governing the dynamics of the field variables into independent components (diffusion, reaction, convection, *etc.*). The dynamics now consist of a local, nonlinear transformation in time (corresponding to reaction terms) of the field variables with coupling terms from among suitably chosen neighbors (corresponding to diffusion).

- Update the dynamics in parallel over the lattice.

The simplest realization of the above procedure is local nonlinear dynamics along with spatial diffusion. The equation for the CML in 1 dimension is:

$$x_{n+1}(i) = (1-\epsilon)f(x_n(i)) + \frac{\epsilon}{2}\left[f(x_n(i+1)) + f(x_n(i-1)) - 2f(x_n(i))\right], \qquad (2.3)$$

with $f(.)$ given by Eq. 2.1. Thus, by construction, the CML provides a systematic way to increase the number of degrees of freedom and systematically approach the thermodynamic limit of an infinite system. Implicit in this definition of diffusion are the discrete time steps of the logistic map. The CML can be seen as an approximation of a set of continuously coupled ODEs, where the coupling terms only act at iT, for integer i, where T denotes some basic period of the underlying ODEs. Hence the choice of coupling terms in CMLs has the form shown in Eqn. 2.3 instead of $f(x_n(i+1) + x_n(i-1) - 2x_n(i))$, which is the finite difference approximation to ∇^2.

The dynamical equations for the N lattice sites resemble a discrete version of the familiar amplitude equations for fluid instabilities such as the Complex Ginzburg-Landau equation:

$$\partial_t A(x,t) = \mu A(x,t) + (1+ic_1)\nabla^2 A(x,t) - (1+ic_2)|A(x,t)|^2 A(x,t), \qquad (2.4)$$

where $A(x,t)$ is a complex amplitude which describes the temperature field in a convection experiment, near the onset of an instability of the uniform state. The

parameter μ controls the onset of the instability and c_1 and c_2 represent the strengths of diffusive and nonlinear interactions respectively. The Ginzburg-Landau equation is a partial differential equation with space, time and the complex amplitude taking on continuous values. In contrast, the CML discretizes both space and time, while the field variable x takes on continuous values in a specified interval.

Since the logistic map is a discrete time, discrete space map, the CML can be viewed as a Poincaré mapping of a partial differential equation. The discrete nature of the CML makes it more amenable than the CGL equation to numerical simulations and analysis. With diffusive interactions between the maps, the lattice captures many qualitative features of amplitude equations for disordered behavior in fluids and chemical reactions, such as wavelength selection, intermittency and spatiotemporal chaos, even though the parameters of the CML do not directly relate to the parameters of the experiments.

Since some combination of elementary local dynamics and diffusive interactions describes diverse dynamical behavior in spatially extended models, the formalism of CMLs can model many physical phenomena. Kapral has modeled pattern formation in chemical reactos using time-discretized models of chemical reactions such as Brusselator kinetics [14] to study front propagation and spiral wave formation. Oono and Puri [15] have proposed CMLs for spinodal decomposition, which is traditionally studied using the kinetic Ising model. Miller and Huse have studied a nonequilibrium phase transition between two chaotic states [16] in a CML. Several groups have studied open flow models using a unidirectionally coupled CML (reviewed in [17]). Below, we briefly discuss the dynamics and patterns for CMLs with the quadratic (one hump) logistic map coupled locally, globally or randomly according to a distance dependent probability. These results should apply to any C^1, unimodal CML.

2.2.1 Locally Coupled Logistic Maps: Dynamics

The local CML is a discrete time, discrete space version of an amplitude equation. Each site communicates with nearest neighbors and the logistic map describes the local dynamics. In contrast to amplitude equations, where the local dynamics is periodic, and spatiotemporal chaos arises from the interaction of several spatial modes, the local dynamics of the uncoupled sites is chaotic, and the overall behavior arises as a competition between the smoothing induced by diffusion and the local chaos of the map. We briefly list some of the characteristic dynamics of local CMLs in one dimension. A more complete review is given in [13].

The relevant parameters are the nonlinearity, a, and the diffusion strength, ϵ. In the period-doubling regime of the local map, most initial conditions lead to a domain state, where each domain corresponds to a different phase of the same periodic orbit. The domain boundaries do not move with time. As the local map period-doubles, the domain sizes grow smaller and their oscillations period-double in time *i.e.* a structure with smaller wavelength is selected. Past the accumulation point, a_∞, (where an orbit of infinite period for the single map becomes stable), motion in large domains becomes chaotic, while smaller domains still remain periodic with period 2^n, n small. This state is called the frozen random phase. For further increase in a, wavelength selection splits large, chaotic domains. The resulting structure is less chaotic than the frozen random phase, *i.e.* a less chaotic pattern is selected.

As a increases further, a zig-zag pattern with wavelength 2 becomes stable, with adjacent lattice sites oscillating in different phases. Random initial conditions can result in small defects in the zig-zag pattern. The temporal evolution within the defects is chaotic, while the rest of the lattice evolves periodically. These defects move diffusively but remain localized in space. Further increase in a results in an increase in the number of defects until the whole lattice becomes turbulent.

Values of a in a periodic window result in a curious spatiotemporal state. The temporal evolution of any single site alternates irregularly between *laminar*, or periodic and *turbulent* or chaotic regimes, with large patches of turbulent sites in a sea of laminar sites. This phase is known as spatiotemporal intermittency. Intermittent behavior has been observed in many physical experiments on fluid convection, electric convection of liquid crystals, Faraday instability of a liquid surface, and lasers and is thought to be an important route to chaos in spatially extended systems [12]. Spatial correlation functions decay algebraically in the spatiotemporally intermittent regimes.

As a approaches 2, the lattice becomes spatiotemporally chaotic. However, unlike the single logistic map, where the chaos is structurally unstable because of the presence of many periodic windows. Small changes of parameters in the chaotic regime $[a_\infty, 2]$ result in periodic behavior, *i.e.*, if for a given value of a, the orbit is chaotic in time, the orbit is periodic in any ε neighborhood of a, no matter how small ε may be. For example the logistic map has a period 3 window in the chaotic region which can be seen in Fig. 2.1. The chaos in the CML is sustained in parameter space. We might expect that spatiotemporal chaos is transient and that eventually the lattice must fall into a time periodic, spatially homogeneous state, corresponding to the periodic windows of the logistic map. Numerical experiments show that the length of transients exponentially increases with the lattice size, and in fact, even for moderately sized lattices ($N \sim 10$), the dynamics never approach the homogeneous phase, indicating that chaos might indeed be sustained in time and might never approach the periodic attractor.

2.2.2 Globally Coupled Logistic Maps

A different limiting case for the CML takes the interaction range to be infinite, the limit of global coupling. Globally coupled models arise naturally in several physical situations. Global feedback in Josephson junction arrays [18], charge density waves in solids under a constant current [19], mode coupling in lasers through an energy source [20], and rapid gas diffusion in surface reactions [21] are some examples where long ranged (global) coupling controls the dynamics. These examples are *not* the mean field limit for some suitably long-ranged coupling, but are globally coupled due to physical constraints. Given their practical applications, the study of globally coupled models is of extreme importance. The globally coupled CML is given by the equation:

$$x_{n+1}(i) = (1-\epsilon)f(x_n(i)) + \frac{\epsilon}{N}\sum_{j=1}^{N} f(x_n(j)), \tag{2.5}$$

where the terms are as before. This model has two tendencies: the mean field action tends to synchronize and local chaos tends to desynchronize the elements. If the former wins, the elements order in a coherent state, while if the latter wins, the elements behave incoherently. We make this idea more precise as follows: The simplest attractor is a synchronous state, where $x(i) = x(j),\ \forall\ i,j$. The single logistic map $x_{n+1} = f(x_n)$ governs the motion at each site. We calculate the stability of this state by following the evolution of infinitesimal perturbations $e_i(n)$ from the synchronous state:

$$e_{n+1}(i) = f'(x_n)\big[(1-\epsilon)e_n(i) + \frac{\epsilon}{N}\sum_{j=1}^{N} e_n(j)\big]. \tag{2.6}$$

The eigenvalues of the matrix $\mathbf{J}_n = f'(x_n)[(1-\epsilon)\mathbf{I} + (\epsilon/N)\mathbf{D}]$, where $\mathbf{I}$ is the identity matrix and $\mathbf{D}$ is a constant matrix whose elements are 1, determine the

linear stability of Eqn. 2.6. Since the matrix is highly symmetric, we obtain the following eigenvalues $\lambda_1 = \Pi_{i=0}^{n} |f'(x_n)| = \rho_0$, and $\lambda_j = \rho_0(1-\epsilon)$, $j = 2 \cdots N$ ($N-1$-fold degeneracy). The perturbations, $e_n(j)$ grow if the eigenvalue $\lambda_j > 1$. The eigenvector corresponding to λ_1 is $(1, 1, \cdots, 1)^T$, and any perturbations along this eigenvector do not destroy the coherent state. Thus the stability condition for the uniform state is $|\rho_0(1-\epsilon)| < 1$.

Kaneko [22] first studied this model, and showed that *clustering* is a generic feature of its dynamics. In a clustered phase, the elements $x(i)$ tend to evolve synchronously within a cluster, and different clusters are independent. As the non-linearity, a, or the coupling strength, ϵ, varies, the lattice can undergo successive transitions from a 1-cluster (synchronous) state to an ordered phase with a few large clusters, a partially ordered states with a few large clusters and several small clusters to an incoherent, turbulent phase with $\mathcal{O}(N)$ clusters. Cluster states are attracting and highly degenerate. Once the lattice falls into a cluster state, it remains there for all time. As an illustration, consider the case of a two cluster state. The fraction of elements in the two clusters are N_1 and N_2 such that $\frac{N_1}{N} + \frac{N_2}{N} = 1$. Clearly, any choice of N_1 and N_2 is allowed, but only a few, perhaps one, are stable. Thus, the two cluster state is degenerate, with more than one stable partitioning of the lattice. In the ordered phase, the GCM has a large mulitiplicity of cluster states, and a small amount of noise applied even at a single site can switch the macroscopic state of the lattice, indicating the multistability of the clusters. Kaneko has suggested [23] that the large multiplicity of attracting cluster states and the possibility of switching between them may allow the GCML to model memory.

The GCML possesses several symmetries. The global coupling introduces a permutation symmetry (symmetry group $\mathcal{S}_n$) in the dynamics, *i.e.* the dynamics are invariant under a permutation of the indices of the elements. Any limiting solution

of the GCML must satisfy these symmetries. One such solution is the turbulent phase with exactly N clusters of size 1 and the single cluster (synchronous) state is another. The permutation symmetry implies the existence of such solutions, but says nothing about their stability. When this symmetry breaks, solutions of lower symmetry bifurcate from the maximally symmetric solutions [24]. In this case, cluster states still obey limited permutation symmetry over the number of elements in the given cluster.

An analysis similar to that for the synchronous state determines the linear stability of cluster states, but now the analysis must include two types of perturbations: those that destroy coherence within a cluster, and those that destroy the k cluster states. Group theoretic methods that use the permutation symmetery of the equations can determine the stability of various states, but we are not aware of the use of these methods to analyze discrete time systems such as the GCML.

In summary: the GCML is a model system with local chaos and global feedback. Suggestive analogies with neurobiology have inspired substantial interest in the cluster states of the GCML. Experiments on cats and monkeys [25, 26] have shown that in the primary visual cortex (the first area in the mammalian brain which processes visual stimuli as pixel images) the membrane potentials of the neurons tend to oscillate at an approximate 40 Hz frequency. Assemblies of phase locked neurons oscillating at this basic 40 Hz rhythm represent features of an object in a scene. Ensembles of neurons which maintain fixed phase differences with each other encode different objects in a scene. The phase locked groups change dynamically with the scene. The dynamic clustering of neurons into different phase locked groups representing various objects in the visual field has been proposed as a mechanism for *feature binding* througout the cortex [26]. Clustering in the GCML or any globally coupled dynamical system has been proposed as models for "clustering "of phase

locked neural assemblies in the brain. However, these analogies have to be taken with caution. Clustering, and many other properties of the GCML, result from its various symmetries, which are in general not present in a network of neurons. In fact, at the level of connectivity, a randomly connected model is more representative of neural connectivity. We explore the dynamics of a model of randomly coupled logistic maps in the next section.

2.3 Fractal CML

Mammalian brains are complex networks of elements (neurons) that can perform a broad variety of information processing tasks. It is clear that the population activity of large assemblies of cells in the vertebrate brain is responsible for sensory processing, motor response and cognition. Several features such as the anatomy and physiology of the neurons, the types of connections between the neurons (excitatory or inhibitory) or the architecture of the network could determine the dynamics of the cell assemblies.

Recent studies have furthered our insights into the macroscopic organization of the cortex. Felleman and van Essen [27] review the overall pattern of connectivity of various modules of the visual cortex. On a microscopic level, extensive studies of interconnectivity in the cortex show that the cerebral cortex is best represented by a sparsely connected, spatially structured network [28].

The volume of the brain imposes physical constraints on the connectivity. The volume of wiring should not be a substantial fraction of the total available volume. In fact, it is possible that the specialization of cortical regions into functional modules in larger brains is a direct result of minimizing the wiring volume [29]. The total number of neurons in the human cortex is about 10^9, and each neuron receives about 10^4 connections. Thus, a sparse random network might best represent

cortical connectivity. However, this picture is obviously incomplete. A sparse random graph has no metric structure, while a brain certainly does. Nearby neurons or modules connect with higher probability than distant ones [30]. Several studies have shown that neuronal branching is fractal [31, 32, 33] (*scale invariant*) over some range. Since fractal, branching structures are rather wispy, the dendritic and axonal branching of N neurons in a volume can interpenetrate freely. This immediately leads us to a *scale invariant* model of cortical connectivity. The neurons are distributed in a d dimensional volume. The connectivity $C(\mathbf{r})$ scales as $\mathbf{r}^{-\alpha(\mathbf{r})}$. The finite size of neuronal arborization determines the functional dependence of α. If the $\alpha(\mathbf{r})$ is such that for small $\mathbf{r}$, connectivity is $\mathcal{O}(N^2)$, implying tight connectivity, while for large $\mathbf{r}$, it is of $\mathcal{O}(N)$, indicating sparse connectivity, we can naturally build up a network that is modular, even though the modules themselves are not prewired. Scale invariant connectivity implies that the crossover between tight and loose coupling is gradual, with no preset length scale. The simplest scenario would take $\alpha(\mathbf{r})$ to be constant. Obviously, substantial experimental work is required to verify this picture in a real cortex. Typical values for α are in the range of 1.2-1.8.

We can however, ask the following question: how does the scale invariant connectivity of a network of dynamical elements affect its time evolution? Chaotic maps like the logistic map capture some essential features of neuronal dynamics such as fixed point, oscillatory, or chaotic behavior [34], depending upon the applied stimulus, and thus are a simple model to study network dynamics with scale invariant connectivity.

We consider a CML with local dynamics at a lattice site on a one dimensional chain described by Eqn. 2.1. Each pair of sites, i, and, j, connect according to the probability distribution:

$$\rho(C_{ij}) = p(ij)\delta(C_{ij} - 1) + (1 - p(ij))\delta(C_{ij}), \tag{2.7}$$

where $p(ij)$ is given by a simple scaling assumption for the connection neighborhood:

$$p(ij) = C|\mathbf{r}_i - \mathbf{r}_j|^{-\alpha}, j = \pm 1, \pm 2 \cdots, \tag{2.8}$$

where $\mathbf{r_i}$ and $\mathbf{r_j}$ are the coordinates of the i^{th} and j^{th} sites respectively, and C is a normalization constant. This form of connectivity differs from random connectivity models with a fixed value of $p(ij)$. The probability that two sites are connected depends on the inter-site distance. The number of connections in a d-dimensional sphere of radius R will scale as $R^{d-\alpha}$ (for large enough lattices), which we define as *fractal* connectivity. The coupled lattice is thus given by:

$$x_{n+1}(i) = \frac{1}{A_i + 1}\big[f(x_n(i)) + \sum_{j \epsilon conn} f(x_n(j))\big], \tag{2.9}$$

where A_i is the number of connections at the i^{th} site, and the sum over j runs over all the sites connected to site i. We have three parameters at our disposal: a, the nonlinearity parameter; α, which defines the connection neighborhood, and A which sets the strength of the interaction between sites.

We impose periodic boundary conditions on the lattice, *i.e.* $x(1) = x(N+1)$. The form of the probability distribution for site-site coupling allows us to smoothly vary the interaction neighborhood of a site. Thus, $\alpha \to \infty$ is the nearest-neighbor coupling limit, and $\alpha \to 0$ is the global coupling limit (see sections 1.2.1 and 1.2.2). The $\alpha = 0$ limit is actually singular, because the permutation symmetry of the dynamical equations of the GCML is only valid at the limit, whereas for any small value of α, the lattice is not symmetric to an interchange of indices. We are mainly concerned with the study of the lattice dynamics for α values of $\mathcal{O}(1)$. For these α values, the coupling between sites is no longer strictly short range or infinite range. This kind of scaling of the connectivity occurs in animal brains and the particular range of values of α results in rather dilute connectivity which is biologically realistic [30].

We show the temporal evolution of the lattice in Figure 2.2, for a lattice of size 100 with the value of the map parameter, a, set to the band periodic region of the logistic map (a=1.44). We see that the lattice splits into almost periodic domains for large α (local limit) (panel a) which select some characteristic stable wavelength. The domain boundaries do not move with time. This state is equivalent to the domain phase of the local CML. As α decreases, the number of domains decreases and the motion within each domain becomes more chaotic (panel b, equivalent to the frozen random phase of the LCML). As α decreases further, the trajectories at each site are almost band-periodic with little spatial order within domains. Below a critical value of α, the lattice becomes spatially uniform. The uniform state is stable for all parameter (a) values of the uncoupled logistic map (fixed point, periodic, semi-periodic and chaotic) though the critical value of α shifts slightly depending upon a.

To locate the value of α at which the uniform state becomes stable, we sweep α, while holding a steady, and record the size of the coherent domain. The size of the coherent domain is defined as the number of sites such that $|x_i - x_{i+1}| < \delta$, with δ taken to be 10^{-11}. We average over 500 different initial conditions for each α and 100 time steps for each initial condition after discarding transients. We show the average coherent domain size for lattice sizes from $2^6 - 2^{10}$ for two parameter values ($a = 1.44$ and $a = 1.9$) of the logistic map in Figure 2.3.

For different values of a, the value for α at which the size of the coherent domain diverges, shifts depending on whether the single logistic map is band-periodic or chaotic. The transition from an initial uncorrelated state to a spatially uniform one becomes sharper as the lattice size increases. This behavior resembles a phase transition, where continuous variation in a parameter, α, results in a discontinuous jump in an order parameter, here, the size of the coherent domain.

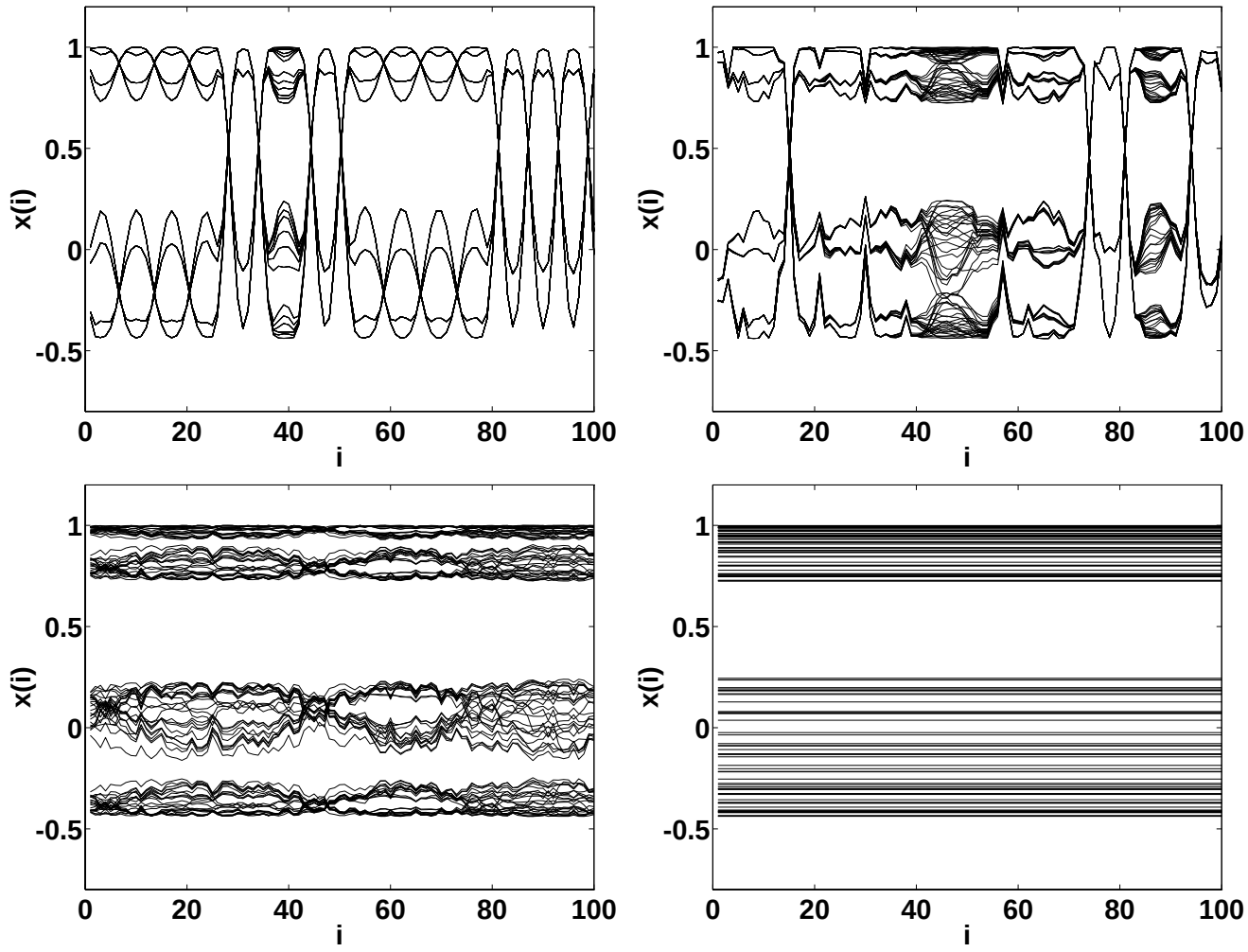

Figure 2.2. Space-time diagram for fractal CML with a =1.44 and a) α = 15, b) α=2.0, c) α=1.3, and d) α=1.1 for random initial conditions.

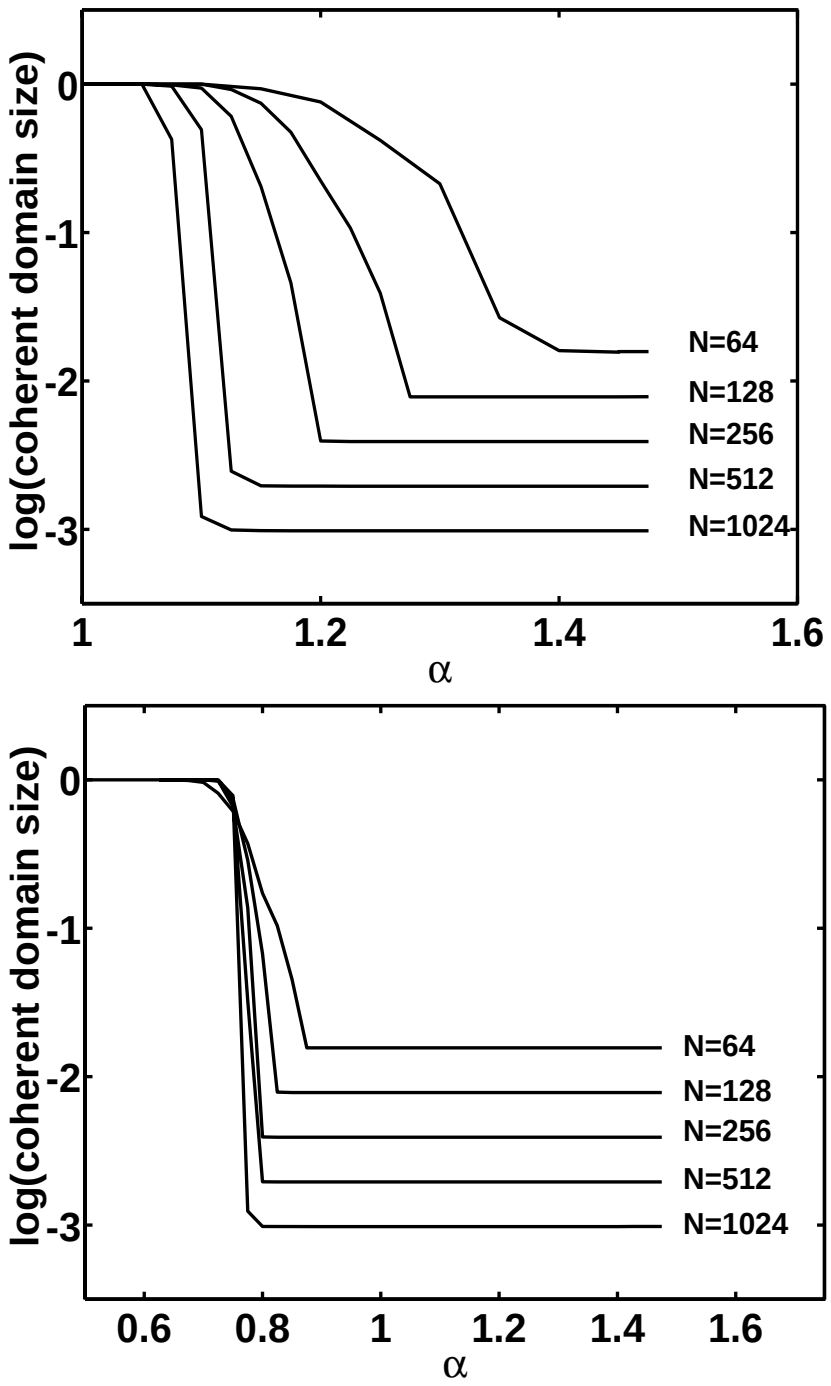

Figure 2.3. Fraction of coherent sites. Results are plotted on a log scale, averaged over 500 random initial conditions after discarding 10000 transient steps. Top panel: a=1.44 (band-periodic region of logistic map), Bottom panel: a=1.90 (chaotic region of logistic map).

The emergence of coherent structures in CMLs has been studied by stability analysis and statistical mechanics [13]. While, in general, temporally chaotic states in lattices with short range interactions lead to a loss of spatial coherence with exponentially decaying correlations in space [35], in models with asymmetric coupling and/or open boundary conditions, a stable uniform state can occur [36]. We show below that chaotic temporal states of lattices with probabilistic, long range interactions can exhibit long range spatial order with temporal chaos. We illustrate explicitly how we can separate the mode leading to spatial homogeneity from the other modes by means of a linear stability analysis.

2.3.1 Linear Stability Analysis

We examine the stability of the uniform state by means of a linear stability analysis about the uniform solution. To linear order in the deviations, $e_n(i) = x_n(i) - x_n$, we have:

$$e_{n+1}(i) = \frac{f'(x(n))}{A_i + 1}\big[e_n(i) + \sum_{j \epsilon conn} e_n(j)\big], \tag{2.10}$$

where the connection neighborhood is chosen according to Eqn 2.8.

The trivial solution for Eqn. 2.10 is $e_n(x) = 0$, which implies that if the lattice starts from a uniform state $x_0(j) = x_0,\ \forall\, j$, the sites stay uniform. We are interested in the long term behavior of a lattice perturbed infinitesimally from the uniform state.

We can rewrite Eqn. 2.10 as a matrix equation:

$$\mathbf{e_{n+1}} = f'(x_n)\ \mathbf{M}\ \mathbf{e_n}. \tag{2.11}$$

If $\mathbf{M}$ is diagonalizable, $|e_n| \propto (\rho_0 \lambda)^n_{max}$, where λ_{max} is the largest eigenvalue of $\mathbf{M}$ and $\log(\rho_0)$ is the Lyapunov exponent of the map, where ρ_0 is defined as:

$$\rho_0 = \lim_{n \to \infty} \left(\prod_l |f'(x_l)| \right)^{\frac{1}{n}}. \tag{2.12}$$

$\mathbf{M}$ is an asymmetric matrix with entries picked randomly according to the probability distribution of Eqn. 2.8. The conditions imposed on $\mathbf{M}$ are:

- *a*) the entries in every row sum to 1 because the lattice dynamics has to map the interval onto itself
- *b*) $\mathrm{M}_{i,i}$, $\mathrm{M}_{i,i+1}$ and $\mathrm{M}_{i,i-1}$ are positive, since the connection neighborhood always includes the nearest neighbors
- *c*) $\mathrm{M}_{ij} \geq 0, \ \forall \ i, j.$

The matrix $\mathbf{M}$ belongs to the general class of matrices known as stochastic matrices. The fractional number of entries in a row approaches a constant value as N increases and the fluctuations are proportional to $\frac{1}{\sqrt{N}}$. The nature of the eigenvalue spectrum of the matrix $\mathbf{M}$ can be established using the following theorems (We state these theorems without proof):

Let $a_{ij}^{(k)}$ denote the (i,j)th entry of the matrix $\mathbf{A}^k$, the kth power of $\mathbf{A}$. $\mathbf{A}$ is nonnegative if the entries of the matrix $a_{ij} \geq 0$ and positive if $a_{ij} > 0$.

Definition 1. If a nonnegative matrix $\mathbf{A}$ can be written as:

$$\mathbf{P}^{-1}\mathbf{A}\mathbf{P} = \begin{pmatrix} \mathbf{B} & \mathbf{C} \\ \mathbf{0} & \mathbf{D} \end{pmatrix}, \tag{2.13}$$

for some permutation matrix $\mathbf{P}$, and $\mathbf{B}$, $\mathbf{C}$, $\mathbf{D}$ are square submatrices, then $\mathbf{A}$ is reducible. Otherwise, $\mathbf{A}$ is irreducible.

Theorem 1. [37] *A nonnegative square matrix* $\mathbf{A} = (a_{ij})$ *is irreducible if and only if* $\forall \ (i,j) \ \exists$ *an integer* $k \in \mathbb{Z}$ *such that* $a_{ij}^{(k)} > 0$.

Theorem 2. [37]. *If* $\mathbf{A}$ *is a nonnegative matrix with a maximal eigenvalue* r *and row sums* $r_1, r_2, \cdots, r_n$, *then*

$$\rho \leq r \leq R, \tag{2.14}$$

where $\rho = \min\{r_i\}$ *and* $R = \max\{r_i\}$. *If* $\mathbf{A}$ *is irreducible, then the equality holds if and only if all the row sums are equal.*

Theorem 3. [37] *Let* $\mathbf{A}$ *be an irreducible matrix with maximal eigenvalue* r *with multiplicity* h. *Let* $\lambda_1, \lambda_2, \cdots, \lambda_h$ *be the eigenvalues of* $\mathbf{A}$ *with modulus* r, *where the modulus is* $(\sqrt{\mathrm{Re}(\lambda)^2 + \mathrm{Im}(\lambda)^2})$. *Then* $\lambda_1, \lambda_2, \cdots, \lambda_h$ *are the* h *distinct roots of* r^h.

Definition 2. A nonnegative matrix $\mathbf{A}$ is primitive if h is 1.

Theorem 4.. [37] *A necessary and sufficient condition for a nonnegative matrix* $\mathbf{A}$ *to be primitive is that* $\mathbf{A}^m$ *is positive for some positive integer.*

The eigenvector corresponding to the maximal eigenvalue is positive. We can use the above theorems to derive the bounds on the eigenvalues of $\mathbf{M}$. Condition b ensures that an integer k exists such that $\mathbf{M}^k$ is strictly positive. A tridiagonal, square, nonnegative $N \times N$ matrix with all nonzero entries equal, is positive for the integer $k = N - 3$. Since $\mathbf{M}$ is tridiagonal, with additional nonnegative entries, $k < N - 3$, in general. Thus $\mathbf{M}$ is irreducible and primitive and it has a non-degenerate, real positive eigenvalue, λ_{max}, such that:

$$\lambda_{max} > |\lambda_i|, \ i = 1 \cdots N - 1, \tag{2.15}$$

where λ_i is any oher eigenvalue of $\mathbf{M}$. Condition a ensures that $\lambda_{max} = 1$ [37] and that the corresponding eigenvector is uniform.

In the case, $\alpha \rightarrow \ \infty$, each site connects only to its nearest neighbors and the matrix becomes symmetric and tridiagonal, with additional entries in the upper right and lower left hand corners due to the periodic boundary conditions. In this case the eigenvalue spectrum of the matrix is:

$$\lambda(i) = \frac{1}{3}\left(1 + 2\cos(\frac{2i\pi}{N})\right), \ i = 0, 1, \cdots. \tag{2.16}$$

For the eigenvalue spectrum of Eqn. 2.16, the eigenvector corresponding to the largest eigenvalue represents the state of spatially uniform fluctuations which is unstable if $\rho_0 > 1$. Since the eigenvalue spectrum is continuous in the limit $N \to \infty$, a band of unstable non-uniform modes exists which destroys the spatial coherence of the lattice.

2.3.2 Origin of Eigenvalue Gap

The theorems on stochastic matrices only show that the eigenvalues of $\mathbf{M}$ are bounded from above by 1 and below by -1, but do not give the distribution of the eigenvalues. For cases where α is $\mathcal{O}(1)$, we calculate the eigenvalues of the stability matrix $\mathbf{M}$ numerically for a large number of matrices for fixed values of α, in order to make general statements about the nature of the uniform state. We find that the matrices have *all real* eigenvalues and the largest eigenvalue is 1 corresponding to the uniform solution, as expected. The eigenvalue spectrum has a gap which separates the largest eigenvalue from a continuous band of $N-1$ eigenvalues corresponding to non-uniform solutions (Figure 2.4), which is a surprising result. The value of α determines the size of the gap. In the $N \to \infty$ limit, for $\alpha > 2$, the gap goes smoothly to zero and the eigenvalue spectrum approaches that of Eqn. 2.16 as α increases. For $\alpha < 1$ the gap is large and bounded below. Intermediate values of α result in gaps which depend upon the lattice size. In the thermodynamic limit of an infinite lattice, we expect the gap to appear discontinuously for $\alpha < \alpha_{crit}$, which causes the divergence of the coherent domain size. While the lattice size affects the size of the gap, the existence of the gap depends only on the particular form of the coupling. The value of α_{crit} varies for each realization of the lattice as well as the value of a, and is hard to determine in general.

We now discuss the origin of the gap, first in a qualitative manner and then

in more detail using Fourier matrices. We take the connectivity of each site to be fixed at k to simplify the analysis and relax the assumption of symmetric connectivity. We have shown that the connectivity matrix $\mathbf{M}$ has a right eigenvector $\mathbf{e}_1 = [1, 1, \cdots, 1]^T$ corresponding to the largest eigenvalue. Let the next eigenvector orthogonal to $\mathbf{e}_1$ be $\mathbf{e}_2 = [u_1, u_2, \cdots, u_N]$. Orthogonality with $\mathbf{e}_1$ implies that $\sum_{i=1}^{N} u_i = 0$. Since $\mathbf{e}_2$ is an eigenvector with eigenvalue λ_2, *i.e.* $\mathbf{M}\mathbf{e}_2 = \lambda_2 \mathbf{e}_2$, the sum of the nonzero elements scales as λ_2 itself. By the law of large numbers, the sum of k random numbers (with zero mean and finite variance) would be $\sqrt{k}$. This relation is exact for a completely random connectivity matrix in the limit of infinite size. Even though $\mathbf{M}$ has additional entries along the upper and lower diagonals, which cause deviations from this behavior, as we see in Figure 2.5, the second largest eigenvalue for the FCML scales nearly as $\sqrt{k}/(k+1)$, the prefactor coming from the normalization for the FCML. Obviously, a completely random matrix, even for a small connectivity k, has a gap in the eigenvalue spectrum. However, the fractal connectivity matrix, in the limit of large α, has upper and lower diagonal terms which imply that the gap smoothly vanishes. As we shall see below, these off diagonal terms lead to interesting consequences for the eigenvalue spectrum in the case of asymmetric connectivity.

We can operate on $\mathbf{M}$ by a similarity transformation to separate its component along the eigenvector $\mathbf{e}_1$ from an $N-1$ dimensional matrix orthogonal to $\mathbf{e}_1$. Such a similarity transformation can be carried out by a Fourier matrix of order N given by $\mathbf{F}_N(i,j) = \omega^{(i-1)(j-1)}$ and its inverse, $\mathbf{F}_N^{-1}$, is $\mathbf{F}_N^{-1}(i,j) = \omega^{-(i-1)(j-1)}$, where $\omega = e^{2\pi i/N}$ is the Nth root of unity and $i = \sqrt{-1}$. For example, the Fourier matrix of order 6 is:

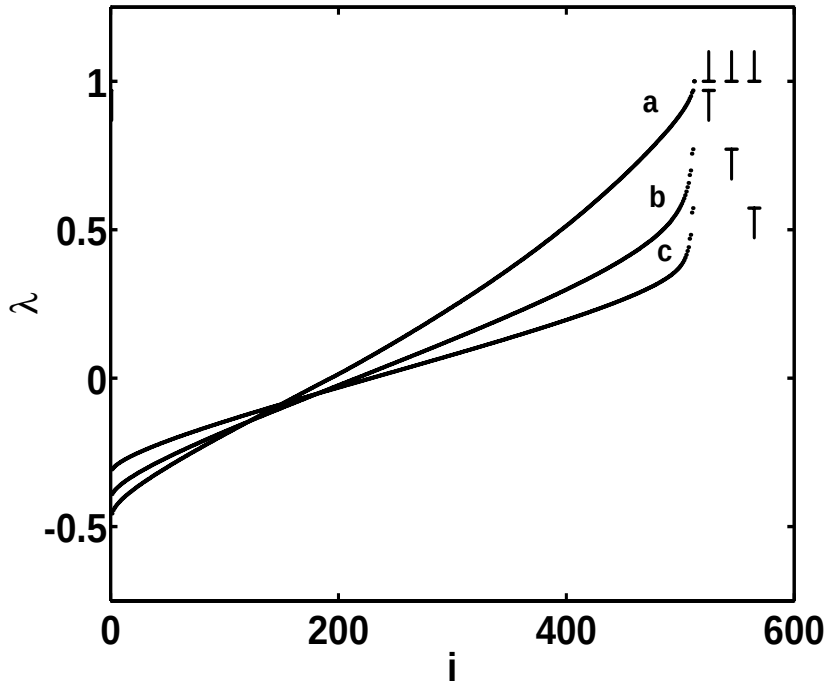

Figure 2.4. Eigenvalue spectrum of the connectivity matrix $\mathbf{M}$ of size 512×512; a) α=1.5, b) α=1.0, c) α=0.75. Bars show the gap in the eigenvalue spectrum.

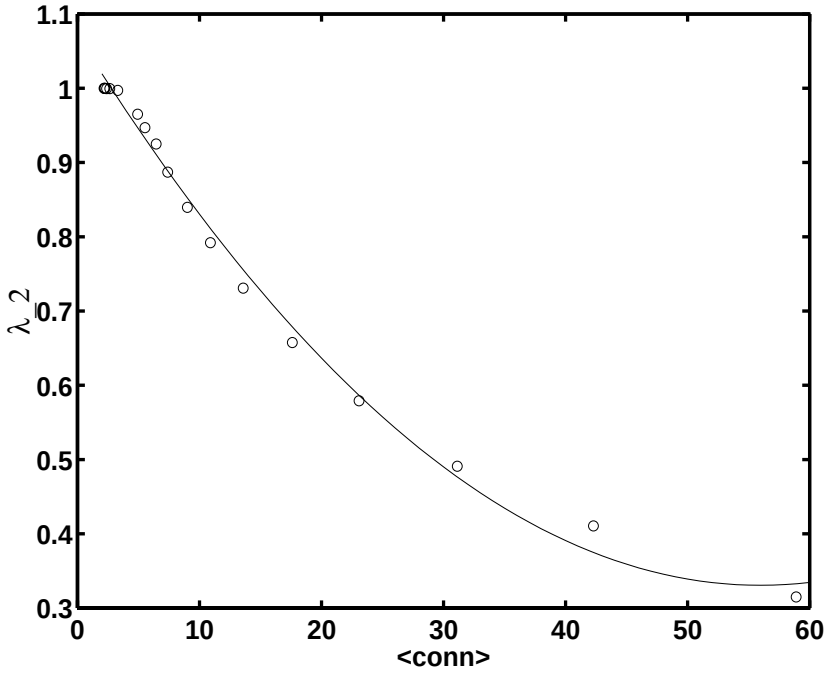

Figure 2.5. Second largest eigenvalue (λ_2) of the connectivity matrix $\mathbf{M}$ as a function of the mean connectivity. The solid line is the curve $\frac{1}{\sqrt{<conn>+1}}$. λ_2 follows the fit closely. Note that λ_2 approaches 1 as the connectivity decreases. The deviations from the fit are due to the fluctuations in the mean connectivity

$$\mathbf{F}_6 = \frac{1}{\sqrt{N}} \begin{pmatrix} 1 & 1 & 1 & 1 & 1 & 1 \\ 1 & \omega & \omega^2 & \omega^3 & \omega^4 & \omega^5 \\ 1 & \omega^2 & \omega^4 & \omega^6 & \omega^8 & \omega^{10} \\ 1 & \omega^3 & \omega^6 & \omega^9 & \omega^{12} & \omega^{15} \\ 1 & \omega^4 & \omega^8 & \omega^{12} & \omega^{16} & \omega^{20} \\ 1 & \omega^5 & \omega^{10} & \omega^{15} & \omega^{20} & \omega^{25} \end{pmatrix} \tag{2.17}$$

and $\mathbf{F}_6^{-1} = \mathbf{F}_6^{\dagger}$. We can now apply a similarity transformation to $\mathbf{M}$ to get $\mathbf{K} = \mathbf{F}^{-1}\mathbf{M}\mathbf{F}$. This transformation results in a matrix of the following form:

$$\mathbf{K} = \frac{1}{N} \begin{pmatrix} kN & N(I_1.f_2, \cdots, I_N.f_2).f_1^{-1} & \ldots & N(I_1.f_2, \cdots, I_N.f_2).f_1^{-1} \\ 0 & N(I_1.f_2, \cdots, I_N.f_2).f_2^{-1} & \ldots & N(I_1.f_N, \cdots, I_N.f_N).f_2^{-1} \\ \vdots & & \ddots & \vdots \\ 0 & N(I_1.f_2, \cdots, I_N.f_2).f_N^{-1} & \ldots & N(I_1.f_N, \cdots, I_N.f_N).f_N^{-1} \end{pmatrix} \tag{2.18}$$

where k is the connectivity of each site, $f_i = (1/\sqrt{N})(1, \omega^{(i-1)}, \cdots, \omega^{(N-1)(i-1)})$ is the ith row (or column) of $\mathbf{F}$ and f_i^{-1} is the ith row (column) of $\mathbf{F}^{-1}$. For illustration, we consider a lattice of connectivity, k=3. If the connectivity is random, any element of each row (except the diagonal) can be occupied with equal probability. Fractal connectivity implies that the upper and lower diagonals are populated, and the remaining 3 elements in each row can be 1 with uniform probability. Thus, a random connectivity matrix might be:

$$\mathbf{M} = \begin{pmatrix} 0 & 1 & 1 & 0 & 1 & 0 \\ 1 & 0 & 0 & 1 & 0 & 1 \\ 0 & 1 & 0 & 1 & 1 & 0 \\ 1 & 1 & 0 & 0 & 1 & 0 \\ 0 & 1 & 1 & 0 & 0 & 1 \\ 1 & 0 & 1 & 1 & 0 & 0 \end{pmatrix}, \tag{2.19}$$

while a fractal connectivity matrix would be:

$$\mathbf{M} = \begin{pmatrix} 0 & 1 & 1 & 0 & 0 & 1 \\ 1 & 0 & 1 & 1 & 0 & 0 \\ 1 & 1 & 0 & 1 & 0 & 0 \\ 1 & 0 & 1 & 0 & 1 & 0 \\ 0 & 0 & 1 & 1 & 0 & 1 \\ 1 & 1 & 0 & 0 & 1 & 0 \end{pmatrix}. \tag{2.20}$$

The CML corresponding to this choice of connectivity is:

$$x_{n+1}(i) = \frac{1}{k+1}\big[f(x_n(i)) + \sum_{j \neq i} M_{ij} f(x_n(j))\big], \tag{2.21}$$

where we have explicitly separated the connectivity matrix and the self interaction terms. The elements of the matrix $\mathbf{K}$ are given by:

$$\mathbf{K}(i,j) = \frac{1}{N}\sum_{m=1}^{N}(\sum_{l=1}^{k}\omega^{(j-1)(c(m,l)-1)})\omega^{-(m-1)(i-1)}), \tag{2.22}$$

where $c(i,j),\ i = 1 \cdots N,\ j = 1 \cdots k$ are the sites to which i connects (modulo N). For example $c(1,1) = 2$ for the random connectivity matrix. Clearly, $K(i,1)$ is 0 for $i \neq 1$, since the sum of the m, n^{th} roots of unity is zero except for unity itself. The eigenvalues of $\mathbf{K}$ are the eigenvalue k and the eigenvalues of the first minor of $\mathbf{K}$, *i.e.* the $N-1$ dimensional matrix in the subspace orthogonal to $\mathbf{e}_1$, which we call

$\mathbf{C}$. The elements of $\mathbf{C}$ are sums of the Nk roots of unity, which in the case of the random matrix are randomly chosen. In case of the fractal connectivity matrix, the upper and lower diagonal elements result in $2N$ roots of unity that sum to 0, and each element of $\mathbf{C}$ is a sum of $N(k-2)$ complex numbers.

This summation restricts the construction of a fractally connected lattice. Clearly, since 2 of the connections for each site are already fixed to be the nearest neighbors, only $k-2$ connections need to be chosen (if we fix the connectivity to k). The remaining connections can be chosen by generating numbers using a pseudorandom number generator and accepting the connection if it is less than the probability distribution $p(i,j)$ (Eqn. 2.8). However, a simple sequential sweep through the lattice results in a bias toward short range connections, introducing correlations in the elements of the matrix $\mathbf{S}$. A better method is to generate a random permutation of the integers 1 to N and choose $k-2$ connections, as earlier. Since the permutations are random, we avoid the correlations which affect the sequential connection process. Of course, if we do not fix the mean connectivity for the lattice, we can use either method, as all the entries of $\mathbf{M}$ are independently 0 or 1.

Let us first consider the case of a random asymmetric connectivity matrix and write $\mathbf{C}$ as $\mathbf{S}/N = \sqrt{\frac{k}{N}}\frac{1}{\sqrt{Nk}}\mathbf{S}'$, where $\mathbf{S}$, and $\mathbf{S}'$ are matrices with the same dimension as $\mathbf{C}$. The elements of $\mathbf{S}'$ are $(Nk)^{-1/2}\sum_{l=1}^{Nk}\exp(\theta_l)$, where the θ_l are randomly chosen. Thus the variance of the modulus of any element of $\mathbf{S}'$ is:

$$\langle|\mathbf{S}'(i,j)|^2\rangle = (\langle[\sum_{l=1}^{Nk}\cos(\theta_l)]/\sqrt{Nk}\rangle + \langle[\sum_{l=1}^{Nk}\sin(\theta_l)]/\sqrt{Nk}\rangle), \tag{2.23}$$

where the average is over the probability distribution.

The law of large numbers implies that the expectation value of $|\mathbf{S}'(i,j)|^2$ is 1 and by the Central Limit Theorem, the distribution of the elements is Gaussian. The elements are independent of each other since the connections are chosen randomly

and independently. $\mathbf{S}'$ is a complex asymmetric matrix with independent, identically distributed elements drawn from a Gaussian distribution with 0 mean and unit variance. The eigenvalues of $\mathbf{S}'$ lie in a unit circle in the complex plane [38] and thus the eigenvalues of $\mathbf{S}$ lie in a circle of radius $\sqrt{k}$.

We show the eigenvalue spectrum for the random k-regular connectivity matrix in Figure 2.6, without normalizing by the total connectivity k. Since the matrix is not symmetric, the eigenvalues are complex. The eigenvalues lie in a circle of radius $\sqrt{6}$ in the complex plane with a single real eigenvalue of 6, as shown above using the Fourier decomposition of the matrix.

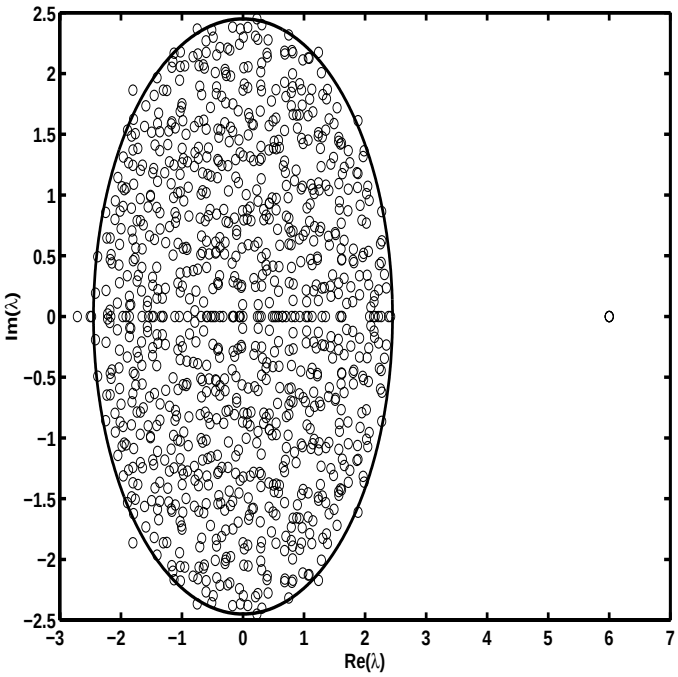

Figure 2.6. Eigenvalue spectrum of the completely random connectivity matrix for N=512 and $k = 6$ for 10 different realizations. $N - 1$ eigenvalues lie in a circle of radius $\sqrt{6}$.

We now apply a similar Fourier decomposition to a fractal connectivity matrix[2].

[2]In order to generate a fractal connectivity matrix which is regular with connectivity k, we

Figure 2.7 shows the eigenvalue distribution for a fractal connectivity matrix. We clearly see that the eigenvalues do not lie in a circle unlike the distribution for the random connectivity matrix. Once again, we obtain a matrix $\mathbf{C}$ as the first minor of the matrix $= \mathbf{F}^{-1}\mathbf{M}\mathbf{F}$. The elements of $\mathbf{C}$, however, are not the sum of k randomly chosen roots of unity. The similarity transformation diagonalizes a nearest neighbor connectivity matrix, and the eigenvalues are $2\cos(2\pi j/N),\ j = 1, \cdots, N-1$. Since the fractal connectivity matrix retains all nearest neighbor connections, the matrix $\mathbf{C}$ is now effectively $\mathbf{C}' = \mathbf{C} - 2(\cos(2\pi j/N)\mathbf{I}$. Thus the terms in $\mathbf{C}'$ are the sums of $N(k-2)$ distinct random roots of unity, and the largest eigenvalue is $2\cos(2\pi/N)+\lambda_1$ where λ_1 is the (complex) largest eigenvalue of $\mathbf{C}'$, which lies in a circle of radius $\sqrt{k-2}$. We have checked that the eigenvalue distribution of the fractal connectivity matrix with the upper and lower diagonal terms removed does indeed lie in a circle of radius $k-2$, except for $\mathcal{O}(1)$ number of real eigenvalues, which we cannot account for in this analysis (Figure 2.8).

We can carry out a similar analysis for the symmetric connectivity case as well. The matrix $\mathbf{K}$, is now unitary and a generalized Wigner's semicircle law gives the relevant eigenvalue statistics [38]. The deviations from completely random connectivity due to the nearest neighbor connections again enter in the same way as for asymmetric connectivity. We can show that the eigenvalue distributions are unchanged even if we have non-uniform mean connectivity, as in the numerical simulations.

Thus, we can relate the appearance of the spatially uniform but temporally chaotic states to the connectivity exponent α. If we consider a gap of width g, then for states such that $\rho_0 > 1$ and $\rho_0(1-g) < 1$, the uniform mode is spatially stable (in the sense that any small initial non-uniformity will lie in the gap and will die out) and temporally chaotic. The remaining $N-1$ nonuniform modes die

randomly choose $k-2$ connections for each site according to the probability distribution given by Eq. 2.7.

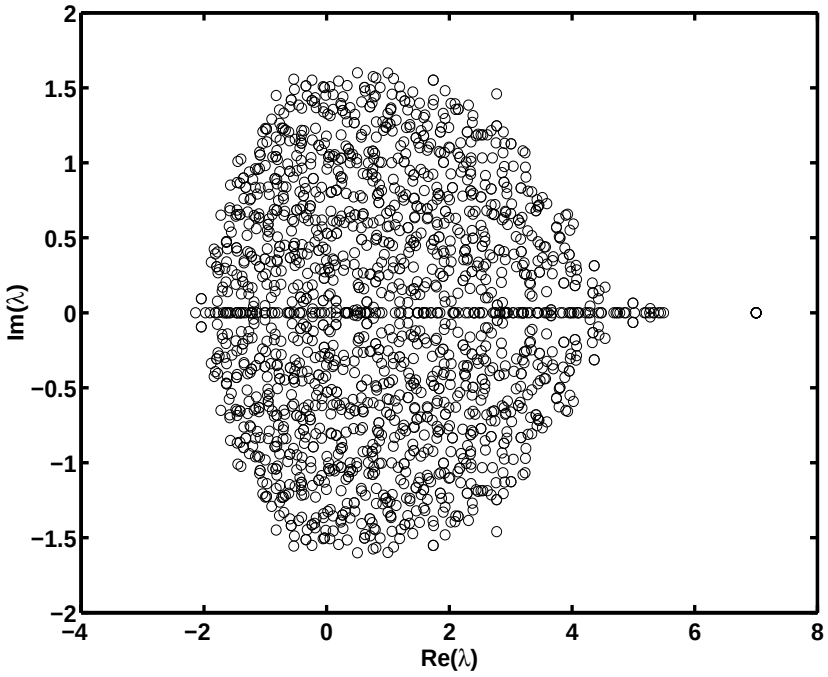

Figure 2.7. Eigenvalue spectrum of the asymmetric fractal connectivity matrix for N=512 and $k = 6$ and $\alpha = 0.9$ for 10 different realizations.

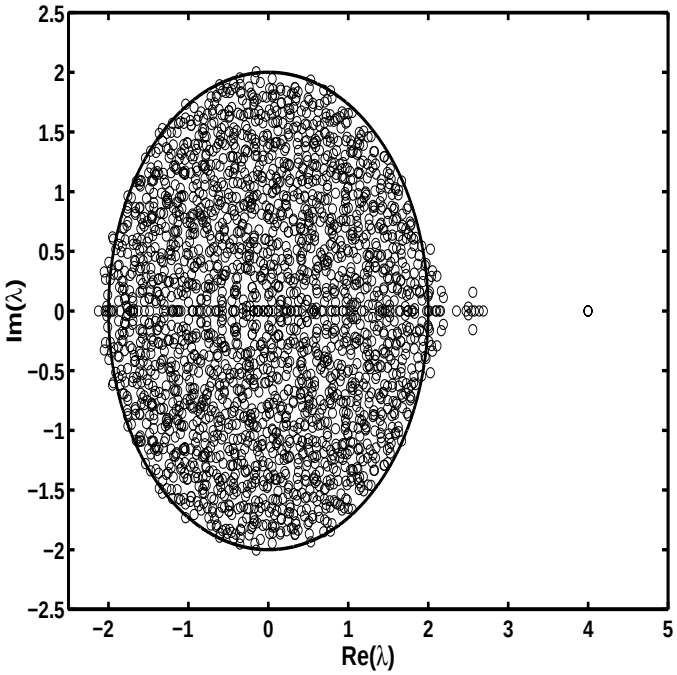

Figure 2.8. Eigenvalue spectrum of the fractal connectivity matrix for N=512 and $k = 6$ for 10 different realizations with the nearest neighbor connections removed. Most eigenvalues, except of an $\mathcal{O}(1)$ number lie in a circle of radius 2 ($\sqrt{k-2}$)

out since their eigenvalues are less than 1. The instability to uniform fluctuations remains, but does not destroy the spatial coherence. A similar gap in the eigenvalue spectrum was responsible for a uniform state in [36] for a nearest neighbor coupling CML with open boundary conditions, and a randomly coupled CML [39]. For temporally periodic states ($\rho_0 < 1$) , the uniform solution is always stable for all values of α, and any infinitesimal perturbation from an initial uniform state dies out, as we observe numerically. However, for random initial conditions, the temporally periodic, spatially uniform state does not appear for $\alpha > \alpha_{crit}$, implying a lack of global stability above α_{crit}, which a local, linear stability analysis would not indicate.

We can also interpret the dynamic behavior of the fractal CML in light of the relationship between the structure and function of a network, in particular, the effect of network connectivity on stability [40]. The stability of a dynamical system with a given Jacobian matrix with randomly chosen elements is usually addressed in the framework of the Wigner-May theorem [41, 42] which states that for a random connection matrix of zero mean, the state is almost surely unstable if the connectivity exceeds a threshold. However, the fractal CML with all nonnegative elements in the Jacobian matrix is unstable for low values of connectivity (and therefore interaction strength) but is stable for connectivity larger than some critical value.

2.4 Collective Behavior

Physical measurements on large, interacting ensembles of oscillators or spatially extended systems are often only possible for well defined macroscopic quantities, resulting in a coarse grained description of the dynamics. In analogy with statistical mechanics, macroscopic quantities are called order parameters. Changes in the dynamical state with parameter variation show up as transitions in the asymptotic states of these order parameters. Often, we can write down simplified, low dimen-

sional models for the dynamics of these order parameters, though the models may be approximate. The extent to which statistical mechanical analogies are valid for nonequilibrium models is an open question [43, 16]. Simple, equilibrium minded, intuition leads to the belief that in spatially extended, chaotic systems, macroscopic quantities do not evolve in time, apart from statistical fluctuations that vanish in the thermodynamic limit, while microscopic quantities can have nontrivial dynamics. How does this simple picture fit in with CML models? CMLs with local interactions display collective behavior and macroscopic order as long as the dimensionalilty of the system is high enough ($d > 2$) [44]. However, similar understanding for globally or randomly coupled models is lacking. Some indications of nontrivial collective behavior (NTCB) have come from the observations of ergidicity breaking in GCML but these models can display a richer spectrum of collective behavior. A continuous time model of coupled oscillators shows collective chaos [45, 46]. Models with local interactions can at most show quasiperiodic collective behavior. Randomly connected models have been studied even less, their importance to biology notwithstanding

The microscopic quantities in the CMLs are clearly the values of the local activity $x_n(i)$. In order to study their collective behavior, we need to define some suitable macroscopic order parameters. One such observable is the mean field:

$$h(n) = \frac{1}{N} \sum_{j=1}^{N} x_j(n). \tag{2.24}$$

A simple model for studying the macroscopic dynamics of Eq. 2.24 is the infinite dimensional GCML. As mentioned earlier, the GCML has two opposing tendencies, namely the synchronization due to the mean field and the desynchronization due to the chaotic local dynamics. Suitable parameter regimes lead to an incoherent state, where each site seems to evolve independent of the others. If in fact, the

elements are independent, quasirandom numbers, the mean field must converge to a stationary value, uncoupling the lattice sites, in the $N \to \infty$ limit. For finite N, the fluctuations of the mean field should decrease as $\frac{1}{N}$. Kaneko [47] studied the macroscopic dynamics of the GCML and concluded that the fluctuations of the mean field behave anomolously, *i.e.* the mean square deviation $< h^2 > - < h >^2$, decays as $N^{-\beta}$, with $\beta < 1$ rather than as $\frac{1}{N}$ as would be expected from the law of large numbers. Kaneko [47] has conjectured that a strong low dimensional collective motion of the lattice causes violation of the law of large numbers. How generic is the collective coherence of the GCML? Does a fundamental reason underly the violation of the law of large numbers? Pikovsky and Kurths [48] have provided a partial answer to this question. They assumed that the effect of the fluctuations in the mean field is modify the bare nonlinearity parameter a to $a_{eff} = 1 - \epsilon h_n$. Since the mean field fluctuates in time, the effective nonlinearity becomes time dependent. Thus the original GCML now becomes a set of uncoupled maps with a distribution of a which the mean field self-consistently generates. A study of these maps shows that the states of the lattice get trapped in a finite region of phase space, (a chaotic or quasiperiodic macroscopic attractor) *i.e.* the lattice is no longer ergodic (does not visit all parts of phase space with equal probability). Thus, time averages are not equivalent to ensemble averages. Since statistical characterization of the mean-field distributions implicitly assumed ergodicity, violations of the law of large numbers occur.

An alternate characterization of the phase space of the lattice is to look at the motion of a single site. If the fluctuations of the mean field decayed regularly with N, the $x_n(i)$ would be independent of each other, and the ergodic nature of the dynamics would mean that each single site eventually visits all parts of phase space. Thus, a long time trace of a single site is enough to characterize the whole motion.

This property is known as self averaging, *i.e.* an average over time of a single site is equivalent to the ensemble average. A lack of ergodicity generically implies the lack of self-averaging. Mean field models of spin glasses show a striking violation of self-averaging [49]. Crisanti *et al.* [50] have shown that the GCML has a glassy phase with a large multiplicity of attractors, which violates self averaging. They study the probability distribution of the time average of the variable x_i,

$$\langle x_i \rangle_{\mathrm{T}} = \frac{1}{\mathrm{T}} \sum_{n=1}^{\mathrm{T}} x_i(n), \tag{2.25}$$

with i chosen at random from a large lattice. The assumption of self averaging implies that the probability distribution, $\rho(\langle x_i \rangle_{\mathrm{T}})$ collapses to a delta function. However, in the glassy phase, $\rho(\langle x_i \rangle_{\mathrm{T}})$ is nontrivial, and does not change with the averaging time T, indicating the presence of ordered collective motion. Crisanti *et al.* argued that this violation of ergodicity and self-averaging results from the partition degeneracy of the GCML. By partition degeneracy, we mean that the equations are invariant under a partition of any integer N into m smaller integers $N_i = [N_1, N_2, \cdots, N_m | \sum_{i=1}^{m} N_i = N]$. So the indices of the individual elements x_i can be reassigned by permutation so long as the overall N_i are preserved, leading to a multiplicity of microscopic states that correspond to a single macroscopic state. This high degree of multiplicity of attractors resembles the attractor crowding in mean field models of spin glasses, hence the name. The lattice does not self average in the glassy phase, while it does so in a macroscopic chaotic phase ($a > 1.8$) with very few attractors.

We studied the long time histograms of Eqn. 2.25 for the FCML for various values of a and connectivity exponent α. For very large values of α (the local coupling limit), we find that the lattice self averages. Figure. 2.9 clearly shows this self-averaging, where the distribution tends to a delta function as the averaging time increases.

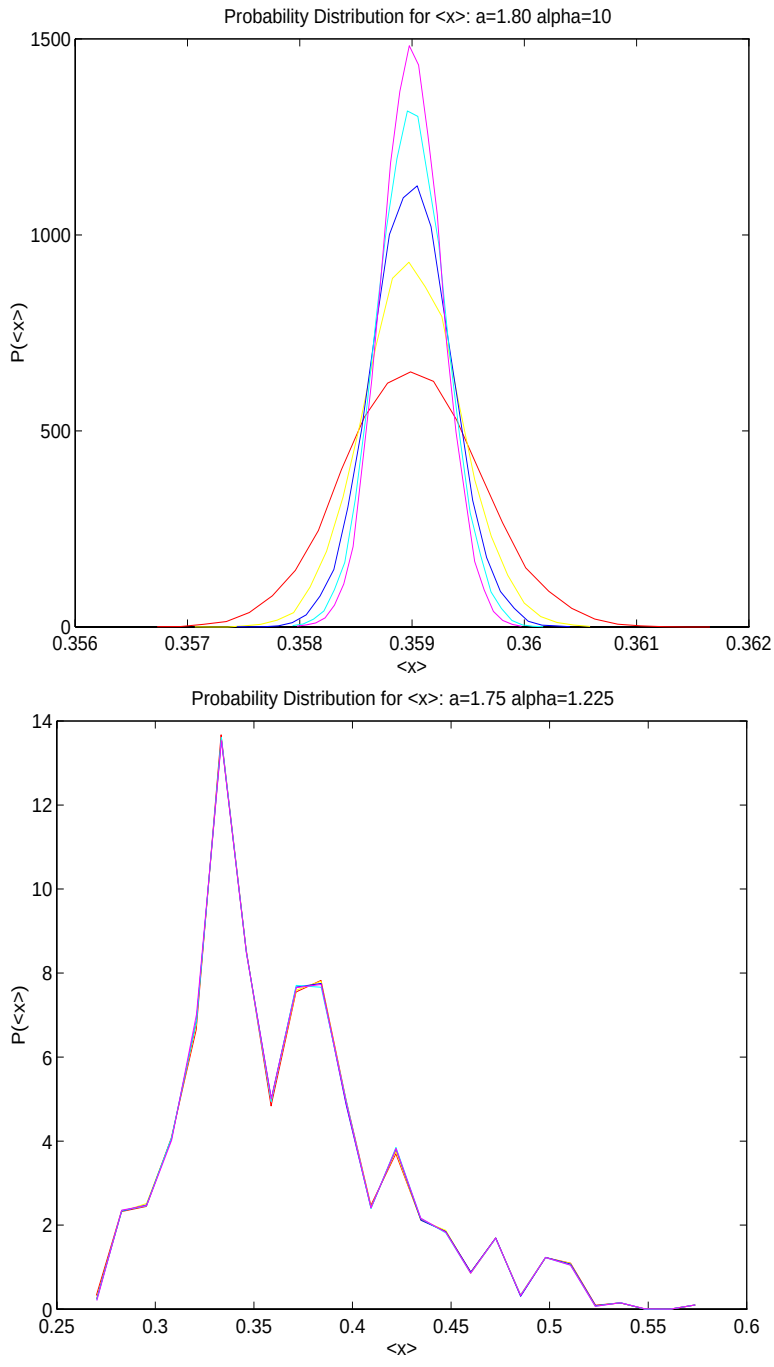

Figure 2.9. Probability distribution of $\langle x \rangle$ at various observation time T. Top panel: local coupling limit, $\alpha = 10$ and a=1.8, Bottom panel: α=1.225, a=1.75. The different curves are averages performed at 1×10^4, 2×10^4, 3×10^4, and 4×10^4 after an initial transient.

For α=1.25, histograms of $x_n(i)$ converge to a nontrivial distribution that does not change with the averaging time, indicating a lack of self-averaging. This property is generic for the FCML for most values of a and α, as long as the lattice does not synchronize or the connectivity is not too localized (*i.e.* most sites are only locally connected to their nearest neighbors). The lack of special symmetries and stable cluster states for the FCML implies that glassy behavior with multiple degenerate attractors, is not a necessary condition for ergodicity breaking. Instead, we argue that a sufficient condition for non-ergodicity is the appearance of low dimensional collective behavior. We have already seen that the GCML is non-ergodic due to collective coherent motion. Nonlocal connections in the FCML allow each site to sample k different sites. Random sampling results in an estimate for the median of the sample with an accuracy that depends on the sample size rather than the size of the population [51]. In a uniform distribution, in the limit of infinite N, an estimate for the mean and median are identical and any oscillator sees the mean field more and more accurately as k increases. In fact, values of k of $\mathcal{O}(1)$ suffice to approximate the mean field. Thus, in this limit, the FCML resembles a globally coupled model and the appearance of collective behavior coincides with ergodicity breaking. We have checked that the FCML does have nontrivial, low dimensional collective behavior, where the mean field settles into a quasiperiodic state.

We briefly digress from the subject of collective behavior in coupled maps to discuss another important network dynamical system. Cellular automata on lattices exhibit suggestive parallels with spatially extended continuous dynamical systems. Studies of cellular automata in 2 and 3 dimensions [52, 53, 54, 55] show that nontrivial collective dynamics is only possible in 3 or more dimensions. 1 and 2 dimensional lattices settle into a macroscopic 2^m periodic state, with low m. Mousseau [56] has shown that randomly connected cellular automata also order into a macroscopic

quasiperiodic state for a narrow range of connectivity. Recent studies on 2 state cellular automata on random graphs show that the appearance of collective quasiperiodic dynamics depends sensitively on the characteristics of the chosen graphs [57]. Ordered graphs such as a Cayley trees with closed edges settle into a macroscopic stationary state (the mean field goes to a fixed point), while in random graphs, the mean field becomes quasiperiodic, indicating that graph theoretic measures such as path lengths or distribution of loop sizes are important for characterizing nontrivial collective states. Preliminary studies of cellular automata on fractally connected substrates also show nontrivial collective states, such as quasiperiodicity or intermittency, and further research will evaluate the intimate relationship between the structure and dynamics of networks.

CHAPTER 3

DIFFUSIVELY COUPLED BURSTERS

3.1 Introduction

Electrical activity in cells arises from the presence of cellular and subcellular processes that operate on a hierarchy of time scales. These processes interact nonlinearly to produce complex temporal activity that is critical for physiological function. Fast ion channels in cell membranes switch at millisecond time scales, producing the familiar action potentials (sharp voltage spikes), which in the nervous system, provide the fundamental mechanism for information transmission, and in electrically excitable media, such as heart tissue, drive muscle contraction. Calcium channels have slower ($\sim$100 ms) time scales leading to characteristic burst patterns in the electrical activity (a repetitive pattern of several action potentials in succession followed by a period of silence). Transmission of action potentials between different neurons, or between neurons and muscles occur across localized patches in the membrane called synapses, which release chemicals in response to voltage changes caused by action potentials. The time scales of chemical release at synapses are distributed in a range of 1-500 milliseconds, and even longer (up to 1s in some invertebrate neurons). Modifications of the synaptic strengths (the amount of chemical released in response to an action potential), which are crucial for learning in the nervous system, occur at time scales on the order of seconds or minutes because they require an up or down regulation of gene expression, an inherently slow process. Learned patterns

or memories decay over time scales of minutes to hours or days. Finally, the time scales for chemical modulations of various spike patterns are also distributed over a range of time scales ranging from milliseconds to hours. All these processes combine to produce complex patterns necessary for life, such as locomotion, digestion, breathing, memory, and perhaps, awareness. Shepherd [58], Kandel and Schwartz [59] review the biology of electrical activity of neurons and Goldbeter [5] gives an excellent pedagogical account of the mathematics of biochemical oscillations.

One example of activity on multiple time scales in neurophysiology is the reflexive swim activity of the marine mollusc, *Tritonia*, which responds to a large amplitude tactile stimulus by initiating a swim pattern to escape from predators. The swim pattern is a series of 2-20 alternate dorsal and ventral (left and right) movements lasting about 10-50s. A network of 14 central pattern generating (CPG) neurons divided into 3 classes [60] produces the characteristic swim pattern. The time scales of the intrinsic conductances and the synaptic activity set the basic rhythm. Chemical modulation of the swim pattern period and duration also occurs over 10s of seconds.

In this chapter, we study a nonlinear oscillator that has two different time scales and trace some of its characteristic patterns in parameter space. The principal motivation for this model comes from a typical pattern of voltage oscillations of neuronal membrane potential called bursting. Dynamical systems theory can systematically characterize bursting in single cells, but our understanding of the dynamics of coupled bursters is incomplete.

3.2 Bursting

3.2.1 Electrical Activity of Biological Cells

All living cells are enclosed by a thin membrane (75 Å in thickness), made up of phospholipids with embedded proteins. The lipids provide the basic structure of the membrane. The proteins embedded in the membrane carry out several physiological functions, such as receiving and transmitting external signals and catalyzing reactions. One class of proteins forms pore-like ion channels and pumps which act as gates controlling the flow of ions into and out of the cells, maintaining the osmotic balance by active transport of ions. Specific channels are selective for different ionic species, for example the sodium (Na^+) channel or the potassium (K^+) channels regulate the flow of sodium and potassium ions. These channels are not open constantly, but act as switches, opening only under certain conditions.

The phospholipid molecules are polar, with a hydrophobic tail and hydrophilic head. The basic membrane forms spontaneously in a bilayer with the heads facing the outside and the inside of the cells. The hydrophobic tails create a membrane that is impermeable to various ions in aqueous solution, while being permeable to water. The impermeability of the membrane to ions in aqueous solution results in an imbalance of ion concentration across the membrane. For example, sodium concentration is low inside the cell and high outside, and vice versa for potassium concentration, resulting in a potential difference across the cell membrane, called the membrane potential. The electric potential difference from a concentration difference for any ionic species on the two sides of the membrane is given by the Nernst equation:

$$V_{ion} = \frac{RT}{FZ}\frac{[C_o]}{[C_i]}, \tag{3.1}$$

where R is the universal gas constant, F is Faraday's constant, T is the temperature

and Z is the valence of the ions. $[C_o]$ and $[C_i]$ are the ion concentrations outside and inside the cell. Thus, the membrane potential, V_{ion}, is the potential difference due to the concentration difference. The resulting electric field would cause an ion flux across the membrane through passive diffusion till an equilibrium is established. However ion pumps actively maintain the concentration difference, establishing a constant potential V_m of -65mV.

An action potential, or a voltage spike occurs when sodium channels open transiently in response to an increase in the membrane potential, allowing Na^+ ions to flow into the cell. This inflow raises the membrane potential to V_{Na} (the Nernst potential for sodium ions) in the up-stroke of the action potential. The sodium channels close at high membrane potentials, and the potassium channels open after a short delay, extruding K^+ ions, repolarizing the membrane towards V_K. The potassium channels close as the voltage returns to the resting potential. The active ion pumps now restore the ionic balance, restoring the membrane potential to its resting value.

Hodgkin and Huxley [61], in their seminal work, extensively studied and modeled the complex kinetics of the ion channels. Their approach still forms the basis of most cell level modeling in neuroscience. They modeled the membrane as a circuit with capacitance, resistance and non-linear current sources (the ion channels). Thus the membrane current, i_m, is:

$$i_m = C_m \frac{dV}{dt} + \sum I_{ion}, \tag{3.2}$$

where C_m is the membrane capacitance and I_{ion} are the ionic currents due to the channels. At rest, i_m is zero, just a restatement of Kirchoff's law. The driving force for each ion, the I_{ion} term, is proportional to the difference between the membrane potential and the Nernst potential for the ion, *i.e.* it has the form $(v - v_{ion})$. The proportionality constant is the effective conductance g_{ion}, the reciprocal of

the resistance, which is assumed to be a nonlinear function of the voltage and perhaps other ionic concentrations. This dependence reflects the voltage dependent kinetics of ion channels and the modification of these kinetics by the modulating effects exerted by some ions such as calcium and other chemicals. The nonlinear conductances are at the heart of action potential generation.

Thus, a model of the membrane potential is a set of first order differential equations for the voltage and the membrane kinetics. Hodgkin and Huxley's major achievement was to derive a phenomenological form for the I_{ion} current from a series of experiments on the channel kinetics for the Na^+ and K^+ ions in a squid neuron. The conductance of a single channel is of the order of picoSiemens and the phenomenological equations for the ionic currents describe the kinetics of a large population of channels. The resulting equations are highly nonlinear, allowing for a rich repertoire of temporal patterns. The electrical behavior of electrically active cells (secretory cells and neurons) differ markedly depending on the concentrations of different types of channels. A study of their kinetics is key to understanding the cells' physiological functions.

Because of the importance of the Hodgkin-Huxley (HH) formalism and to illustrate the nature of the equations governing the electrical activity of cells, we give the HH equations below and discuss some of their features. The HH equations for the electrical potential of the squid giant axon are a set of 4 ODEs:

$$C_m \frac{dV}{dt} = -g_{Na} m^3 h (V - V_{Na}) - g_K n^4 (V - V_K) - g_{leak}(V - v_{leak}) + I_{app}, \quad (3.3)$$

$$\frac{dm}{dt} = \frac{(m_\infty(V) - m)}{\tau_m(V)}, \quad (3.4)$$

$$\frac{dh}{dt} = \frac{(h_\infty(V) - h)}{\tau_h(V)}, \quad (3.5)$$

$$\frac{dn}{dt} = \frac{(n_\infty(V) - n)}{\tau_n(V)}. \quad (3.6)$$

The variables are V, the membrane potential [mV], $\{m,\ h\}$, the phenomenolog-

ical variables related to the probability of the opening and closing of the sodium channel respectively and n, a phenomenological variable related to the opening probability of the potassium channel. C_m is the membrane capacitance. I_{app} is an externally applied current, either from other cells or through an electrode in a controlled experiment, and g_{Na}, g_K, and g_{leak} are the maximum conductance [μS] of the sodium channels, potassium channels and the spontaneous leak across the membrane. The functions $x_\infty(V),\ \tau_x(V),\ x = m, h, n$ are the rate functions for channel opening and closing, and depend on the membrane voltage (and temperature). The functional form of the rate dependence can be determined experimentally and then fit to sigmoidal forms. The first two terms in the voltage equation are the ionic currents, and the functional forms vary for different types of cells, even for the same type of channels. We give the rate functions in Appendix A.

Eqns. 3.3-3.6 are actually the "space-clamped" versions of the original equations, and describe action potential generation over an isopotential membrane. Hodgkin and Huxley added a diffusion term to the voltage equation to describe conduction of action potentials down the nerve cylinder. In the following, we will consider the diffusion term to be very fast, resulting in an isopotential cell, reducing the PDEs to ODEs (Eqns. 3.3-3.6). The HH equations with diffusion have been studied extensively (actually a planar approximation of the HH equations, the Fitzhugh-Nagumo equations) as a model of extended excitable media. The interaction of diffusion and local dynamics results in spatiotemporal patterns such as traveling waves, spiral waves, trains of pulses and chaos.

Experimental preparations usually study the electrical activity of cells by applying an external current. This experiment is analogous to studying the dynamics of Eqns. 3.3-3.6 by increasing the applied current. With no applied current, the membrane is at the resting potential, given by the steady states of Eqn. 3.3-3.6,

obtained by setting the derivative terms to zero. Brief current pulses increase the membrane voltage as the membrane capacitance charges up, and then decays exponentially after the removal of the current pulse. If the current pulse is large enough, the membrane voltage increases sufficiently to open Na channels, which feedback positively, to open more Na channels and eventually cause a spike. The potassium channels now open causing the downstroke of the spike and an undershoot below the resting level. The membrane then returns to its resting level. Prolonged application of a supercritical current pulse results in repetitive spiking.

We show the numerically constructed bifurcation diagram for Eqns. 3.3-3.6 in Figure 3.1. For low values of I_{app}, the cell is at rest, with a membrane potential of ~ -62 mV. As the current increases, the rest state destabilizes at $I \sim 10\ \mu A/cm^2$ via a Hopf bifurcation (*i.e.* a pair of complex conjugate eigenvalues of the linearized Jacobian matrix crosses the imaginary axis). This bifurcation results in repetitive activity and the cell spikes periodically with a period which increases with increasing current.

3.2.2 Analysis of Bursting

Bursting is common in biological oscillators and chemical reactions such as the Belousov-Zhabotinsky reaction, notably in the electrical activity of neurons and pancreatic β cells [2]. During bursting, the oscillators typically alternate between silent and active phases. In the active phase, the variables rapidly oscillate, while in the silent phase they change slowly. Transitions between the active and silent phases are rapid compared to the time scale of the oscillations themselves and the successive transitions are periodic in time.

Different burst patterns depend on the complex mechanisms that interact with each other. These burst signatures have evocative names attached to them describ-

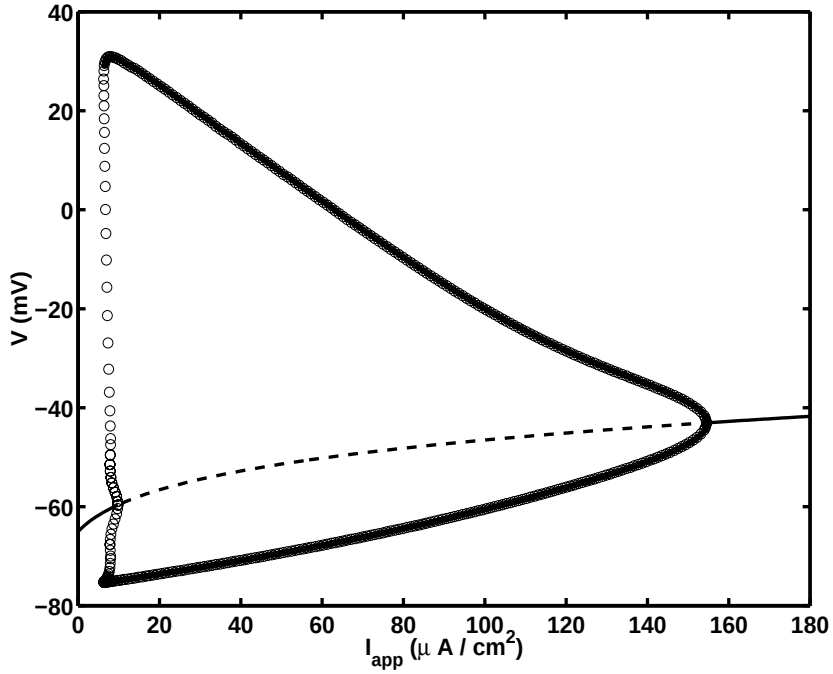

Figure 3.1. Bifurcation diagram for the HH model constructed using the automated bifurcation analysis software AUTO [1]. Solid lines indicate stable fixed points and broken lines indicate unstable fixed points. Heavy lines denote stable periodic orbits and open circles denote unstable periodic orbit. A subcritical Hopf bifurcation occurs at $I_{app} = -10\ \mu A/cm^2$ and another Hopf bifurcation occurs at $I_{app} = -\ 160 \mu A/cm^2$.

ing some of their salient features. We show some characteristic burst patterns in Figure 3.2. The burst variable is the transmembrane electrical potential. An important ingredient for bursting electrical activity is the presence of processes that modify the membrane potential at multiple, widely separated time scales.

The origin of multiple time scales in the HH models of action potentials is immediately obvious. The $\tau_x(V)$ give the characteristic times associated with the channel variables. If some $\tau_x(V)$ are large, and hence, the associated channel variables, x, vary slowly in V, while others are smaller by orders of magnitude, we have a separation of time scales. Large enough separations result in a set of singularly perturbed equations with slow and fast variables. The interaction of these time scales results in the characteristic burst patterns in Figure 3.2. Most of the burst patterns can be reproduced by minimal models (which can be more or less rigorously constructed from full models with several HH type equations) with 2 fast variables and 1 or 2 slow variables. Some burst patterns such as the bursts in hippocampal and cortical pyramidal cells (panels I & J in Figure 3.2) require several slow variables for a complete description.

As an illustration, consider the 3 variable modified Sherman-Rinzel-Keizer (SRK) [62, 63] model for the bursting behavior of pancreatic β-cells, which secrete insulin in the presence of glucose:

$$\tau \frac{dV}{dt} = -g_{Ca} m_\infty(V)(V - V_{Ca}) - g_K n(V - V_K) - g_S S(V - V_K), \tag{3.7}$$

$$\frac{dn}{dt} = \frac{n_\infty(V) - n}{\tau_n}, \tag{3.8}$$

$$\frac{dS}{dt} = \beta \frac{S_\infty - S}{\tau_S}. \tag{3.9}$$

The relevant ionic currents are the Calcium current (with a Ca^{++} conductance g_{Ca}), a potassium conductance as before and a phenomenological variable S, which could be a slow calcium channel or reflect the concentration of some other metabo-

Square-wave Bursting

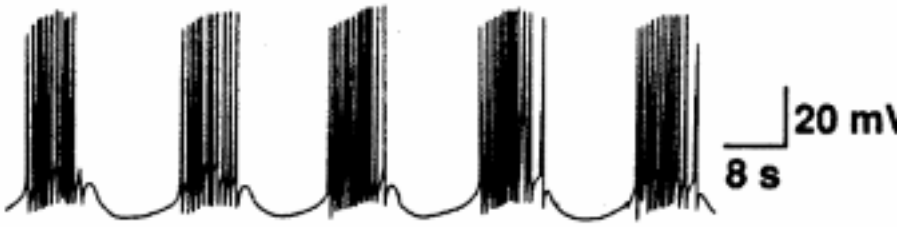

Parabolic Bursting

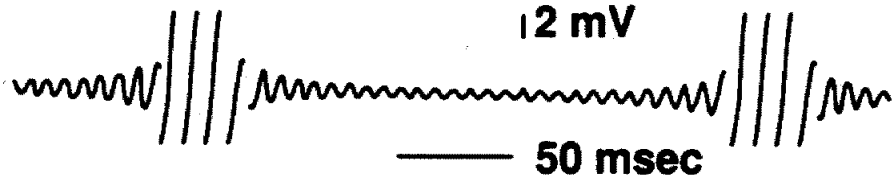

Elliptic Bursting

Complex Bursting

Figure 3.2. Examples of rhythmic bursting, showing the time courses of the membrane potential. A. Square wave bursting in a pancreatic β-cell. B. Square wave bursting in a dopamine containing neuron in the rat brain. C. Elliptic bursting in a *Sepia* giant axon. D. Complex dendritic mediated bursting in the mouse cortex. From [2].

lite. We give the explicit forms of the rate functions and other parameters in Appendix A. The time scales for the V, n and S equations are now constants, rather than functions of the membrane potential. τ and τ_n are 20 ms while τ_S is 35 s (!!). Thus, S is the slow variable and V, n are the fast variables (the calcium channels are taken to activate (open) and inactivate (close) instantaneously). The SRK equations are a set of singularly perturbed differential equations in $\mathbb{R}^{2+1}$, where we have separated the two dimensional fast subspace and the one dimensional slow subspace. We show the integration of Eqns. 3.7-3.9 in Fig. 3.3.

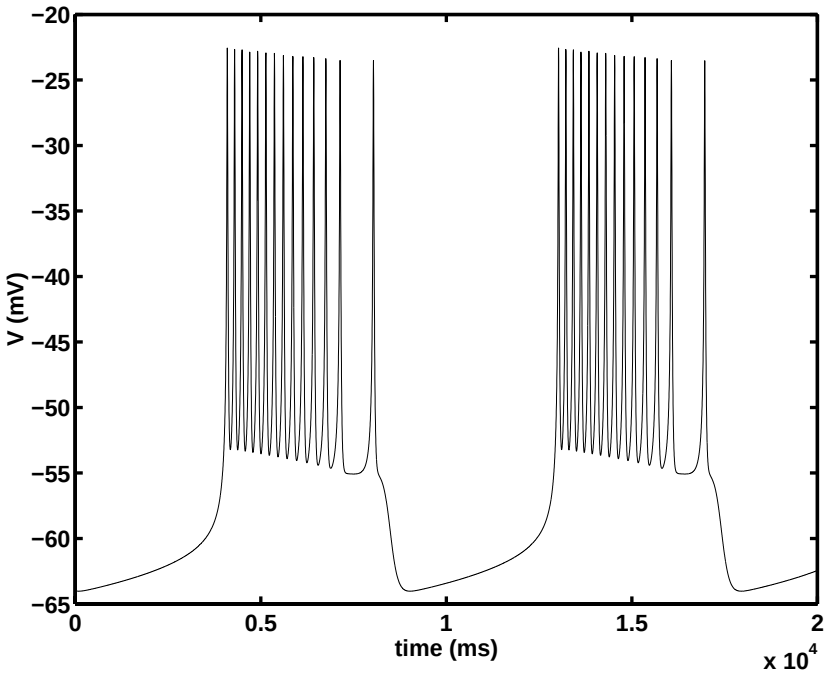

Figure 3.3. Time integration of the Sherman-Rinzel-Keizer equations showing the membrane voltage

We see clearly a periodic burst pattern with alternating active (oscillatory) and silent (rest) phases. The transition between the rest and spiking states is rapid, and the spike frequency decreases continuously. Note that the last spike is higly delayed relative to the previous ones. Any model must account for the rapid transitions

between the active and silent phases as well as the dynamics of the active phase spikes. We exploit the 3 orders of magnitude difference between the time scales to obtain a qualitative understanding of the dynamics of the SRK model. The small parameter $1/\tau_S$ justifies a perturbation theory approach to the dynamics. However, the expansion differs from standard perturbation theory in physics, where the solution is known for an unperturbed system, and a perturbation expansion in powers of the small parameter approximates the full solution. The nonlinearity of the equations precludes analytic solutions even in the unperturbed case. Thus our approach will necessarily be geometric and qualitative.

Let us take the singular limit, where $\tau_S \to \infty$. Now, S is frozen in time, and enters in the V and n equations as a parameter. The dynamics of V and n are on a fast time scale, parametrized by t. The slow variable S evolves on a slow time scale $T = \varepsilon t, \varepsilon = \frac{1}{\tau_S}$. Thus for the fast subsystem, the perturbation parameter ε induces a slow variation of the parameter S, resulting in a slowly varying set of equations. On the slow time scale, V and n remain near their steady states (either resting, or oscillating). Bifurcations of the fast subsystem result in transitions between steady states from the neighborhood of one attractor to another. The times for these jumps from silence to quiescence and vice versa occur with a characteristic time ε. The evolution of the SRK model on the slow time scale is (in the $\varepsilon = 0$ limit) a differential algebraic equation. The complete solution of the (2,1) dimensional ODEs can be constructed by piecing together the fast jumps and the drift on the slow manifolds.

To make this approach more clear, we consider a geometric singular perturbation method originally due to Rinzel [2]. The first step in a bifurcation analysis is to determine the steady states of the fast subsystem. Setting $n = n_\infty(V)$ in Eqn. 3.7, have the steady state current:

$$I_{SS}(V;S) = g_{Ca} m_\infty(V)(V - V_{Ca}) + g_K n_\infty(V - V_K) + g_S S(V - V_K) = 0, \quad (3.10)$$

as a function of V, with S as a parameter. For low values of S, $I_{SS} = 0$ has one solution at high V. For high values of S, $I_{SS} = 0$ again has one solution at low V. Intermediate values of S result in 3 solutions for the steady state current. The stability of the steady states can only be determined numerically.

We show the bifurcation diagram of the V, n equations with S considered as a bifurcation parameter in Fig. 3.4. S, the fraction of open channels, varies from 0 to 1. The solutions of Eqn. 3.10 form a Z shaped curve. For small S, the fast subsystem has a single, high voltage steady state. As S increases, a Hopf bifurcation (HB) creates a stable periodic orbit surrounding the now unstable steady state. For larger values of S, a saddle node (SN) bifurcation creates an additional pair of steady states. The lower branch in Fig. 3.4 contains stable steady states (the rest states) and the middle branch is a set of saddle points with one dimensional stable and one dimensional unstable manifolds. The fast subsystem has two stable solutions for a range of S, namely a fixed point and a periodic orbit. For larger S, the periodic orbit disappears in an infinite period orbit (called a homoclinic or saddle loop bifurcation [9]) as the amplitude of the periodic orbit grows till it contacts the stable and unstable manifolds of the saddle point.

Beyond this value of S, only a single rest state is stable, while the other two states are unstable. Finally, another saddle node bifurcation leaves the low voltage rest state as the only fixed point. Thus the steady states of V (and hence n) lie on a Z shaped curve, with the knees of the Z being the saddle node bifurcation points. What about the slow evolution of S? The steady states of S as a function of V lie on a curve obtained by setting the left hand side of the S equation to 0, which intersects the Z curve on the middle branch. Below this line, S decreases, and above it, S increases. We call this line the S-nullcline. The intersection of the two curves gives the steady state of Eqns. 3.7-3.9. If the intersection is on the middle branch

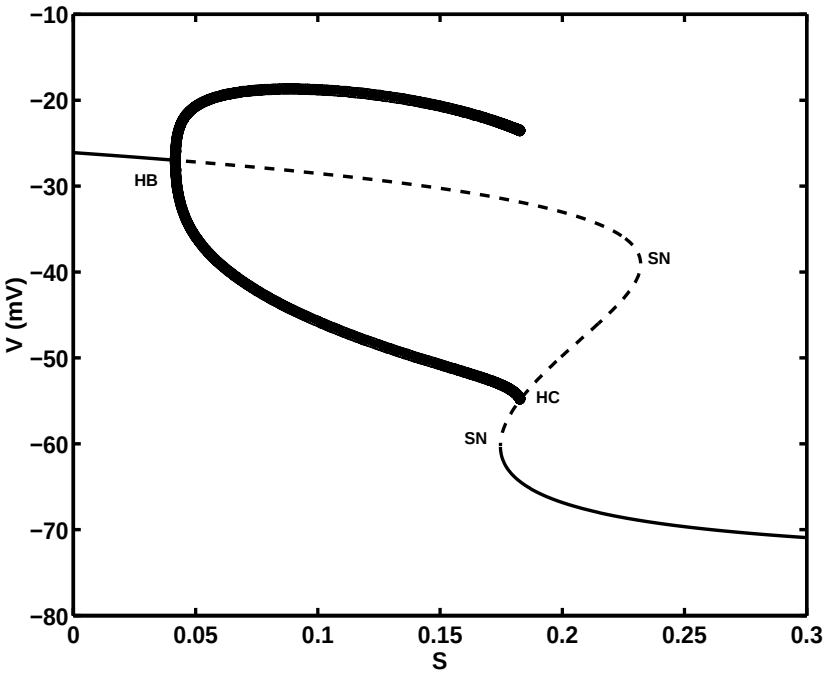

Figure 3.4. Bifurcation diagram for the Sherman-Rinzel-Keizer model constructed using the automated bifurcation analysis software AUTO. Solid lines indicate stable fixed points and dashed lines indicate unstable fixed points. Heavy lines denote periodic orbits. The bifurcation points, saddle node (SN), Hopf (HB) and homoclinic (HC) are indicated on the curve.

of the Z curve, the steady state is unstable, leading to a bursting solution and if the intersection is on the lower branch, the steady state is stable, with no bursting. Depending on the choice of parameters in the slow S equation, the S-nullcline can intersect the Z curve more than once. We will not consider this case here.

We now start Eqns. 3.7-3.9 close to the low voltage rest state. Since the rest state is stable, it attracts trajectories, and V tracks the lower branch of Z as S decreases (Figure 3.5). When S reaches the knee (SN), the only stable state is the periodic orbit, and V "jumps" up on a fast time scale. Now V is above the S nullcline, and thus S increases. V now tracks the periodic orbit, until it disappears in the infinite period orbit (HC). Since the rest state is the only stable state left, V "jumps" down to it. Thus, to first order in ε, the jump up and jump down points are the saddle node point and the homoclinic point.

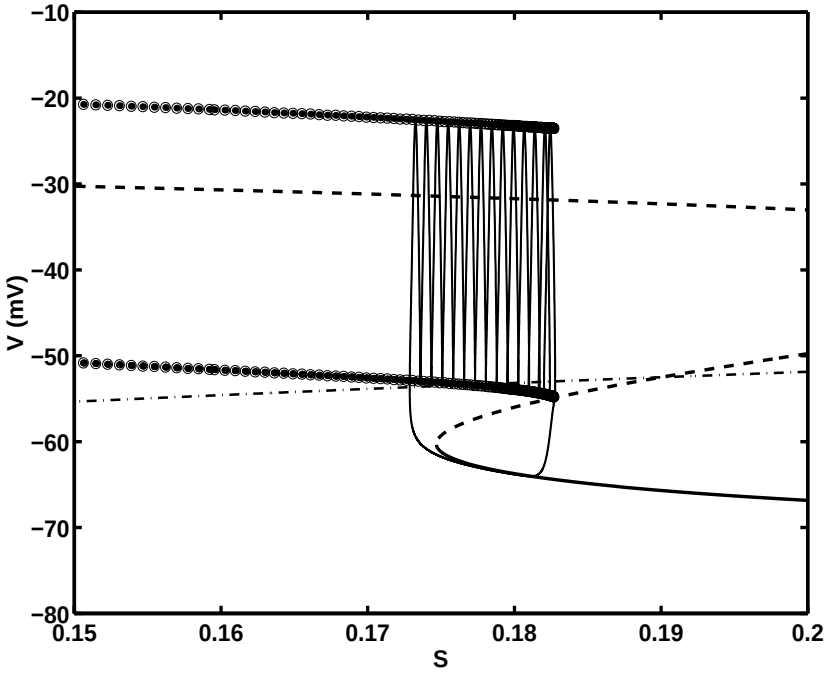

Figure 3.5. Phase portrait of the SRK equation superimposed on the bifurcation diagram. The dashed-dotted line is the S nullcline ($\dot{S} = 0$). See explanation in text.

3.3 Singularly Perturbed Dynamical Systems

Bursting is but one of many dynamical modes of a singularly perturbed (SP) model and many different types of dynamics are possible depending on the parameters. In order to get a qualitative description of these dynamics, we restrict our attention to a set of singularly perturbed differential equations in (2,1), *i.e.* a planar fast subsystem with 1 slow variable. Thus we have the following differential equation in $\mathbb{R}^{(2+1)}$ (1 slow variable):

$$\dot{X} = f(X,Y) \tag{3.11}$$

$$\dot{Y} = \varepsilon g(X,Y) \tag{3.12}$$

or

$$\varepsilon X' = f(X,Y) \tag{3.13}$$

$$Y' = g(X,Y), \tag{3.14}$$

where $'$ denotes differentiation with respect to $T = \varepsilon t$ (the slow time). Eqns. 3.11-3.14 show our two points of view of analysis of the SP equations, namely in the fast and the slow time scales. Since the bifurcation structure of two dimensional vector fields is relatively well understood [9, 64], restricting the fast subsystem to 2 variables allows the analysis of generic features of the SP. However, (an important technical point) the $\varepsilon = 0$ limit is singular, and the limiting equations with $\varepsilon = 0$ do not really describe the situation $\varepsilon > 0$. For $\varepsilon = 0$, the parameters do not vary in time. Careful analysis must establish that the invariant manifolds and attractors that exist for the singular limit also exist for $\varepsilon > 0$. The trajectories of the SP_0 equations (we use the subscript to denote the value of ε) contain segments that

evolve on the invariant subspaces (subspaces of the phase space that are invariant under the flow, for example, fixed points, limit cycles or trajectories that connect fixed points) on the slow time scale (segments S) and segments that connect different invariant subspaces on the fast time scale (F). The transitions S-F or F-S occur at the bifurcations of the fast subsystem, with the slow variables treated as parameters.

An analysis of the bifurcations of planar vector fields allows classification of different types of transitions. We have already seen examples of transitions in the SRK model at the bifurcation points of the fast subsystem (the saddle-node point and the homoclinic point). A major challenge in the theory of dynamical systems is the identification of the bifurcation structure of a planar vector field. In fact, the number of periodic orbits of an arbitrary polynomial planar vector field (2 first order ODEs), first posed by Hilbert as problem 16 of his famous list, is an unsolved problem. Even partial answers for particular cases requires rather sophisticated mathematical machinery. Given the wealth of parameters in neural models, can we hope to uncover the general structure of even planar models? We give a small laundry list of known bifurcations (one and two parameter cases) for general planar ODEs which can be found in neural models. A detailed discussion of the asymptotics and structure of these bifurcations can be found in any book on dynamical systems such as [9, 64].

3.3.1 Generic Bifurcations

The bifurcation point of a vector field is a degenerate structure: the situation is very different on either "side" of the critical parameter values at the bifurcation. The nature of the bifurcation depends on the number of parameters required to "unfold" the bifurcation. The parameters form a manifold of n dimensions equal to the number of parameters required to break the degeneracy, called the codimension

of the bifurcation. More simply, the codimension of a bifurcation is the number of zero conditions required to specify a bifurcation. *E.g.*, the Hopf bifurcation is specified by a zero trace and non-zero determinant, so that it is of co-dimension one.

3.3.2 Codimension-One

Saddle-Node Bifurcation: If the linearization of the vector field has a single zero eigenvalue, with the remaining eigenvalues having nonzero real parts, then the trajectories near the bifurcation are determined by:

$$\dot{x} = f(x, \mu) = \mu - x^2. \tag{3.15}$$

The steady states are a parabola in the $\mu - x$ plane, with no fixed points for $\mu < 0$, and 2 fixed points, one stable and one unstable for $\mu > 0$.

Hopf Bifurcation: When the linearization of the vector field has a pair of complex conjugate eigenvalues which cross the imaginary axis, a periodic orbit is born from a fixed point. Depending on the structure of the vector field, the periodic orbit may be stable or unstable, and the bifurcation is supercritical or subcritical respectively. Near the Hopf bifurcation the trajectories are governed by:

$$\dot{x_1} = \omega x_1 - x_2 + (x_1^2 + x_2^2)x_1 \tag{3.16}$$

$$\dot{x_2} = x_1 + \omega x_2 + (x_1^2 + x_2^2)x_2, \tag{3.17}$$

where ω is the frequency of the oscillations.

Saddle Connections: The saddle points created at saddle-node bifurcations are characterized by a one dimensional stable and a one dimensional unstable subspace. In general, these subspaces do not intersect. However, at special points the two subspaces cross each other transversally (not tangentially). These transveral intersection points are points of infinite period orbits or saddle loops. We have already

seen a saddle loop (or homoclinic) orbit in the SRK model, which led to a transition from the active to the silent phase. These bifurcations have not been extensively studied for SP systems, except for different models of β-cell bursters by Pernarowski [65, 66], using a combination of analytical and numerical methods. These β-cell models fortuitously are perturbations of Hamiltonian systems, for which a rigorous theory for finding points of homoclinic orbits exists. The most familiar homoclinic orbit is the separatrix for a simple pendulum. Other models, in general, will not be close to Hamiltonian, and techniques for locating homoclinic orbits in dissipative systems need to be applied and developed [67].

Connections between saddle points and sinks (or sources) are called heteroclinic orbits, but we are not aware of any models of bursting where these play a role.

SNIC (Saddle-Node-Loop): This situation occurs whenever the unstable manifold of a saddle point coincides with the stable manifold of a sink, forming a large loop that takes infinite time to traverse. Thus the name saddle node on invariant circle (SNIC). As the parameters are varied, the saddle and node collide, leaving a periodic orbit. This bifurcation is very important for most neural models which oscillate. The oscillation frequency at the onset of the SNIC bifurcation is small, and increases as a square-root of the bifurcation parameter, which is observed in experiments on neurons (the parameter is the applied current). The frequency of oscillations at the bifurcation point is infinite, and decreases as the parameters applied current increases, in contrast to the HH case, where the frequency is discontinuous at the bifurcation point and approximately constant.

Saddle Node of Periodics: In this situation, the linearization of the Poincaré map of the periodic orbit has an eigenvalue 1. This situation is analogous to the saddle node bifurcation encountered above, but now it denotes the coalescence and disappearance of stable and unstable periodic orbits.

3.3.3 Codimension-Two

The list of codimension-2 bifurcations is not complete, and their analysis requires a careful asymptotic analysis on a case-by-case basis. Some commonly encountered bifurcations are listed below.

Cusp: Consider a one dimensional dynamical system of the form:

$$\dot{x} = f(x, \lambda), \quad x \in \mathbb{R}, \quad \lambda \in \mathbb{R}^n, \ n > 1, \tag{3.18}$$

at an equilibrium point x_c for some λ_c, such that $f(x_b, \lambda_b) = 0$. The equilibrium is a cusp, if the following conditions are satisfied:

$$\left.\frac{\partial^2 f}{\partial x^2}\right|_{x_b,\lambda_b} = 0 \quad \text{but} \quad \left.\frac{\partial^3 f}{\partial x^3}\right|_{x_b,\lambda_b} \neq 0, \tag{3.19}$$

along with the appropriate transversality conditions. The cusp bifurcation point is an intersection of two curves of saddle-node bifurcation points.

Degenerate Hopf: The periodic orbits born at a Hopf point can be sub- or supercritical. The degenerate Hopf points form a curve in parameter space separating the subcritical and supercritical Hopf bifurcations.

Takens-Bogdanov (Double Zero): The linearization of the planar vector field for the fast subsystem can be written as a 2×2 matrix. This matrix can have zero trace and determinant at discrete points in a two-dimensional parameter space, implying a zero eigenvalue of multiplicity 2. Such points are called Takens-Bogdanov bifurcation points, after the two authors that first studied them [9]. An unfolding of these singularities shows small periodic and homoclinic orbits nearby.

Other bifurcations include heteroclinic cycles, with trajectories connecting different fixed points forming a closed orbit. We do not discuss these as they do play a role in most physiological examples of bursting.

As an epilogue to this section, we mention that the $\varepsilon = 0$ limit is indeed singular. The bifurcations discussed above consider that the slow variable is actually constant.

In the full model, with $\varepsilon > 0$, the slow variables evolve, subtly modifying the static bifurcation picture. For concreteness, let us consider a situation where the fast subsystem undergoes a Hopf bifurcation at $\mu = \mu_H$. Thus, for parameter values $\mu < \mu_H$ (μ constant), the rest state is stable. As μ increases past μ_H, the rest state loses stability to a stable periodic orbit. However, if μ is now allowed to vary slowly through the bifurcation point, paradoxically, the transition to a periodic orbit at μ_H disappears! Instead, the trajectory tracks the unstable rest state closely. The periodic orbit appears well above the critical parameter value. Thus, what one observes for $\varepsilon = 0$ differs qualitatively from the case of $\varepsilon > 0$. Nejshtadt first investigated this phenomenon, termed delayed loss of stability [68]. Delayed loss of stability is not restricted to the Hopf bifurcation, but occurs for the saddle-node and transcritical bifurcations[64] as well . Thus, viewing the bifurcation points of the fast subsystem as the transitions between different segments of the slow subsystem is only approximate. The delayed stability loss must be taken into account to estimate the transition points. Guckenheimer has outlined steps towards a global theory of SP models and discussed the dynamics of maps that describe successive F-S and S-F transitions [69].

3.4 (Weakly) Coupled Bursters

The principal motivation for the development of a framework for analysis of bursters comes from various physiological observations in biology. Best studied among these is the β-cell burster in the pancreas. These cells are responsible for the secretion of insulin in response to glucose. Abnormalities in their function result in diabetes. The considerable health related implications of diabetes require a better understanding of burst generation. β cells in the pancreas, however, do not burst by themselves, but cluster in arrays called islets and couple to neighboring cells by gap junctions

(small conducting pores that have a low effective electrical resistance). A number of these cells act in concert, resulting in the secretion of insulin by an islet. The β-cell islet is not a unique example of biological coupled oscillations, and assemblies of coupled oscillating cells are rather common (see Chapter 3).

The coupling between two cells can either be via a gap-junction, which we term diffusive (since the resistive coupling of the form, $g_{gap}(V_1 - V_2)$ is a discrete version of diffusion), or chemical (for example, synaptic coupling, where the activity of a cell results in the release of a chemical which influences the state of another cell in the network). We postpone the discussion of synaptic coupling to Chapter 4 where we analyze models of neural oscillators coupled by synapses, and concentrate here on networks of diffusively coupled cells. Again, diffusive coupling is natural when considering chemical reactions such as the Belousov-Zhabotinsky [70] reaction since the chemicals in solution diffuse.

The simplest network of coupled oscillators is a two cell network with reciprocal diffusive coupling between the two elements. We consider models of bursters with diffusive interactions and outline methods for their analysis. The relevant questions are: Does the bursting behavior of individual cells survive in the network? Does the bursting behavior change in some predictable way? Sherman has studied the dynamics of a pair of coupled SRK models with diffusive interactions [62], using an extension of the geometrical perturbation theory outlined above. We will follow a similar approach to illustrate some of the new phenomena that arise in coupled bursters. We shall consider a pair of bursters with two fast and one slow variables and explore their dynamics using numerically constructed bifurcation diagrams. The coupled equations are now a SP vector field in $\mathbb{R}^{4+2}$ (i.e. (4,2)), with four fast and two slow variables. The bifurcation structure of four dimensional vector fields is very hard to analyze completely because several global bifurcations appear in the

enlarged phase space. However, some progress is possible because of symmetries in the equations peculiar to diffusively coupled models.

For concreteness, we consider the dynamics of each cell to be governed by the (2,1) SP vector field originally studied by Pernarowski [71] and further extended by deVries [66]. The equation for a single cell with coupling is:

$$\dot{v_1} = -\frac{a}{3}v_1^3 + a\hat{u}v_1^2 + (1 - a(\hat{u}^2 - \eta^2))v_1 - w_1 - z_1 + g_{gap}(v_2 - v_1) \quad (3.20)$$

$$\dot{w_1} = (1 - \frac{a}{3})v_1^3 + a\hat{u}v_1^2 - (2 + a(\hat{u}^2 - \eta^2))v_1 - 3 - w_1 \quad (3.21)$$

$$\dot{z_1} = \varepsilon(\beta(u - z_1)), \quad (3.22)$$

where $a,\ \hat{u},\ \eta$ are fast subsystem parameters and β is a slow subsystem parameter; v is equivalent to the voltage variable; w is the channel variable (analogous to the variable n for the SRK model) and z is the slow variable. The subscripts denote the index of the oscillator, and another set of three ODEs represent the second oscillator, with the indices interchanged. The cubic polynomial terms in the fast equations are sufficiently general so that Eqns. 3.20-3.22 can display most of the bursting behavior in Figure 3.2 [66]. We fix the parameters $\hat{u} = 1.5$, $\eta = 0.75$ so that each uncoupled cell has a square wave bursting pattern similar to the SRK model. The bifurcation diagram of a single cell looks qualitatively similar to that of the SRK model. The upper steady state loses stability via a Hopf bifurcation at $z = -1.640616$. The resulting periodic orbit disappears in a homoclinic bifurcation at z =1.706126 in a teardrop shaped loop of infinite period. An additional Hopf bifurcation occurs near $z = 5$, but disappears immediately in a homoclinic bifurcation, playing no role in bursting.

We show the time evolution of the voltage variable of the two cells in Figure 3.6a for a small value of the coupling strength g_{gap}. Clearly, the burst solution still persists, but the fine structure of the spikes changes. A magnified view of the

active phase (Figure 3.6b.) shows that the two cells spike π radians out of phase. Figure 3.6c shows that the slow variables z_1 and z_2 are very close to each other. We shall make use of this last observation to analyze the network dynamics.

We note that Eqns. 3.20-3.22 are symmetric with respect to an interchange of the indices of the oscillators, *i.e.*, if $(v_1,\ w_1,\ z_1,\ v_2,\ w_2,\ z_2)$ is a solution, its symmetry couterpart, $(v_2,\ w_2,\ z_2,\ v_1,\ w_1,\ z_1)$ is also a solution. The four dimensional fast subsystem with $\varepsilon = 0$, has 3 parameters, namely $g_{gap},\ z_1$ and z_2. Since numerical integration of the full equations shows that the $z_1 \sim z_2$ (upto first order in ε), we need only consider the $z_1 - g_{gap}$ plane in parameter space to unfold the dynamics. Also, because of the exchange symmetry, all solutions occur with multiplicities of 2. In the following, we shall construct numerical bifurcation diagrams to illustrate the solution structure. An analytical treatment of some solutions is certainly possible, but distracts from an understanding of the bursting oscillations. We shall mention the steps required for analytic exploration whenever possible.

Figure 3.8 shows the bifurcation diagram for the coupled fast subsystem. The original Z shaped steady state curve persists for the steady states with both oscillators at rest. The diffusive coupling does not change these states. Furthermore, two small Z shaped curves bifurcate from the the knees of the large Z. These secondary Z-curves are asymmetric steady states, with $v_1 > v_2$ and its symmetric counterpart. The original Hopf bifurcation at $z = z_H$ persists, along with the second Hopf bifurcation near $z = 5.0$. These Hopf bifurcations are the in-phase (IP) periodic orbits. In addition, two more Hopf bifurcations, one at z =1.8 and one near the saddle node point $z \sim 5$, occur on the main Z curve which are the anti-phase (AP) periodic orbits.

The IP branch is initially stable close to the Hopf bifurcation, but loses stability through a pitchfork bifurcation (one stable solution for $\mu < \mu_c$ and 3 solutions (2

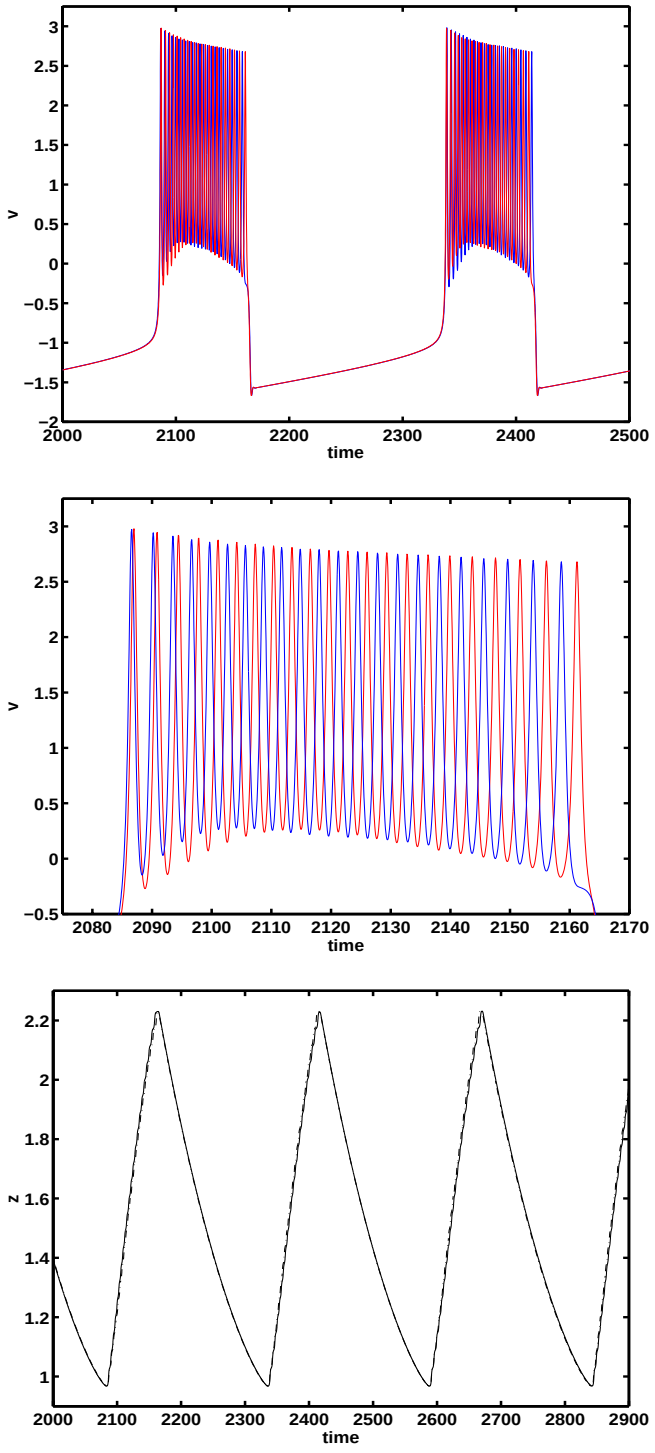

Figure 3.6. Time integration of coupled bursters with $g_{gap} = 0.025$. a) Time evolution of $v_1,\ v_2$. b) Blowup of a) showing anti-phase spikes. c) Time evolution of slow variables z_1 and z_2.

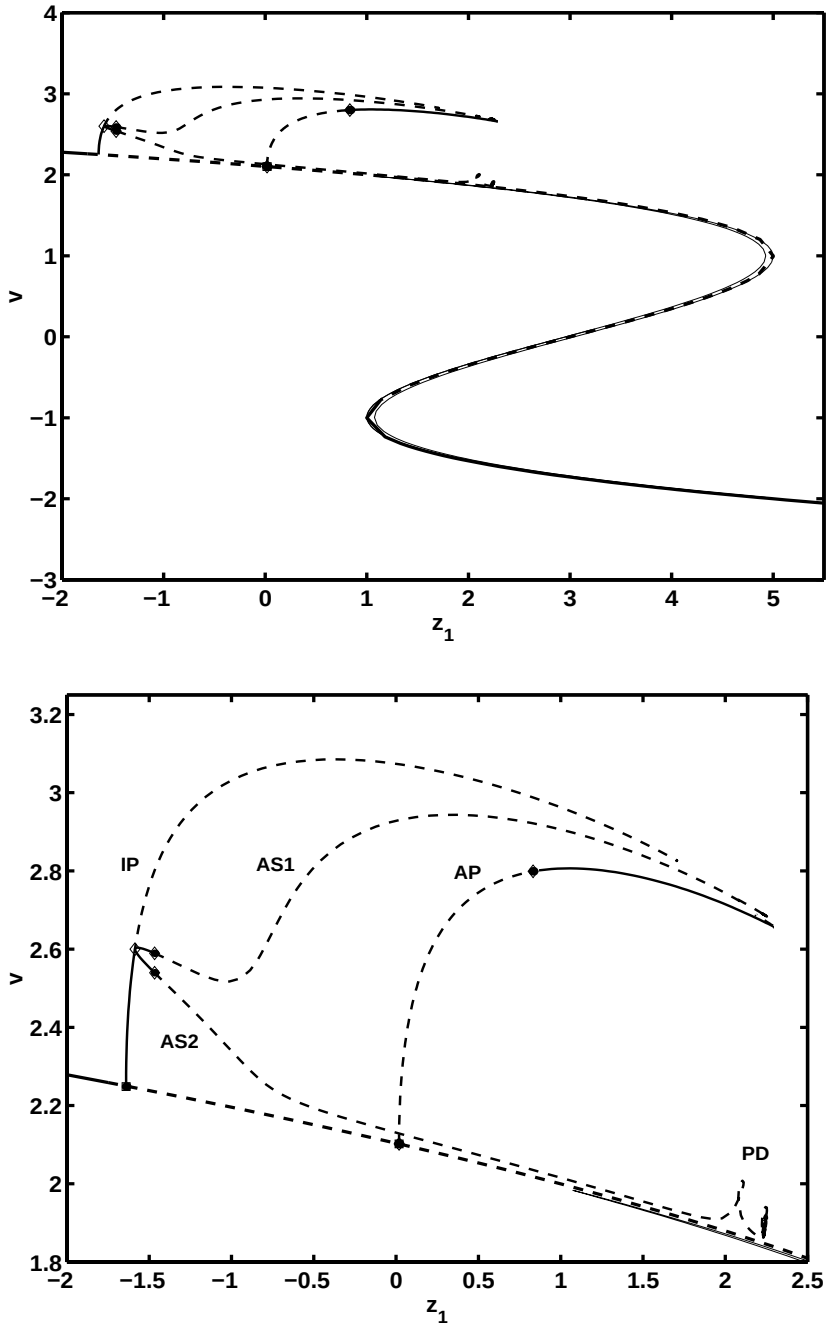

Figure 3.7. Bifurcation diagram for the fast subsystem of the coupled bursters, Eqn. 3.20-3.22. Top panel shows the full diagram and bottom panel shows a blowup. Heavy lines are steady states, dashed thin lines are maximum values of unstable periodic orbits and solid thin lines are maximum values of stable periodic orbits. Filled squares are Hopf bifurcation points, filled diamonds are torus bifurcations, and open diamonds are pitchfork bifurcations. The Z shaped curve (see text) appears solid throughout because the two asymmetric steady states are close to the symmetric branches. The stability is as indicated in the text.

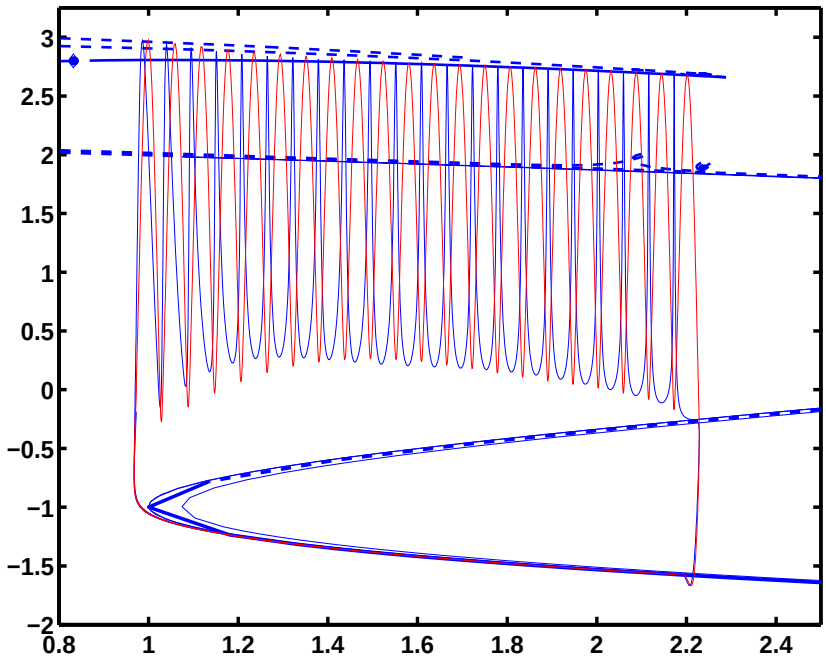

Figure 3.8. Blowup of the burst superimposed on the bifurcation diagram of two coupled bursters.

stable and 1 unstable) for $\mu > \mu_c$, where μ is any generic parameter), leading to a pair of asymmetric periodic orbits: one oscillator has large(r) amplitude oscillations, while the other has small(er) amplitude oscillations. These asymmetric branches (AS1 and AS2) in Figure 3.8 undergo a series of bifurcations where a pair of Floquet multipliers go thorough 1 (torus bifurcations), and finally disappear in a homoclinic orbit after a series of period doubling bifurcations (PD in the bottom panel of Figure 3.8). However, these asymmetric solutions are unstable throughout the range of z (except in the vicinity of the pitchfork bifurcation) and do not play a role in bursting for low g_{gap}. The AP branch is initially unstable, but gains stability through a torus bifurcation, and disappears in a saddle-node of periodics (SNP) bifurcation (one Floquet multiplier goes through 1), The unstable branch of antiphase periodic orbits, born at the SNP bifurcation, finally disappears in a homoclinic orbit at $z \sim 2.9$. A close look at the bursting trace reveals the following pattern: the silent phase of the burst ends near the saddle-node point at $z = 1.0$, as before. The active phase tracks the unstable in-phase branch transiently. Then the trajectory follows the stable AP branch as z increases. The active phase terminates near the homoclinic bifurcation of the AP branch. This structure resembles the active phase for a single burster which terminates at the homoclinic bifurcation of its periodic orbit.

Thus we see that weak gap junctional coupling still preserves the bursting solution, but alters the fine structure of the burst. More importantly, the active phase period is longer for the network than for the single cell, and the spike amplitude is reduced for these AP solutions. Physiologically, the length of the active phase determines the amount of insulin secretion. This result implies that coupled β-cells can secrete larger amounts of insulin than single cells. Perturbation techniques give leading order approximations to the duration of the active and silent phases [65]

for the uncoupled oscillator. The active phase begins at the saddle-node point and ends at the homoclinic point. The saddle point can be analytically computed from the linearized vector field, and Melnikov's method gives a leading order ($\mathcal{O}(\varepsilon)$) approximation to the homoclinic point. For two coupled bursters, the saddle point is unchanged, but the homoclinic point shifts to larger values of z (see Figure 3.7), lengthening active phase duration.

A two parameter bifurcation diagram in $\{z_1, g_{gap}\}$ allows us to trace the parameter regimes where an AP solution is stable. We show such a diagram in Figure 3.9, where we have traced the AP Hopf bifurcation point, the AP torus bifurcation point (where AP becomes stable), and an approximation to the AP homoclinic. We see that for zero coupling, the AP Hopf point and torus point merge into the IP Hopf point at $z = -1.640616$. The AP homoclinic merges with the IP homoclinic. The AP Hopf curve intersects the line SN2, indicating a second Hopf bifurcation near the saddle-node point. The second AP limit cycle born at SN2 also undergoes torus and homoclinic bifurcations. Horizontal cuts in this figure at any give g_{gap} value between the lines SN1 and the homoclinic curve show the z range for the active phase. The oscillators jump up synchronously at the SN1 point, follow the AP branch and jump down at the AP homoclinic point. The AP branch is stable in the region between the curves of torus points and homoclinic points.

As g_{gap} increases, the parameter range where the AP solution is stable shrinks continuously. For $g_{gap} > 0.06$, the AP branch is unstable, as the torus bifurcations on the left and right AP branches merge. For $g_{gap} > 0.072$, the AP branch disappears completely, but numerical experiments show that the bursts still persist, but are no longer periodic (Figure 3.10). The spike patterns within the bursts are asymmetric, with large amplitude oscillations for one oscillator, and small amplitude oscillations for the other, which alternate from burst to burst. The phase difference between

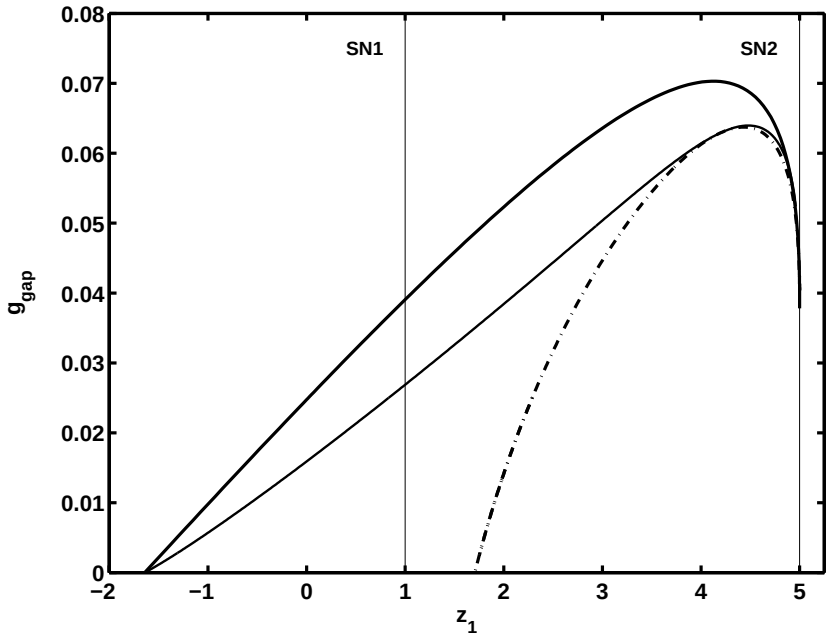

Figure 3.9. Two parameter bifurcation diagram for the fast subsystem of two coupled bursters. The thick solid line shows the curve of AP Hopf bifurcations. The thin solid line is the curve of torus bifurcation points of the AP limit cycle. The dashed line is the approximation to the AP homoclinic bifurcation. The two vertical lines SN1 and SN2 are the lines of saddle-node bifurcations.

the two oscillations also oscillates about π. We term these solutions asymmetric, phase trapped solutions, where the amplitudes and phase differences are periodic with some period T, which may or may not be commensurate with the basic period of the oscillations. We conjecture that these solutions are tertiary branches, arising from the AP branch, which AUTO cannot follow. The approximation $z_1 = z_2$ fails for larger values of the coupling strength or different values of the parameters $\{\hat{u},\ \eta\}$.

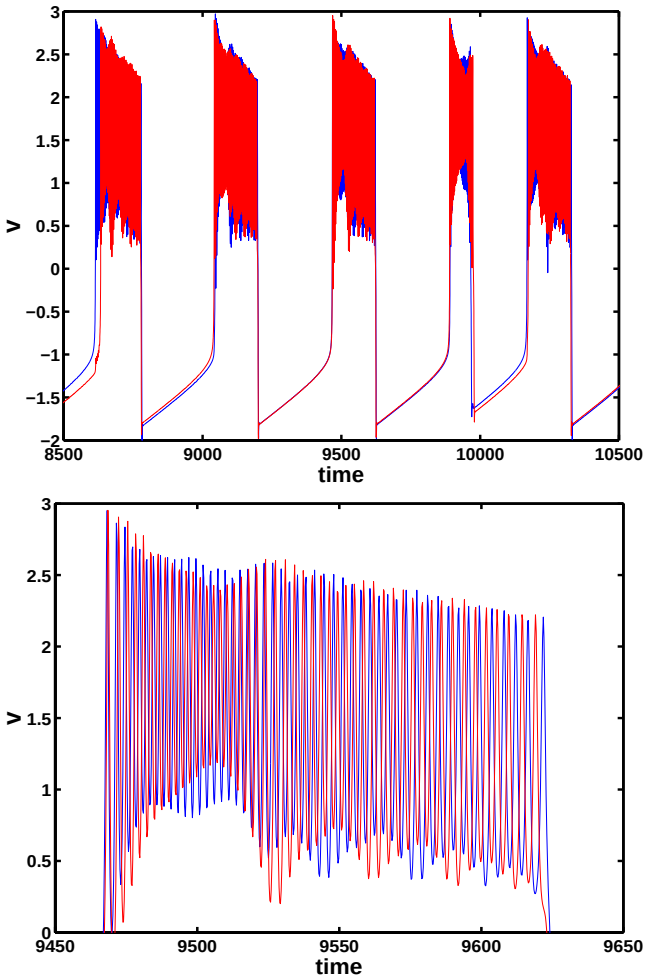

Figure 3.10. Time integration of coupled bursters with $g_{gap} = 0.075$. Top panel: Time evolution of $v_1,\ v_2$. Bottom panel: Blowup of showing phase trapped spiking within the burst

The above numerical experiments clearly suggest that the periodic orbits of the fast subsystem govern the dynamics during the active phase of the coupled cells. Thus a local theory near the Hopf bifurcation can tell us much about the qualitative nature of the periodic solutions for the 4-dimensional fast subsystem. Transitions to and from the active phase depend on bifurcations of other steady states or global bifurcations, which are beyond the scope of any local theory. We next show that a normal form reduction of the fast subsystem around the Hopf bifurcation shows that active phase oscillations are generically either antiphase or asymmetric, phase trapped.

Recall that the fast subsystem defines a vector field in $\mathbb{R}^4$ as follows:

$$\frac{d\mathbf{X}_1}{dt} = \mathbf{F}(\mathbf{X}_1;\mu_1) + \mathbf{D}_1(\mathbf{X}_2 - \mathbf{X}_1), \tag{3.23}$$

$$\frac{d\mathbf{X}_2}{dt} = \mathbf{F}(\mathbf{X}_2;\mu_2) + \mathbf{D}_1(\mathbf{X}_1 - \mathbf{X}_2), \tag{3.24}$$

The vector valued functions $\mathbf{F}(..)$ are identical, $\mu_1 = \mu_2$ and the coupling $\mathbf{D}$ is a 2×2 matrix of the form:

$$\begin{pmatrix} g_{gap} & 0 \\ 0 & 0 \end{pmatrix}. \tag{3.25}$$

The steady state $\mathbf{X}_1^*, \mathbf{X}_2^*$ undergoes a Hopf bifurcation at $\mu = \mu_{Hopf}$. We linearize about this steady state and obtain the following coupled equations:

$$\frac{d\mathbf{u}_1}{dt} = (\mathbf{A} + \lambda\mathbf{B})\mathbf{u}_1 + \mathbf{N}(\mathbf{u}_1) + \eta\mathbf{D}(\mathbf{u}_2 - \mathbf{u}_1), \tag{3.26}$$

$$\frac{d\mathbf{u}_2}{dt} = (\mathbf{A} + \lambda\mathbf{B})\mathbf{u}_2 + \mathbf{N}(\mathbf{u}_2) + \eta\mathbf{D}(\mathbf{u}_1 - \mathbf{u}_2), \tag{3.27}$$

where $\mathbf{u}_i$ are vectors in $\mathbb{R}^2$, $\mathbf{A}, \mathbf{B}$ and $\mathbf{D}$ are real matrices, λ and η are scalar parameters, and $\mathbf{N}(..)$ is a thrice differentiable, smooth function. $\mathbf{A}$ has a pair of imaginary eigenvalues. The matrix $\mathbf{D}$ contains the coupling terms, and $\mathbf{B}$ describes the linear part away from criticality.

With the coupling coefficient set to zero, Eqns. 3.26-?? split up into a pair of independent 2-dimensional subsystems each with an asymptotically stable limit cycle $\Omega_0 = (\sqrt{\lambda}\cos(\omega t), \sqrt{\lambda}\sin(\omega t))$. The product system has an attracting invariant torus $T_0 = \Omega_0 \times \Omega_0 \in \mathbb{R}^4$ such that all initial conditions except zero converge exponentially fast to the torus. A family of solutions, parametrized by the two initial phases of the oscillators covers the torus. However, since the vector field is autonomous (no explicit time dependence), it is invariant to time-translation. Hence, only a single parameter, namely the phase difference, suffices to parametrize the family of solutions. For non-zero coupling, we do not expect this degenerate structure to persist. Invariant manifold theory [72] implies that the attracting torus will persist for small coupling, perhaps changing its shape and position, but remaining smooth and close to the original torus T_0. While the invariant torus as a whole survives, the structure of the orbits in the torus changes. We note that coupling strengths of the same order of magnitude as the nonlinear terms destroy the invariant torus, and invalidate this theory. In order to see which solutions persist, we note that the following subspaces are invariant under the flow:

$$\mathcal{I} = (\mathbf{u}_1, \mathbf{u}_2) | u_{1i} = u_{2i}, i = 1, 2, \tag{3.28}$$

$$\mathcal{A} = (\mathbf{u}_1, \mathbf{u}_2) | u_{1i} = -u_{2i}, i = 1, 2. \tag{3.29}$$

The two invariant subspaces $\mathcal{I}$ and $\mathcal{A}$ represent the in-phase and anti-phase solutions. In addition, there are two more invariant subspaces, $\mathcal{AS}_1$ and $\mathcal{AS}_2$, $(0 \times \Omega_0)$, and by symmetry, $(\Omega_0 \times 0)$. The $\mathcal{AS}_i$ are the two asymmetric solutions that arise from pitchfork bifurcations from the IP branch in Fig. 3.8. Averaging methods [9, 73], show that these four are the only solutions that persist and any other periodic solutions arise via bifurcations from these basic solutions. The averaged equations also give the stability of these solutions. The flow in $\mathbb{R}^4$ now reduces to the flow

on the two 2-dimensional subspaces, $\mathcal{I}$ and $\mathcal{A}$. The reduced equations have an additional symmetry: if ($\{z_i\}$ is a solution then $\{-z_i\}$ is also a solution. This extra symmetry, of course, is not a symmetry of the original equations, and we must discard any such solutions.

We can write Eqns. 3.26-?? in polar form as:

$$r_1' = r_1(1-\gamma-r_1^2) + r_2\gamma(\cos(\phi) - \eta\sin(\phi)) \quad (3.30)$$

$$r_2' = r_2(1-\gamma-r_2^2) + r_1\gamma(\cos(\phi) + \eta\sin(\phi)) \quad (3.31)$$

$$\phi' = q(r_1^2 - r_2^2) - \gamma\big[(\frac{r_2}{r_1} + \frac{r_1}{r_2})\sin(\phi) + \eta\{\frac{r_1}{r_2} - \frac{r_2}{r_1}\cos(\phi)\}\big], \quad (3.32)$$

where r_i are the amplitudes of the oscillations emerging from the Hopf bifurcation, ϕ is the relative phase difference between the oscillators, and γ and η are parameters that can be derived from the original equations. We have reduced the fast subsystem for a pair of coupled bursters (Eqns. 3.20-3.21) using a standard reduction proceduce [74] to the polar form shown above. We show the bifurcation diagram of the reduced equations as γ is varied in Figure 3.11.

In the reduced form, changing γ is equivalent to changing g_{gap} in the original equations. We can clearly see that for γ=0, the in-phase and anti-phase Hopf bifurcations merge. For low values of γ, the anti-phase oscillations are the only stable branch. The amplitude of oscillations decreases monotonically with γ. As γ in increased, the anti-phase oscillations lose stability via a Hopf bifurcation. This bifurcation corresponds to the birth of the phase trapped solutions that oscillate about a phase difference of π in the original equations (Figure 3.10). At γ=0.5, the anti-phase oscillations disappear. Note also the two branches of asymmetric oscillations, which correspond to oscillations where the two oscillators have different amplitudes. The branches of asymmetric oscillations arise from a pitchfork bifurcation of the in-phase branch. Thus, we have confirmed that the phase-trapped solutions indeed

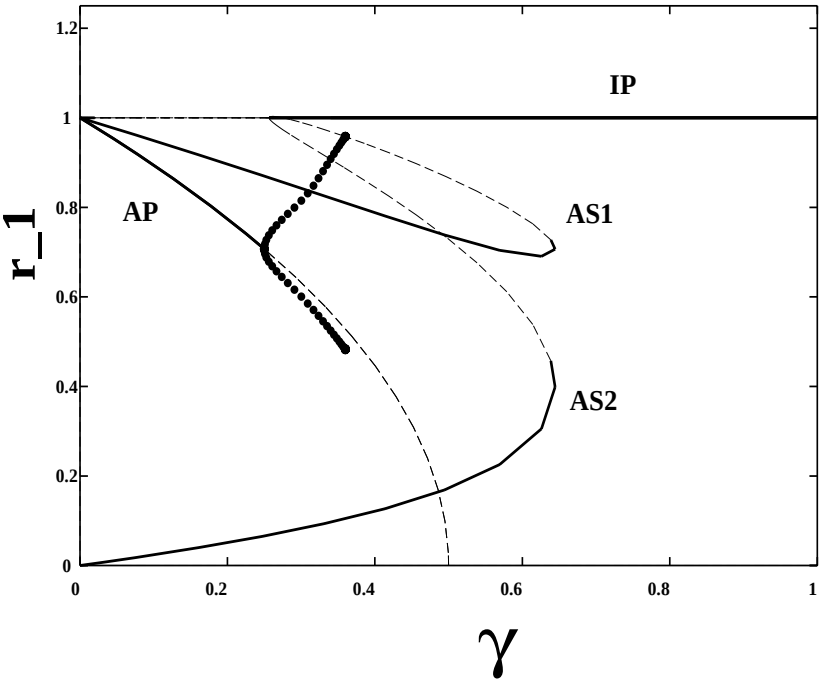

Figure 3.11. Bifurcation diagram of the reduced equations (Eqns. 3.30 -3.32 showing the steady states of the amplitude of oscillator 1 as a function of γ. Solid lines indicate stable solutions, dashed lines indicate unstable solutions and filled circles denote stable periodic orbits.

emerge from the anti-phase branch, and thus the relative phase difference oscillates about π. If the frequency of the emergent phase oscillations is incommensurate with the frequency of the original oscillations, then the spiking patterns in the burst looks quasiperiodic with an incommensurate period.

The fate of these solutions in the full model, well away from the Hopf bifurcation, depends on the presence of global bifurcations involving the stable and unstable manifolds of other fixed points, which cannot be deduced from a local analysis around the Hopf bifurcation. For example, the active phase in the above analysis terminates at the homoclinic orbit, which is a global bifurcation whose existence cannot be inferred from a local analysis. Again, symmetry arguments imply that the degenerate homoclinic orbit, for zero coupling, splits up into two homoclinics for the IP and AP periodic orbits. The critical z value for the IP homoclinic for the coupled burster is the same as for a single burster. Qualitatively, since the AP amplitude is smaller than the IP amplitude, it intersects the saddle branch of the Z curve at $z^*(AP) > z^*(IP)$, thus shifting the AP homoclinic to higher values of z.

We have also numerically integrated Eqns. 3.20-3.22 for a few different values of $\hat{u}$ and η corresponding to different regions in the parameter space of a single cell and find very different patterns of bursting. However, the large number of parameters precludes a systematic analysis (just the fast subsystem of two identical cells has 3 parameters). Sherman [62] has analyzed the bursting in a network of two identical, coupled SRK model bursters using the same methods. For this more realistic model, the burst period for the coupled cells is longer than for the uncoupled cells. His analysis shows that the most common burst pattern is synchronous bursting with asymmetric, quasiperiodic spiking, which occurs in experiments. He also shows that non-identical cells, with different *slow* subsystem parameters, which may or may not burst singly, burst when coupled. In an earlier study of β-cell models with many

cells, Smolen *et al.* [75] showed that most of the cells in a cluster do not burst when uncoupled because the parameter regime for bursting for single cells is too narrow. However, when coupled, the whole cluster, which is a model for a islet in the pancreas, bursts robustly. The above analysis sheds some light on why the islet bursts even when single cells need not. The study of a two cell network is also important for understanding the dynamics of a spatially distributed model of the islet, which we explore in the next section.

3.5 Spatially extended models

3.5.1 Introduction

As a culmination of our analysis of coupled bursters, we will study a spatially extended model of bursting to loosely model an islet in the pancreas. The pancreas consists of millions of islets composed of endocrine cells. Insulin secreting β-cells make up about 80% of the cells in an islet. Individual β-cells conditionally burst depending on the glucose concentration. In an islet, these cells connect to each other by gap juntions. While models of single β-cells are well understood, models of coupled bursting elements are little analyzed. Smolen *et al.* have analysed such a model with heterogenous bursters [75]. Studies of networks of two coupled bursters [62] show that the burst solution depends on the coupling strength and several types of burst patterns arise in the same network.

One key question in models of large numbers of coupled bursters is the role of the strength of the gap junction coupling. The maximal effective conductance (a measure of coupling strength) of gap junctions has been measured in β-cells [76] in isolated cell pairs to be 0.174 ± 0.08 (in dimensionless units), which is rather weak compared to the maximal conductances of the various channels. What does this weak coupling imply for models of coupled bursters? Some experiments suggest

that the cells in the islet burst in synchrony on addition of glucose (see [66] for a review) but we are not aware of a definitive experiment that conclusively proves synchrony. However, we can model the effect of weak coupling on a field of bursters to determine whether the value for coupling strength for isolated cell pairs is in fact too weak to support synchrony.

We consider a generic polynomial model of bursting which allows analytic exploration and use a similar fast-slow decomposition to that for the single cell and two cell models. We show that the fast-slow decomposition of the continuum models leads to a two component reaction-diffusion equation for the fast subsystem. Reaction-diffusion equations are extensively used to study pattern formation in biology and chemistry. These equations are coupled parabolic PDEs of the form:

$$\frac{\partial \mathbf{u}}{\partial t} = \mathbf{f}(\mathbf{u}) + \mathbf{D}\nabla^2\mathbf{u}, \tag{3.33}$$

where $\mathbf{u}(\mathbf{x}, t)$ is the vector of dependent variables, $\mathbf{f}(\mathbf{u})$ is a nonlinear vector-valued function (the reaction term) and $\mathbf{D}$ is the diffusion matrix, representing the diffusivities of the various species, with suitable boundary conditions. The reaction terms represent chemical reactions, predator-prey interactions *etc.* Murray [77], Grindrod [78] and Britton [79] give excellent pedagogical reviews of the applications of reaction-diffusion equations in biology, chemistry and ecology and the analysis of their solutions.

If the reaction terms $\mathbf{f}(\mathbf{u})$ possess two stable equilibria, then the reaction diffusion equations can support solutions that connect these equilibria, called plane wave solutions. Bistable behavior of spatially extended models is common in biology, chemical reactions and models of fluid dynamics [80, 70, 81, 43, 82, 77].

A typical plane wave solution of reaction-diffusion equations in one dimension is a front solution, which is essentially a domain wall separating a metastable state from a stable equilibrium state. Under very general conditions, we can show that

the domain wall moves with a velocity, c, with unchanged shape, as the stable state takes over the whole domain. Establishing the velocity, c, of the front is a very delicate problem, depending on the topology of the reaction terms $\mathbf{f}(\mathbf{u})$. Fronts can have either a discrete set of velocities or a continuous family from which one velocity is selected [83]. The mechanism of selection is often unknown. Another typical solution is the pulse solution, where the whole domain is in the stable state, with a small patch of the metastable state, with the patch moving with a velocity c. Again, depending on the geometry of the solution of the reaction terms, the patch can be stationary in space.

The metastable and stable states need not be stationary in time, but can be time-dependent. The most common examples of time-dependent states are models of binary convection or oscillatory chemical reactions, where the spatially uniform equation has an unstable steady state with a limit cycle (the steady state has undergone a Hopf bifurcation). If the Hopf bifurcation is sub-critical (as in binary convection), the steady state and the oscillations are both stable for the same parameter values. A reaction-diffusion equation for this situation has traveling waves (front states), pulses and spatiotemporal chaos [80]. Bistability between stable oscillations and a stable fixed point can also arise for a different case, as we have seen for the fast subsystem of a single burster, where a stable limit cycle and a stable fixed point coexist for parameter values between a saddle-node bifurcation and a homoclinic bifurcation. This form of bistability has no equilibrium counterpart, since the periodic orbit breaks time translation invariance. Reaction terms of the above topological type occur in the Gray-Scott model of chemical reactions [84], semiconductor lasers *etc.*

The analysis of a field of coupled bursters also allows us to gain some insight into this important class of reaction-diffusion equations. The linearization of any vector

field with a homoclinic bifurcation has a double zero eigenvalue, and the remaining eigenvalues lie to the left of the imaginary axis (negative real part). The most generic form of this bifurcation (a normal form, in dynamical systems terminology) is the Takens-Bogdanov (T-B) normal form [9] given by:

$$U_{tt} + \mu_1 U_t + \mu_2 U + \alpha U^2 U_t + \beta U^3 = 0. \tag{3.34}$$

Argentina and Coullet [3] recently studied a model reaction-diffusion equation constructed from a symmetric T-B normal form, with additional terms that ensured a coexisting fixed point and limit cycle:

$$U_{tt} + \mu_1 U_t + \epsilon_1 U U_t + \alpha U^2 U_t + \mu_2 U + \epsilon_2 U^2 + \beta U^3 = U_{xx} + U_{xxt}, \tag{3.35}$$

where $\mu_1,\ \mu_2,\ \epsilon_1,\ \epsilon_2, \alpha$, and β are parameters. μ_1 and μ_2 are the unfolding parameters of the T-B normal form, and the remaining parameters are of order unity. ϵ_1 controls the number of fixed points for the spatially homogeneous equation. They set $\alpha = \beta = 1$, $\epsilon_1 = 0$, and $\epsilon_2 = a$. For a range of a, Eqn. 3.35 has 3 fixed points: a stable node, a saddle point and a stable focus. We give the phase portrait in Figure 3.12. At $\mu_1 = 0$, the focus undergoes a Hopf bifurcation to a stable limit cycle. As μ_1 increases, the amplitude of the limit cycle increases, till at $\mu_1 = \mu^* \sim 0.08$, it disappears in a homoclinic bifurcation. Thus, the limit cycle and the stable node are bistable for a range of μ_1..

The addition of the diffusion terms results in striking spatiotemporal dynamics, shown in Fig. 3.13. We start from random initial conditions about the unstable focus, with $\mu_1 > \mu^*$. For $\mu_1 < 0.12$, the whole domain oscillates in a chaotic manner about the unstable focus. For $\mu_1 > 0.12$, small patches of the metastable state (the stable node) begin to appear. Since these patches are metastable, they shrink and disappear, replaced by chaotic oscillations, which again nucleate metastable patches. The statistics of the widths of the metastable patches resembles the statistics of

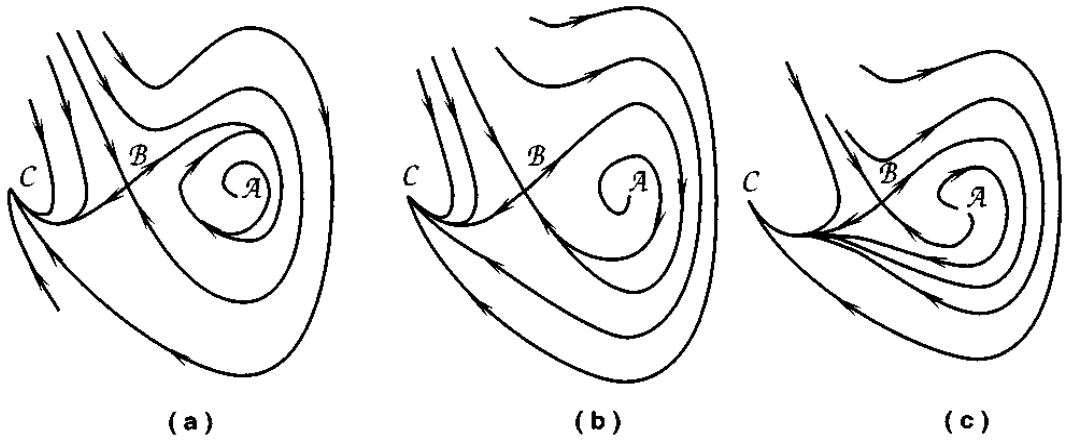

Figure 3.12. Phase portrait for Eqn. 3.35 showing the 3 fixed points: stable node (A), saddle point (B) and unstable focus (C).

laminar patches observed in spatiotemporal intermittency in amplitude equations [85, 12].

The above observation is our second motivation for studying models of diffusively coupled bursters. As shown before, a key ingredient for square wave bursting is bistability between a low voltage rest state and high voltage oscillations between a saddle node and a homoclinic bifurcation. Does the spatially extended model exhibit well defined bursts? *I.e.*, does the whole domain synchronously switch between active and silent phases? Note that oscillations within the burst need not be synchronous. Do diffusively coupled bursters also show similar spatiotemporal intermittency? If so, and if the gap junction coupling is indeed weak, pancreatic islets should secrete in chaotic bursts, which would have physiologically disastrous consequences. Physiological experiments on single islets show a smooth dose response to glucose which would imply spatiotemporally uniform dynamics rather than chaos. We answer these questions for a minimal (generic) model for bursting, using singular perturbation theory and techniques developed for reaction-diffusion equations.

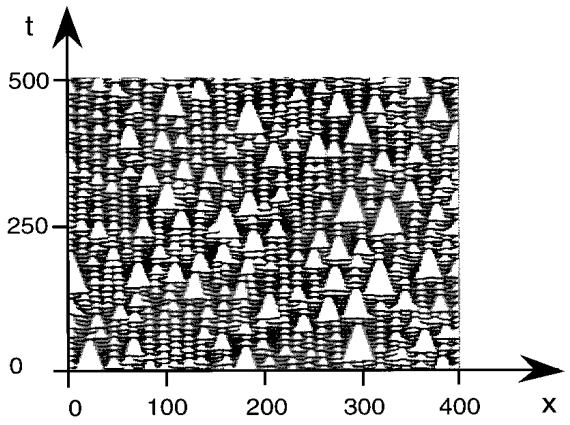

Figure 3.13. Numerical integration of Eqn. 3.35. The white triangular regions are the metastable phase, and the dark regions are chaotic oscillations. The numerically integrated values have been thresholded to distinguish the oscillating regions from the stationary state. From [3]

3.5.2 Wave phenomena in weakly coupled bursters

Several models describe the activity of single cell bursting. We consider the Hindmarsh-Rose equations [86], a simple polynomial model of bursting. The H-R model was originally developed to study bursting in thalamic cells, but are general enough to allow for different types of bursts. We choose a parameter set for which the H-R equations have a square wave bursting solution and study the dynamics of a field of H-R bursters with a weak resistive coupling between neighboring cells. In the continuum limit, resistive, gap junctional coupling between nearest neighbors of the form $V_1 - V_2$, is equivalent to diffusion.

The equations for a continuum model of coupled Hindmarsh-Rose model are:

$$v_t = w + 3v^2 - v^3 - \mu + Dv_{xx}, \tag{3.36}$$

$$w_t = 1 - 5v^2 - w, \tag{3.37}$$

$$\mu_t = \varepsilon(v - \frac{(\mu - z)}{4}), \tag{3.38}$$

where v is the voltage, w is a channel variable, D is the strength of diffusive coupling, μ is the slow variable, and z is a slow subsystem variable that controls the bursting. Taking the singular limit $\varepsilon \to 0,\ \mu(x) = \mu$, we obtain a planar reaction-diffusion equation with μ treated as a parameter. The bistability of the single cell model (in the singular limit) carries over to the reaction-diffusion equations. We will consider the equations over the real line and the initial conditions sufficiently localized in space.

We write Eqns. 3.36-3.37 conveniently in a Liénard form [9], *i.e.*, as a nonlinear oscillator with a small damping term. We differentiate the v equation with respect to t and use the w_t equation to eliminate w. The governing equations then become:

$$v_{tt} + G(v,\mu) + F(v)v_t = Dv_{xx} + Dv_{xxt}, \tag{3.39}$$

where $G(v,\mu) = v^3 + 2v^2 + \mu - 1$, which can be considered as the gradient of a potential $V(v) = \frac{v^4}{4} + \frac{2v^3}{3} + (\mu - 1)v$, and a damping term $F(v) = 1 + 3v^2 - 6v$. The roots of $G(v,\mu)$ give the fixed points of the equations, which typically have either one or three real roots depending on the parameter μ.

We show the bifurcation diagram of Eqns. 3.36-3.37 as a function of μ in Figure 3.14. The upper branch of steady states loses stability by a Hopf bifurcation at $\mu \sim -11.5$. The condition for the Hopf bifurcation is: $G(v_H, \mu_H) = 0,\ F(v_H) = 0$ and $G_v(v_H, \mu_H) > 0$. At $\mu \sim -0.1815$, a saddle-node bifurcation creates two additional steady state branches (middle: saddle; lower: nodes). As μ increases, the amplitude of the periodic orbit increases until it disappears through an Andronov homoclinic bifurcation at $\mu^* \sim 0.8$.

Since the damping term $F(v)$ is small ($\mathcal{O}(\delta),\ \mu \ll \delta \ll 1$ along the periodic orbit, Eqns. 3.36-3.37 without diffusion are a perturbation of a nonlinear oscillator of the van-der-Pol-Duffing type, with a potential function given by $\int_0^v G(u,\mu)du$. This analogy enables us to find a value for the homoclinic orbit using Melnikov

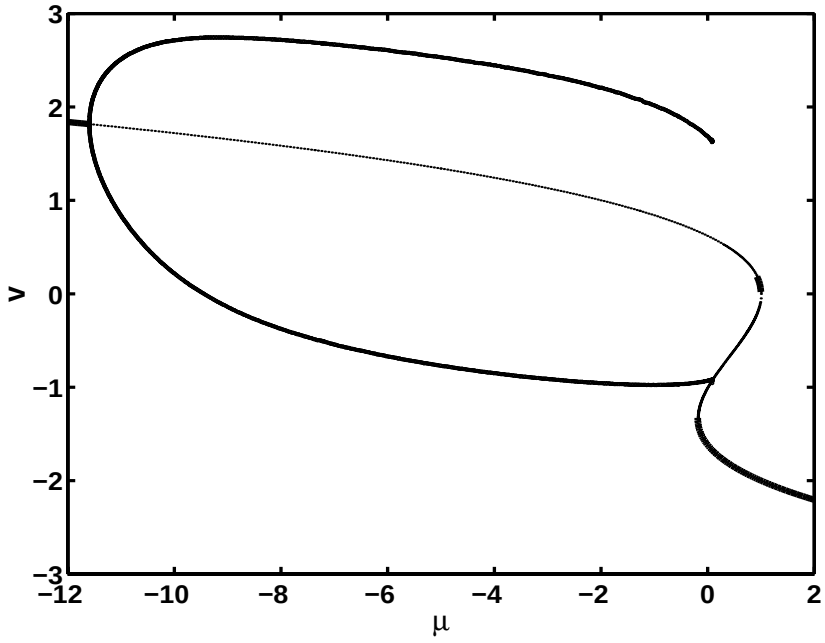

Figure 3.14. Bifurcation diagram for the Hindmarsh-Rose equations constructed using the automated bifurcation analysis software AUTO . Heavy lines indicate stable fixed points and thin lines indicate unstable fixed points. The equations have another Hopf bifurcation at $\mu = 0.8$ which terminates in a homoclinic bifurcation nearby, but plays no role in bursting or front propagation.

theory [65] to first order in δ as $\mu^* \sim 0.08$.

Since the diffusionless equations are bistable, we look for plane wave solutions of the reaction diffusion equations with $\varepsilon = 0$. First, we consider the homogeneous oscillations (the active phase for bursting) that emerge from the Hopf bifurcation of the upper steady state. We analyze the stability of this homogeneous oscillating state near criticality using an analysis similar to Kuramoto's [74]. We linearize the evolution equations (Eqns. 3.36-3.37) about the Hopf bifurcation and apply a solvability condition to obtain a complex amplitude equation for the periodic state of the form:

$$A_t = (1 - ic_2|A|^2)A + (1 + ic_1)A_{xx}. \tag{3.40}$$

The complex amplitude of the oscillations near criticality is $A = \sqrt{\mu}e^{-ic_2\mu t}$, and the coefficients c_1 and c_2 determine the nature and stability of the oscillations. We find that $c_2 > 0$, indicating a supercritical Hopf bifurcation. The coefficients c_1 and c_2 satisfy the Benjamin-Feir criterion [74], $\alpha \equiv 1 + c_1c_2 < 0$, implying that homogeneous oscillations are unstable to long wavelength fluctuations.

With nonzero coupling, the periodic orbit is no longer stable to localized perturbations. The Benjamin-Feir criterion implies that the Ginzburg-Landau equation, as well as the original equations are spatiotemporally chaotic [74, 87]. Moreover, the instability implies that the frequency of oscillations increases with increasing amplitude, while the presence of the saddle point causes the frequency to decrease with increasing amplitude (the periodic orbit approaches the infinite period homoclinic orbit). As the oscillations are spatiotemporally chaotic, small patches of large amplitude oscillations can develop, which then "escape"into the metastable state (the low voltage rest state). These chaotic oscillations are responsible for the nucleation of the metastable phase in [3]. Might we expect a similar nucleation of the metastable phase as for Eqn. 3.35?

In Figure 3.15, we show a numerical integration of the reaction-diffusion equations. Initial conditions are homogeneous oscillations, with a small phase-like perturbation at the left end. The perturbation grows and moves into the homogeneous oscillating regime, leaving behind a region of unsteady oscillations.

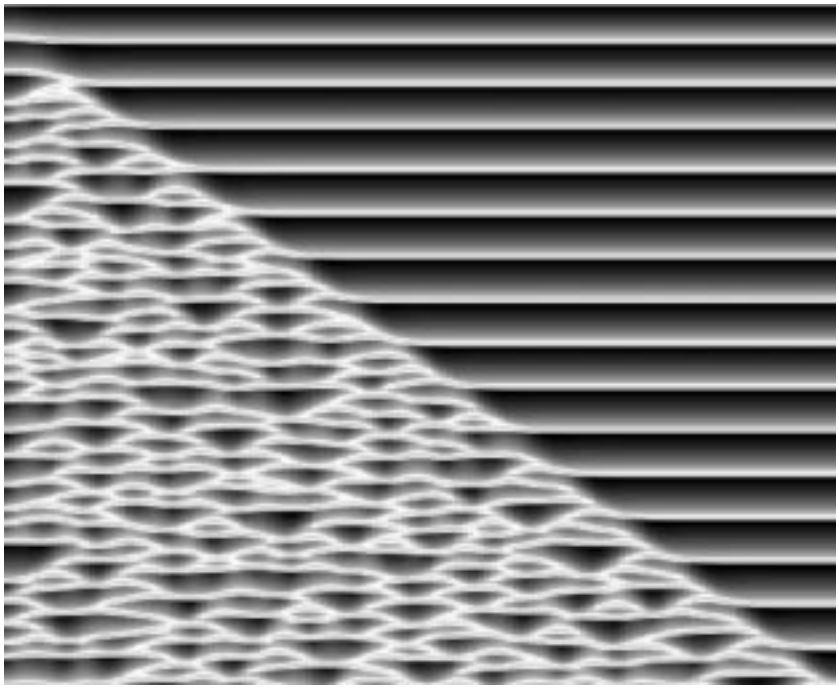

Figure 3.15. Numerical integration of Eqns. 3.36-3.37. Figure is color coded with light and dark regions indicating high and low values of the variable v. Length is 40 units and total time is 200. Space increases from left to right and time from top to bottom. $D = 0.2$, and $\mu = -0.15$. The grid size is 200 and Gear's method is used for integration. The system is started on the limit cycle with the left edge advanced by 0.05π in phase. The front separating the unsteady oscillations from the homogeneous oscillations moves with a velocity of approximately 0.2.

While the reduction to a Ginzburg-Landau form for the amplitude of oscillations is certainly valid for parameter values near the Hopf bifurcation, the values of μ in the bistable regime is an order of magnitude higher than its value at the Hopf bifurcation. Thus, a local analysis of the amplitude of oscillations might not hold in the bursting regime. We must consider the global effects of the stable and unstable

manifolds of the saddle point. As the periodic orbit passes close to the saddle point, parallel to the stable manifold of the saddle point (Figure 3.12), global effects cause a slow-down in the phase flow. The periodic orbit spends a long time near the saddle point, and speeds up away from it.

We give a qualitative explanation of the origin of the unsteady oscillations by an analysis similar to [88], and examine the dynamics. Although the coupling is only in the v variable, the oscillators can differ in both variables (v and w) along the limit cycle. The saddle point introduces strong deformations of the phase flow. If the trajectories of two interacting oscillators come close to the limit cycle, but their phases are slightly different, the interaction drives them away from the limit cycle. The lagging oscillator is pushed out and slows down as it travels along the stable manifold of the saddle point. The leading oscillator is pushed in and departs from the limit cycle. Away from the saddle point, the limit cycle attracts nearby points and synchronizes the oscillators. The phase portrait (a plot of $v(x)$ with $w(x)$) for any location behind the front is thus dense and completely fills the region bounded by the phase portrait of the periodic orbit of the diffusion-less equations. While this line of reasoning qualitatively explains the instability of homogeneous oscillations, the existence of a front solution and separating the homogeneous oscillations and the the irregular ones, as well as the front speed must be inferred by other means. This analysis is one of the open questions arising from this work.

Figure 3.16 shows the numerical integration of the equations, with the initial conditions set at the lower fixed point, with a small patch excited close to the upper fixed point. We see a front advancing to the right with a constant velocity, leaving behind a region of unstable oscillations, much like the ones observed in the case of the propagation of a phase-like disturbance into the homogeneously oscillating region. A uniform state corresponding to the upper fixed point cannot be established since

this state is unstable for the original reaction equations. A modulated oscillatory state about this fixed point is also ruled out since the wavenumber selection by the front competes with the dephasing interaction and renders the oscillations unstable. Therefore, the front leaves behind a region of irregular oscillations.

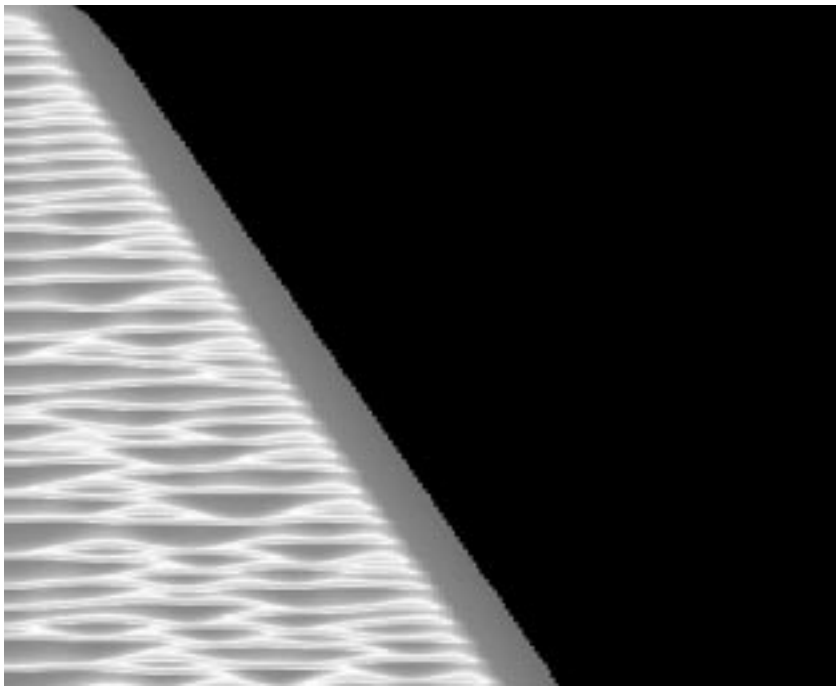

Figure 3.16. Numerical integration of Eqns. 3.36-3.37. Figure is color coded with light and dark indicating high and low values of v. Space increases from left to right and time from top to bottom. Grid size is 200, with domain length of 20. D and μ are the same as for Figure 3.15. The initial conditions are mentioned in the text. The front velocity is approximately 0.055 which is close to the value obtained from the perturbation analysis.

Instability of the homogeneous oscillations suggests that we approximate the front connecting the unsteady oscillations by the front between the unstable steady state and the stable steady state instead. The potential ($V(v, \mu)$) of the unstable steady state is less than that of the low v, stable steady state, indicating that the front switches the domain from the metastable state to the stable one, and implies

that the front velocity is positive. A front solution can be expressed as a stationary solution in the moving frame, $v(\xi),\ w(\xi)$, with $\xi = x - ct$, and $c > 0$. The equations now become:

$$x_1' = x_2, \tag{3.41}$$

$$x_2' = x_3, \tag{3.42}$$

$$Dcx_3' = -G(x_1, \mu) + cF(x_1)x_2 + (D - c^2)x_3, \tag{3.43}$$

where $'$ denotes $\frac{d}{d\xi}$, and $x_1 = v,\ x_2 = v_\xi$, and $x_3 = v_{\xi\xi}$.

Eqns. 3.41-3.43 have 3 equilibrium solutions, $\pi_0 = (v_1, 0, 0)^T, \pi_1 = (v_2, 0, 0)^T$, $\pi_2 = (v_3, 0, 0)^T$, with v_1, v_2, v_3, the three roots (upper, middle and lower respectively) of $G(v, \mu)$. Since we require heteroclinic solutions connecting different equilibrium points, $\pi(\xi) = (x_1(\xi), x_2(\xi), x_3(\xi))$ such that $\lim_{\xi \to -\infty} \pi(\xi) = \pi_0$ and $\lim_{\xi \to \infty} \pi(\xi) = \pi_2$, we linearize about π_0 and π_2. From the expressions for the roots of a cubic polynomial, we see that the linearization matrix of Eqns. 3.41-3.43 about the two solutions have 1 negative and 2 positive eigenvalues, indicating a two dimensional unstable manifold and a 1 dimensional stable manifold. Therefore, 2 parameters specify any trajectory leaving π_0 (c being one of them). Any trajectory that tends to π_2 must be orthogonal to its two dimensional unstable subspace, requiring two parameters for specification. Thus at most a discrete set of fronts connects the two fixed points. In fact, numerical computations show only a single stable front, and the front velocity is unique.

We use a numerical shooting method to compute the velocity of the front as a function of μ, using Gear's method for numerical integration of the equations. Since the unstable subspace of π_0 is 2 dimensional, while the stable subspace of π_2 is 1 dimensional, we reverse the pseudotime ξ and start the trajectory along the stable manifold of π_2. We locate an interval ($c_1 < c < c_2$) such that for $c = c_1$, the

trajectory blows up above π_0 and for $c = c_2$, the trajectory blows up below π_0. By a connectedness argument, a value of c exists in the interval, such that the heteroclinic orbit connects π_0 and π_2, moving to the right with velocity c. By repeatedly bisecting the interval (c_1, c_2) we obtain a value of c correct to 16 significant digits. We show the dependence of c on μ in Figure 3.17. The front speed tends to 0 near the Maxwell point $\mu_M = 0.4$. (the value of μ where the potentials of the two steady states are equal).

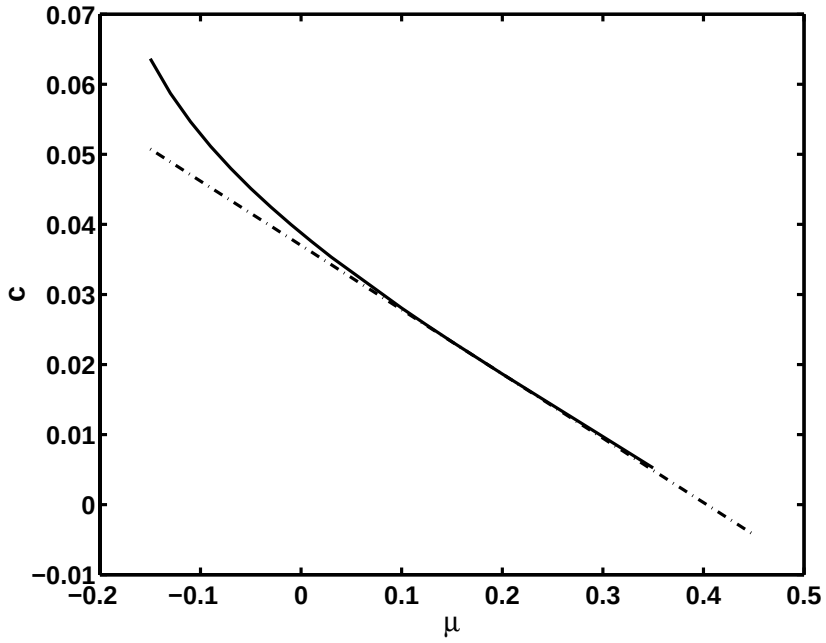

Figure 3.17. Variation of front velocity with the parameter μ. The broken line is calculated from the perturbation analysis and the solid line is the velocity calculated using the shooting method.

We also computed the velocity of the domain wall separating the homogeneous steady state from the unsteady oscillations by a simple perturbation analysis of the stationary front connecting the two steady states. Numerical computations show that the front velocity is rather small, suggesting that we use c as a small parameter,

with the singular limit $c = 0$. Setting $c = 0$ and $\mu = \mu_M$ in Eqns. 3.41-3.43 gives us the stationary front solution (μ_M being the Maxwell condition),

$$x_1(\xi) = a(1 + \exp(-a\xi\sqrt{5}/\sqrt{2})) - b, \tag{3.44}$$

where a and b are constants. For μ close to μ_M, a solvability condition gives the front velocity, following standard perturbation techniques, as $c \sim 0.092(\mu_M - \mu)$. An important point is that the limit cycle makes no non-equilibrium contribution, suggesting that the homoclinic bifurcation and the limit cycle play no role in selecting the front velocity. The average velocity of the front computed from the direct numerical integration of Eqns. 3.41-3.43 agrees with the velocity obtained from the perturbation analysis, indicating that only the difference in potential between the two fixed points determines the front velocity. The front velocity computed using the shooting method is approximate (Figure 3.17), and agrees with the velocity computed using the perturbation for μ greater than the homoclinic point, μ^*, indicating that for the shooting method, the limit cycle changes the front velocity, which is not the case for either the direct computation or the perturbation analysis.

We can now apply the results obtained for the fast subsystem to study a field of diffusively coupled bursters. The Hindmarsh-Rose equations exhibit square wave bursting. The frequency of the oscillations in the active phase decreases logarithmically, as the slow variable increases toward the homoclinic point. Pernarowski [89] has studied a different polynomial model of coupled bursting cells distributed on the unit interval with strong coupling and has shown that for certain initial conditions, the model tends to burst uniformly. However, as we show below, weak coupling results in very different dynamics.

Figure 3.18 shows the bifurcation diagram of the fast subsystem with the nullcline of the slow subsystem superimposed, along with the phase portrait of the bursting oscillations. For the parameter value $z = 4.5$ the single cell model bursts with 9

spikes. The slow subsystem parameter, z, controls the nature of bursting in the full model [90]. The number of spikes per burst increases with decreasing z until homoclinic bifurcations lead to a chaotic bursting state. For small z, the model has a periodic spiking solution and bursting disappears.

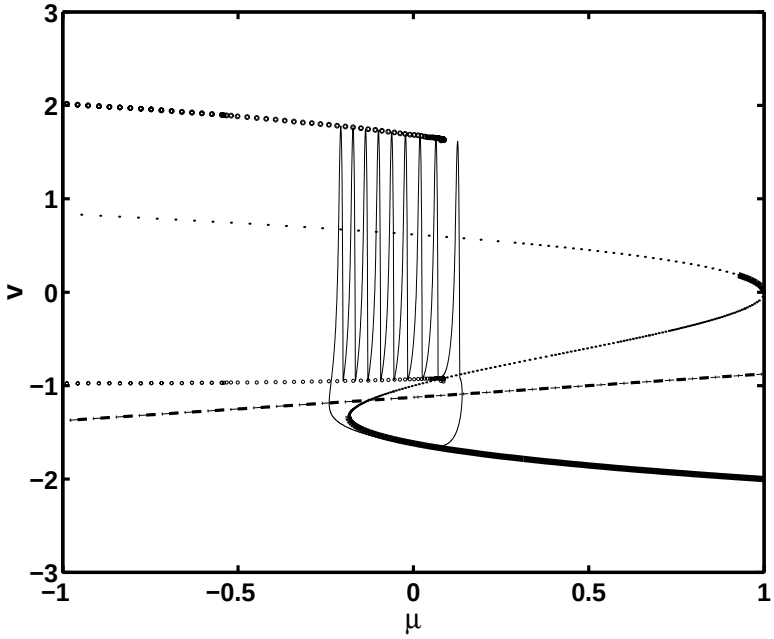

Figure 3.18. Numerical solution of the full Hindmarsh-Rose equations (with D=0) projected onto the fast subsystem bifurcation diagram. The dotted line is the μ nullcline. Heavy lines indicate stable steady states and thin lines indicate unstable steady states. Open circles represent stable periodic orbits. The silent phase tracks the lower branch of steady states and is excited into the active phase near the saddle-node point. The active phase tracks the periodic orbit of the fast subsystem and terminates at the homoclinic orbit.

We show the evolution of the full model in Figure 3.19. The entire domain begins in the active phase with a small patch at the left end advanced in phase along the active phase oscillation. A wave of bursting sweeps across the domain with well defined active and silent phases, but the oscillations in the active phase are now irregular and of small amplitude. The bursting does not terminate at the

same value of μ for all x. The burst period is also larger than that of the single cell model. A well defined wavefront separates the bursting region from the silent region. A second, irregular wavefront switches the domain from the active to silent phase. The front velocity in the leading edge is not uniform because of the slow nonuniform evolution of μ, which changes the potentials of the two competing fixed points continuously.

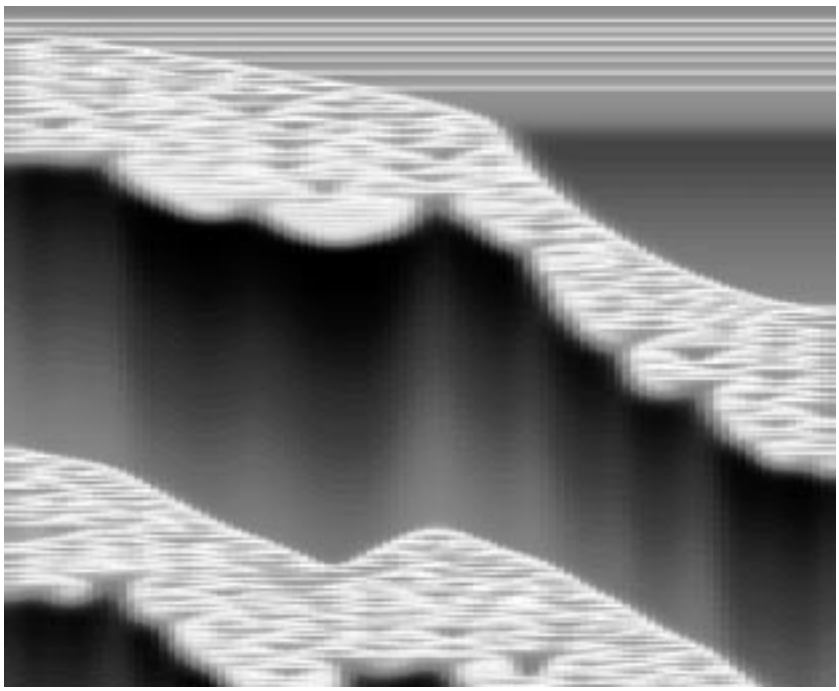

Figure 3.19. Numerical integration of Hindmarsh-Rose equations with D=0.2. v is color coded as in Figs. 3.15-3.16. System length is 20, increasing from left to right and total time is 1000, increasing from top to bottom. A spatial wave of bursting spreads across the domain.

A phase portrait for $x = 10$ shows that the irregular oscillations persist for $\mu > \mu^*$, strongly suggesting that the homoclinic bifurcation no longer plays a role. Instead, the active phase continues till μ increases till μ_M and the upper and middle branches in Fig. 1 disappear in a saddle node bifurcation, leaving the lower fixed

point as the only stationary state. Now, as v switches below the μ nullcline, μ starts to decrease. Since $\mu > \mu_M$, a (locally well defined) front develops with the steady state replacing the oscillations to the right and the active phase terminates as a spatial wavefront extinguishes the oscillations. These observations suggest that diffusively coupled bursters do not have regular active phase oscillations nor do they burst homogeneously. Instead, we see a pulse like solution develop, that travels with nonuniform speed, denoting a small patch of cells that burst. The activity corresponds to a cluster of active cells, and the boundaries of the cluster drift. However, we do not see aberrant chaotic spatiotemporal behavior for the fast subsystem.

The lack of uniform bursting with weak diffusive coupling implies that the measurements of gap junction coupling strengths in isolated β-cell pairs may not hold for the intact islet, where the value of g_{gap} may be considerably larger, for synchronous bursting. Pernarowski has recently studied a model of square wave bursters with diffusive coupling in one dimension [89] with $D = \mathcal{O}(1/\varepsilon)$. For these high values of D, a singular perturbation analysis shows that the domain bursts in synchrony, with the spikes locked in phase. We can anticipate this result from our analysis of a pair of coupled bursters, which synchronize for large coupling strengths.

We have numerically integrated several other model equations with both polynomial as well as more complex kinetics for the fast subsystems. In all cases, we see qualitatively similar behavior as the Hindmarsh-Rose equations, with some differences. In particular, a spatially extended model using Eqns. 3.20-3.22 do not have the irregular large amplitude oscillations about the unstable steady state. The solution behind the transition zone has very small amplitude oscillations about the unsteady state.

Moreover, we see that bistability of a periodic orbit and a steady state, near

a homoclinic orbit is not sufficient to generate spatiotemporal intermittency. The topological structure of the vector fields of the reaction terms is crucial. Since the Hindmarsh-Rose equations are closely related to the normal form for a codimension-3 Takens-Bogdanov bifurcation [91], which is the topological model for the fast subsystems of most types of bursters [62], the fast subsystems of bursters subtly differ from the situation Argentina and Coullet considered. The lack of chaotic dynamics in our model needs to be explained. Qualitatively, the lack of chaotic nucleation of the rest state comes from failure of the Ginzburg-Landau description, because we are considering a finite amplitude limit cycle, which passes close to the stable and unstable manifolds of the saddle point. Thus, the nonuniform phase velocities along the limit cycle result in small amplitude oscillations around the unstable focus. Consequently, the amplitude of oscillations never grows large enough to "break through" to the metastable, rest state. The Benjamin-Feir criterion for amplitude turbulence only considers small amplitude oscillations near the Hopf bifurcation. Additionally, it assumes that the phase gradient (see Chapter 3) does not vary along the limit cycle. We must consider a modified Benjamin-Feir criterion for finite amplitude limit cycles with phase gradients that vary along the limit cycle. A simple application of the B-F criterion to neural oscillators, where the bistable regime is often far from the Hopf bifurcation does not tell the whole story.

CHAPTER 4

NEURAL OSCILLATIONS

4.1 Introduction

Collective oscillations in neural arrays are hallmarks of behavioral patterns. They range from the characteristic rhythmic movements of invertebrate motor responses to the oscillations in different frequency bands of the mammalian EEG. An important example of the latter is the 20-60 Hz rhythm in the neocortex of rats and primates generated by the coordinated activity of large ensembles of excitatory and inhibitory neurons. The study of neural oscillations assumes tremendous importance given their role in generating patterned behavior. Small neuronal networks in invertebrates called Central Pattern Generators directly control movements such as locomotion, respiration and digestion. Large scale oscillations in the neocortex have been implicated in cognitive and behavioral tasks such as short term memory, sleep-wake cycles and dreams, and processing of sensory stimuli [92].

The rhythmic activity of a single neuron is rarely sufficient to drive motor patterns. Neurons that drive rhythmic motor activity almost always connect in networks and interact among themselves in complex fashion to provide a stable oscillatory output. Moreover, in the cortex, processing of large amounts of sensory inputs requires the concerted action of large ensembles of neurons. Thus, synchrony of neural oscillators, in small or large networks organizes behavior, perception and response; and a mathematical understanding of oscillatory dynamics of coupled neu-

rons is vital to understand brain function. However, neuronal dynamics are highly nonlinear, and they interact in a nonlinear, asymmetric fashion. The methods of nonlinear dynamics, with some extensions, play a pivotal role in understanding the generation of coherent neural oscillations.

We can succinctly write a neuronal model as:

$$\frac{d\mathbf{x}}{dt} = F(\mathbf{x}, \{\mu\}), \tag{4.1}$$

where $\mathbf{x} \in \mathbb{R}^m$ is a vector of state variables for a neuron. $F(.)$ is a continuous function from $\mathbb{R}^m \rightarrow \mathbb{R}^m$, and $\{\mu\}$ is a vector of parameters controlling the state of the neuron, such as sensory inputs or external, experimental manipulations. A neural oscillator has a solution of the form $\mathbf{x}_0(t+\mathrm{T}) = \mathbf{x}_0(t),\ \forall\ t$, for some minimum positive integer T, the period of oscillations. The oscillations are asymptotically orbitally stable if for each $\epsilon > 0$, there is a $\delta > 0$ such that if $|\mathbf{x}(0) - \mathbf{x}_0(0)| < \delta$, then $|\mathbf{x}(t) - \mathbf{x}_0(t)|\ \ \forall t > 0$. Furthermore, a phase ϕ exists, such that,

$$\lim_{t\rightarrow\infty} |\mathbf{x}(t) - \mathbf{x}_0(t+\phi)| \rightarrow 0, \tag{4.2}$$

where ϕ is the asymptotic phase shift. Eqn. 4.2 essentially implies that nearby initial conditions in phase space asymptotically tend to the periodic orbit, with at most a phase shift. Interactions with other neurons modify the equations to:

$$\frac{d\mathbf{x}_i}{dt} = F_i(\mathbf{x}_i, \{\mu\}) + G_i(\mathbf{x}_i, \mathbf{x}_j, \rho), \quad i, j = 1, \cdots n, \tag{4.3}$$

where the $G(\mathbf{x}_j)$ are smooth functions that describe the interaction.

CPGs generate rhythms autonomously, without any feedback from the sensory inputs. The patterns of their oscillations are nevertheless under the control of the sensory environment, so that when the environmental conditions change, the patterns of oscillations change concomitantly. The inputs to the network are not oscillatory in general, but the output of the network is oscillatory, *i.e.* the network has no "zietgeber". Neither oscillating, single neurons nor networks require a pacemaker.

We give a general introduction to synaptic function in Section 4.2, and outline perturbative techniques for obtaining approximate, simple forms from complicated evolution equations for single oscillators and networks with synaptic coupling in Section 4.3. We discuss a model network with experimentally observed multiple synaptic time scales using methods from Section 3.3 and geometric singular perturbation theory (Section 4.4)

4.2 Coupling in Neural Networks

Besides electrical, diffusive coupling via gap junctions, interactions between neurons commonly occur at specialized sites on their membranes called synaptic terminals. At each terminal, one neuron is the emitter and one a receiver. Emitter sites release chemicals called neurotransmitters, packaged in small, membrane spheres called vesicles which diffuse onto specialized protein molecules called receptors in the receiver neuron. The release sites are located at the presynaptic terminals, the receptor sites are situated in the post-synaptic membrane. The release of vesicles requires a change in the membrane potential at the presynaptic terminals. When an action potential occurs in the presynaptic cell, the voltage change at the presynaptic terminal initiates a complex sequence of biochemical reactions, which ultimately result in a pulsatile release of vesicles. These vesicles diffuse across the intercellular space between the pre- and post-synaptic terminals and bind to the receptors. The binding of neurotransmitter to the post-synaptic receptors in turn opens specific ion channels in the post-synaptic cell near the synapse, causing the membrane potential of the cell to change due to the ion flux.

Synapses differ in the kinds of neurotransmitter released at the presynaptic terminals as well as the receptors at the post-synaptic site. If the neurotransmitter binding depolarizes the membrane (the membrane potential increases with respect to

the resting membrane potential), the neurotransmitter action is called excitatory, because sufficiently large amounts of neurotransmitters released across synapses would ultimately cause the cell to fire an action potential. If the binding hyperpolarizes (the membrane potential decreases with respect to rest), the neurotransmitter action is inhibitory. Shepherd [58] gives a detailed, pedagogical account of the physiology and biochemistry of synapses. Tuckwell discusses the mathematics of synaptic transmission [93].

Rall proposed a simple model for the synaptic potential to fit the experimentally observed time courses of post-synaptic potential changes. He suggested that if the presynaptic membrane potential crosses the threshold for action potential generation, the post-synaptic potential at the synapse can be approximated as:

$$v_{syn}(t) = \alpha t e^{-\alpha t}, \tag{4.4}$$

where α is a rate constant, derived from fitting Eqn. 4.4 to the experimentally measured post-synaptic potentials. This approximation, called the α-function captures the qualitative features of synaptic action, but misses important details [94], such as the saturation of response to a high frequency stimulation. An alternative model exploits the similarity between the ionic currents generated by voltage gated channels and the neurotransmitter gated synapses, and considers the ion current, I_{syn}, due to the synaptic action to be:

$$I_{syn} = -g_{syn} s (V - V_{syn}), \tag{4.5}$$

where g_{syn} is the maximal conductance of the channels, s is related to the channel opening probability and V_{syn} is the reversal potential for the channel (*i.e.* the Nernst equilibrium potential). A simple first order kinetic model:

$$S_{bound} \underset{r_{ji}}{\overset{r_{ij}(V)}{\rightleftharpoons}} S_{unbound}, \tag{4.6}$$

suffices to model the dynamics of the neurotransmitter receptor binding reaction. The forward rate function $r_{ij}(V)$ depends on the presynaptic potential, representing the voltage gated release of neurotransmitter. The reversible binding reaction can be modeled as:

$$\frac{ds}{dt} = k_f s_\infty(V_{pre})(1 - s) - k_r s, \tag{4.7}$$

where k_f and k_r are the binding and dissociation rate constants for the neurotransmitter receptor pair and $s_\infty(V_{pre})$ is a sigmoidal function that models the transmitter release due to the presynaptic action potential. Eqn. 4.7 also captures the saturation of the synapse from prolonged stimulation, due to receptor saturation or emitter depletion, which is important for bursting cells.

The most common example of an excitatory synapse is the glutamate-AMPA (α-Amino-3-hydroxy-5-Methyl 4-isoxazole Propionic Acid) neurotransmitter receptor pair, prevalent throughout the central nervous systems of vertebrates. These fast excitatory synapses have small rise and fall time constants (rise times of $\sim$1 ms and decay times of 5 ms). Another important excitatory synapse is the glutamate-NMDA (N-Methyl-D-Aspartate) pair, which has slow rise and fall times. NMDA channels are unique among excitatory synapses in that their activation requires the post-synaptic membrane also to be depolarized (the presynaptic membrane is necessarily depolarized for vesicle release). The NMDA synapse has rise times of 5-10 ms and decay times of $\sim$150 ms.

Inhibition in the central nervous system of vertebrates is mediated predominantly by the neurotransmitter GABA (γ-Amino-Butyric Acid) with its associated receptor pairs $GABA_A$ and $GABA_B$. The former, like the AMPA receptor, is fast, with small rise and fall time constants. $GABA_B$ receptors do not directly produce a change in the membrane potential, but set off a complex series of reactions which eventually triggers ion channels to open to hyperpolarize the membrane. As several

intermediate steps are involved in $GABA_B$ action, the effective time constants for the rise and fall of post-synaptic potentials are large. These synapses are examples of slow inhibition.

We stress that the transmitter-receptor pair and not the neurotransmitter alone is excitatory or inhibitory. Thus, in some invertebrate neurons, glutamate, in conjuction with an appropriate receptor (not AMPA or NMDA) is actually inhibitory [95]. Finally, the overall effect of the synapses depends on the collective effect of several different voltage and chemical gated ion channels in the membrane.

4.3 Neural Oscillations

From a mathematical viewpoint, neural oscillations generically arise in two ways, distinguished by their parameter dependence close to the onset of oscillations. Type I oscillations arise at a saddle-node-on-invariant-circle (Section 2.2.5), while Type II oscillations arise at a Hopf bifurcation (sub- or super-critical). their frequency-current relationship distinguishes them. For Type I oscillations, the frequency of oscillations is zero at onset and increases as $\sqrt{I_{app}}$, whereas the frequency of oscillations of Type II rises discontinuously at onset, and remains approximately constant for increasing I_{app}. The canonical Hodgkin-Huxley model is an example of Type I oscillations while the action potentials of cortical neurons are of Type II.

The distinction between the two generic mechanisms is not restricted to the onset of oscillations, but crucially affects the nature of synchrony in neural networks.

4.3.1 Weakly Coupled Oscillators: Theory

In this section, we outline formal methods for analysis of general models of the form:

$$\frac{d\mathbf{x}_i}{dt} = F_i(\mathbf{x}_i, \mu) + \varepsilon G_i(\mathbf{x}_i, \mathbf{x}_j, \rho),\ i, j = 1, \cdots n, \tag{4.8}$$

with $\varepsilon \ll 1$.

Our basic assumption is that the uncoupled oscillator:

$$\frac{d\mathbf{x_i}}{dt} = F_i(\mathbf{x}_i, \mu),\ \mathbf{x}_i \in \mathbb{R}^m \tag{4.9}$$

has an asymptotically stable periodic solution $\{\Gamma \in \mathbb{R}^m \mid \mathbf{x}_i(t) = \mathbf{x}_i(t+T)\}$, with period T, for some value of μ. The n uncoupled oscillators have a periodic solution on an n torus given by the direct product of the n periodic orbits, $\mathcal{T} = \Gamma_1 \times \Gamma_2 \times ... \times \Gamma_n$. A smooth change of coordinates exists such that $\mathbf{x}_i \in \Gamma_i$ maps onto the unit circle S^1, parametrized by the phase of the limit cycle θ_i. We have omitted an implicit coordinate change that takes $\mathbf{x}_i \in \mathbb{R}^m$ to $x_i \in \Gamma_i$, which we can obtain using a center-manifold reduction [9].

Consider $x_i(t)$ be the periodic solution to the Eqn. 4.9 such that $x_i(0) \equiv x_i^0 \in \Gamma_i$. Let $\theta_i(t)$ be a phase variable such that the parametrization:

$$M_i : S^1 \to \Gamma_i, \quad M_i(\theta_i(t)) = x_i(t) \in \Gamma_i, \quad t \in [0, 2\pi\Omega_i], \quad i = 1, \cdots, m, \tag{4.10}$$

maps the limit cycle Γ_i onto the unit circle. Ω_i is the frequency of the limit cycle.

Since $x_i(t) = M_i(\theta_i(t))$ is a periodic solution to Eqn. 4.9, we have:

$$\dot{x_i} = \frac{dM_i(\theta_i(t))}{dt} = M_i'(\theta_i(t))\dot{\theta_i} = M_i'(\theta_i(t))\Omega_i = F_i(M_i(\theta_i(t), \mu)) \tag{4.11}$$

for all t. Therefore,

$$M_i'(\theta_i(t)) = F_i(M_i(\theta_i(t), \mu))/\Omega_i \tag{4.12}$$

for all $\theta_i \in S^1$. Substituting $x_i(t) = M_i(\theta_i(t))$ in Eqn. 4.8, we obtain:

$$M_i'(\theta_i(t))\dot{\theta_i} = F_i(M_i(\theta_i(t)), \mu) + \varepsilon G_i(M_i(\theta_i(t)), \mu, \rho). \tag{4.13}$$

Multiplying both sides by

$$\alpha_i(\theta_i) = \frac{\Omega_i F_i^{-1}(M_i(\theta_i), \mu)}{|F_i(M_i(\theta_i), \mu)|^2} \tag{4.14}$$

we obtain

$$\dot{\theta_i} = \Omega_i + \varepsilon\alpha_i(\theta_i)G_i(M_i(\theta_i), \mu, \rho). \tag{4.15}$$

Identifying $\alpha_i(\theta_i)G_i(M_i(\theta_i), \mu, \rho) = g(\theta_1, \cdots, \theta_n, \mu, \rho)$, we have the phase equation:

$$\dot{\theta_i} = \Omega_i + \varepsilon g(\theta_1, \cdots, \theta_n, \mu, \rho). \tag{4.16}$$

The coordinate change assigns a phase $\theta(t)$ to each $x(t)$. If $x(t)$ rotates around Γ (not necessarily at a constant speed), $\theta(t)$ rotates in $[0, 2\pi]$ with speed $\Omega_i(\mu) = 2\pi/\mathrm{T_i}$. Let us now consider a pair of coupled oscillators:

$$\frac{d\theta_1}{dt} = \Omega_1(\mu) + \varepsilon g_1(\theta_1, \theta_2, \varepsilon), \tag{4.17}$$

$$\frac{d\theta_1}{dt} = \Omega_2(\mu) + \varepsilon g_2(\theta_1, \theta_2, \varepsilon). \tag{4.18}$$

The oscillators are frequency locked if they have a stable periodic solution. If the frequencies Ω_1 and Ω_2 are in a 1:1 ratio, the network is entrained. We shall only consider cases of 1:1 frequency locking in the following. Frequency locking with $p : q$, with p and q relatively prime nonnegative integers result in complicated resonance structures [96]. We further define $p : q$ phase locking for entrained oscillators as:

$$q\theta_1(t) - p\theta_2(t) = \text{constant}. \tag{4.19}$$

If $p = q = 1$, the oscillators are synchronized. Thus, our definition of synchrony implies mutual entrainment and 1:1 phase locking. The phase difference between the two oscillators is $\theta_1(t) - \theta_2(t) = \phi(t)$. As in Section 2.3, the $\phi(t) = 0$ solution is locked in phase, and the $\phi(t) = \pi$ solution is locked anti-phase. The above definitions can be extended similarly for n coupled oscillators [74].

We have left out some technical steps such as using the invariant manifold theorem to extend the center-manifold reduction of Eqn. 4.9 to the case of weak coupling.

Although we have formally shown the existence of a coordinate change that takes Eqn. 4.8 to Eqn. 4.16, we now show how to explicitly construct the coordinate transformation. We closely follow the steps in [97].

Consider a weakly connected oscillator network of the form of Eqn. 4.8 such that each oscillator has an exponentially orbitally-stable, periodic solution, Γ_i, for $\varepsilon = 0$. Let $\tau = \varepsilon t$ be a slow time and let $\phi(\tau)$ be a measure of the phase deviation from the periodic orbit and,

$$x_i(t) = \Gamma_i(t + \phi_i(\tau)) + \varepsilon P_i(t + \phi_i(\tau), \varepsilon). \tag{4.20}$$

where the εP_i are the small perturbations to the product limit cycle T. $\phi_i(\tau)$ varies slowly in time and accounts for the phase deviations due to the weak coupling. Note that we keep the two time scales, t and τ separate.

We differentiate the above equation with respect to t and Taylor expand to obtain

$$\begin{aligned} \dot{x}_i &= \Gamma_i'(t + \phi_i)(1 + \varepsilon \frac{d\phi_i}{d\tau}) + \varepsilon \frac{dP_i(t + \phi_i, \varepsilon)}{dt} + O(\varepsilon^2) \\ &= F_i(\Gamma_i(t + \phi_i)) + \varepsilon G_i(\{\Gamma(t + \phi)\}) + \varepsilon DF_i(\Gamma_i(t + \phi_i))P_i(t + \phi, \varepsilon) + O(\varepsilon^2), \end{aligned}$$

where DF_i is the Jacobian of the vector field F_i. As in regular perturbation theory, we equate terms with like powers of ε, with $\Gamma'(t + \phi_i) = F_i(\Gamma_i(t + \phi_i))$. We have:

$$F_i(\Gamma_i(t + \phi_i))\frac{d\phi_i}{dt} + \frac{dP_i(t + \phi_i, 0)}{dt} = G_i(\Gamma(t + \phi)) + DF_i(\Gamma_i(t + \phi_i))P_i(t + \phi, 0). \tag{4.21}$$

Eqn. 4.21 is a linear equation of the form:

$$\frac{dy_i}{dt} = A_i(t, \phi_i)y_i(t, \phi_i) + b_i(t, \{\phi\}), \tag{4.22}$$

where we treat $\phi \in T$ as a parameter, $A_i(t, \phi_i) = DF_i(\Gamma_i(t+\phi_i))$ is a linear operator, and $b_i(t, \{\phi\}) = G_i(\{\Gamma(t + \{\phi\})\}) - F_i(\Gamma_i(t + \phi_i))\frac{d\phi_i}{dt}$. From the theory of linear

equations, we can show that Eqn. 4.22 has a solution if and only if the solvability condition:

$$< Z, b >= \frac{1}{2\pi} \int_0^{2\pi} Z_i(t, \phi_i) b_i(t, \{\phi\}) dt = 0, \tag{4.23}$$

is satisfied. $Z_i(t, \phi_i) = q_i^*(t, \phi_i)$, where $q_i(t, \phi_i)$ is the solution to the adjoint equation:

$$\frac{dq_i(t, \phi_i)}{dt} = -A_i(t, \phi_i)^\dagger q_i(t, \phi_i), \tag{4.24}$$

with the normalization :

$$\frac{1}{2\pi} \int_0^{2\pi} Z_i(t, \phi_i) F_i(\Gamma_i(t, \phi_i)) dt = 1. \tag{4.25}$$

Substituting the expression for $b_i(t, \{\phi\})$ in Eqn. 4.23, we have:

$$\begin{aligned} \frac{d\phi_i}{dt} &= \frac{1}{2\pi} \int_0^{2\pi} Z_i(t + \phi_i, 0) G_i(\{\Gamma(t + \{\phi\})) dt \\ &= \frac{1}{2\pi} \int_0^{2\pi} Z_i(s, 0) G_i(\{\Gamma(s + \{\phi\} - \phi_i)) ds, \quad s = t + \phi_i. \end{aligned}$$

The function $Z_i(t + \phi_i)$ is called the phase response function, which measures the asymptotic deviation in phase of the limit cycle for a small, impulsive perturbation. The phase equation shows that any delays in the couplings enter into the coupling terms as phase shifts.

An implicit assumption for the derivation of the phase equations in the previous section is that the neuronal coupling is "weak". How small is ε for most models? Typical post-synaptic potentials are on the order of 0.5 mV in pyramidal cells in the hippocampus, whereas the threshold voltage required for firing is about 25 mv above resting. Given the nonlinear summation of the post-synaptic potentials from different neurons, about 400 simultaneous EPSPs are required to discharge a pyramidal neuron. Thus, we can estimate $\varepsilon \sim 0.0025$. This is just a crude, order of magnitude estimate. Hoppensteadt and Izhikevich [98] give a more detailed discussion of the weakness of synaptic strengths and the validity of the assumption for neural oscillators.

4.3.2 Weakly Coupled Neural Networks

We can now look at the phase locking properties of oscillatory neural networks connected by synapses. We assume that the neurons oscillate periodically in response to an externally applied constant stimulus. How do synaptic interactions between the neurons modify the oscillations? We have already seen in Chapter 2 that weak gap junctional coupling in identical oscillators can lead to anti-phase oscillations. The solvability condition and the adjoint equation allows us to numerically construct the function $g_i(\theta_i, \{\mu\}, \rho)$ for an arbitrary choice of $F(\{\mathbf{x}_i\}, \{\mu\})$ [99]. We study the dynamics of a network of 2 identical weakly coupled Hodgkin-Huxley model neurons using numerically constructed phase equations. The HH equations (Eqns. 3.3-3.6) now have an additional term representing the synaptic current $I_{syn} = -g_{syn} s(V - V_{syn})$, where the terms are defined in Section 3.2. The voltage equation now becomes:

$$\begin{aligned} C_m \frac{dV_i}{dt} &= -g_{Na} m_i^3 h_i (V_i - V_{Na}) - g_K n_i^4 (V_i - V_K) \\ &\quad - g_{leak}(V_i - V_{leak}) + I_{app} - g_{syn} s_j (V_i - V_{syn}),\ i, j = 1, 2,\ i \neq j. \end{aligned}$$

The equations for the recovery variables m_i, n_i, h_i are as before. Hansel *et al.* first studied this model network [100] using a simple α-function form (Eqn. 4.4) for the dynamics of s_j. We use a kinetic description of the synaptic current given by:

$$\frac{ds_i}{dt} = k_f s_\infty(V)(1 - s_i) - k_r s_i. \tag{4.26}$$

with $s_\infty = 1/(1+\exp(-(V-V_a)/V_b))$, with V_a =0, and V_b =2, and the rate constants k_f =1.1 and k_r =0.11 to model the dynamics of the synaptic conductance. These values are representative of the excitatory AMPA synapse [94]. A natural advantage of this formalism is that we can independently control the rise and fall times. van Wreeswijk and Abbott [101] have shown that the value of the fall time significanly

alters the phase dynamics of networks of integrate-and-fire neurons (a caricature of the HH equations). We numerically solve the adjoint equation (Eqn. 4.23) and show the solution $\mathbf{Z}(\theta_i)$ in Fig. 4.1. The solution to the adjoint equation is the phase response function for the HH model. A pulse-like perturbation retards the phase along the limit cycle for negative values of $\mathbf{Z}$ and advances the phase for positive values of $\mathbf{Z}$.

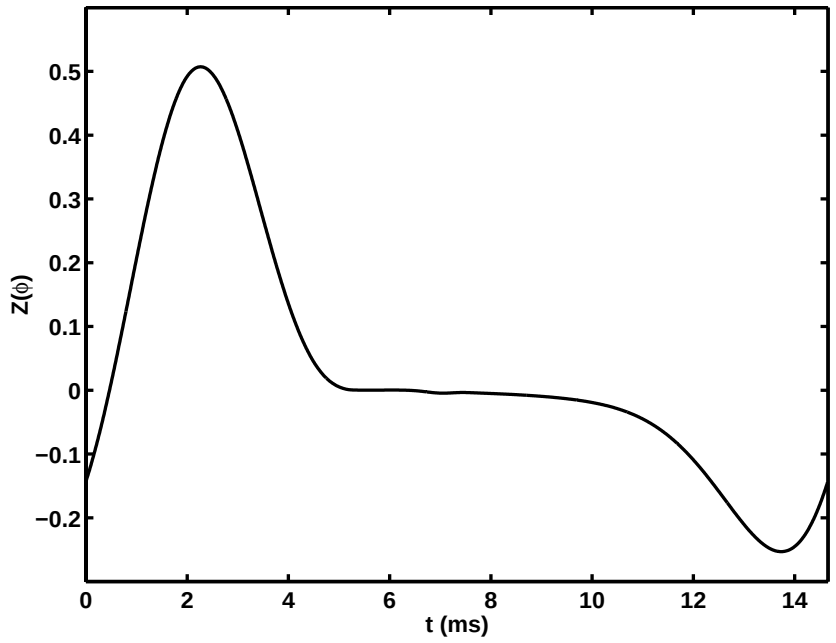

Figure 4.1. Solution of of the adjoint equation (the phase response curve) for I_{app} =10μA/cm^2. The phase response is negative over a large part of the period.

We compute the phase function $H(\theta_1 - \theta_2)$ by computing the integral in Eqn. 4.26 numerically over the period with $G(\theta_1, \theta_2, \mu, \rho) \equiv -g_{syn} s_j (V - V_{syn})$, and show the results in Figure 4.2.

The antisymmetric part of the interaction function has fixed points at 0 and $\pm\pi$ for small values of applied current. The negative slope at 0 phase difference indicates that the in-phase solution is stable while the antiphase solutions are unstable. For

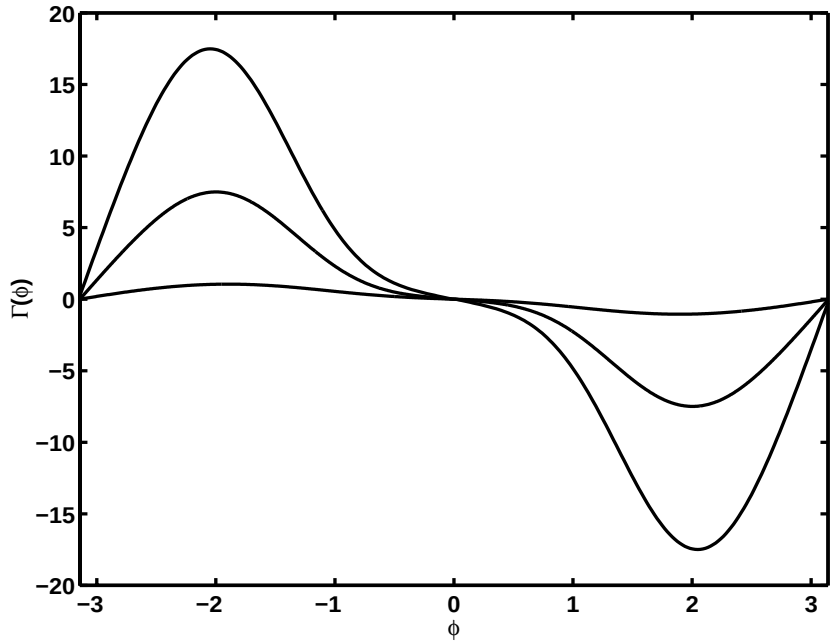

Figure 4.2. The antisymmetric part of the phase interaction function $H^-(\theta_1 - \theta_2)$ for $I_{app} = 10$, 20 and 50 μA/cm^2 (the amplitude of H^- decreases with I_{app}).

larger values of the applied current, the stable fixed point undergoes a pitchfork bifurcation, with two stable, symmetric solutions at non-zero phase difference. A trace of the membrane potential (Figure 4.3) for I_{app} =50 μA/cm^2 shows that the oscillators spike with a small phase difference.

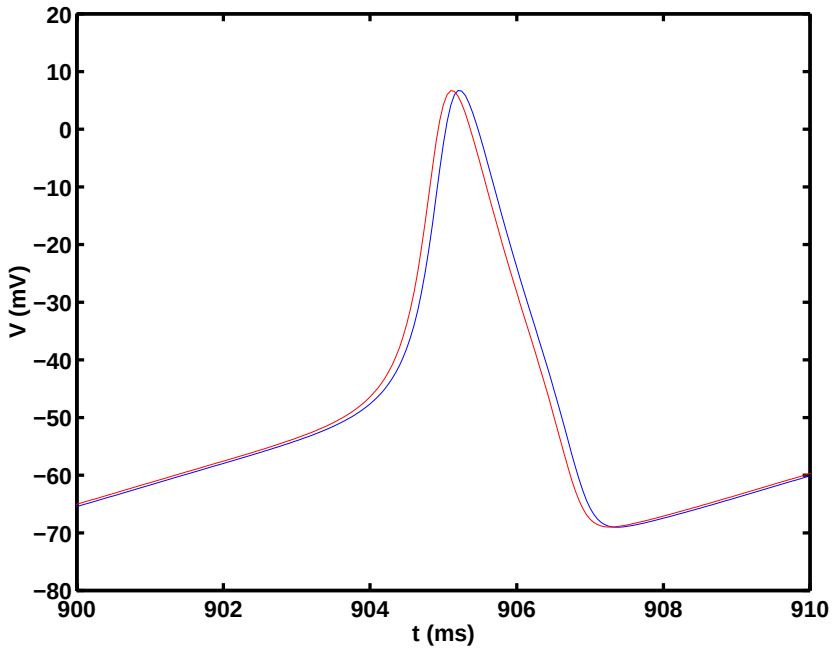

Figure 4.3. Time integration of HH equations with I_{app} =50 μA/cm^2 and g_{syn} =0.2. The two neurons are started antiphase and converge to a slightly out of phase trajectory after a transient (not shown).

The phase approximation breaks down for larger values of g_{syn} as amplitude efffects become important. The derivation of the phase difference approximation for coupled oscillators implicitly assumes that the deviation from the amplitude of the limit cycle $\dot{\rho}(\tau, t) \sim \mathcal{O}(\varepsilon)$. As g_{syn} becomes large, the amplitude deviation from the limit cycle is no longer small and must be considered.

The pitchfork bifurcation to two stable, out of phase states occurs for lower values of the applied current for slower synapses with smaller values of k_r. We

also show the phase interaction function for a network with mutual, fast inhibition (Figure 4.4). In contrast to mutual excitation, this network has stable in-phase and anti-phase solutions for small values of applied current. The in-phase state becomes unstable via an inverse pitchfork bifurcation as I_{app} increases.

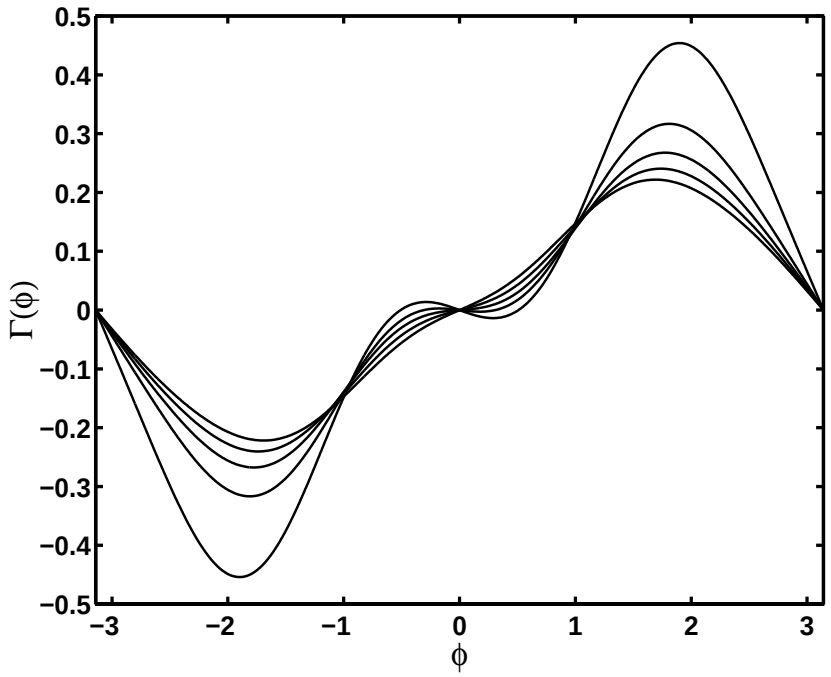

Figure 4.4. The antisymmetric part of the phase interaction function $H^-(\theta_1 - \theta_2)$ for fast inhibition with $I_{app} = 10$, 20, 30, 40, and 50 μA/cm^2 (the amplitude of H^- decreases with I_{app}).

The phase reduction of Section 3.3.2 works well for synaptic decay constants not much larger than the period of oscillations. However, if the decay constant is much larger than the time period (slow synapses), the oscillations can be averaged over and the dynamics of the slow synapses suffice to describe the rates of action potentials [102, 99].

4.4 Slowly Coupled Inhibitory Neurons

4.4.1 Background and Motivation

Central Pattern Generators (CPG) control rhythmic activities such as swimming, heartbeat, breathing or walking. CPGs are networks often composed of a small number of neurons whose output is oscillatory. Individual neurons in CPGs may themselves be oscillatory and the the synaptic interactions between the neurons patterns the network rhythm. Conversely, neurons in some CPGs are not endogenous oscillators and synaptic interactions are crucial in initiating and maintaining the network rhythm. Getting [103] and Harris-Warrick *et al.* [6] review the intrinsic and synaptic properties of several invertebrate CPG networks. Some well studied networks include the escape swim CPG in *Tritonia*, the gastric mill CPG in the lobster, the flight CPG in locust and the CPG controlling the heartbeat of the leech *Hirudo medicinalis*.

Several features of synapses contribute to temporal pattern generation in CPGs, such as the polarity (excitatory or inhibitory), ionic dependence and temporal characteristics (for example, the time course of multiphasic actions, where the synapse has both excitatory and inhibitory components). Circuit models with complex synaptic properties often show dramatic changes in network oscillations as the synaptic time course varies. Wang and Rinzel [104] showed that pairs of neurons with reciprocal inhibition can oscillate in-phase or anti-phase, depending on the decay time constant of the synaptic inhibition (the value of k_r in Eqn. 4.7 is small). Detailed models of CPGs [60, 105] with complex synaptic interactions are useful in understanding particular cases, but do not elucidate general principles, in as much as any general principles exist in neurobiology.

Most general models of small neuronal networks [106, 104, 100] consider synaptic interactions on only a single time scale. However, several examples of synaptic

interactions have multiple time scales. Pyramidal cells in the mammalian cortex can excite other cells with both fast and slow excitatory synapses, and some evidence suggests that the same inhibitory cell can provide fast and slow inhibition in the same target [107]. Invertebrate CPG circuits often have more complex synapses which have a fast excitatory and slow inhibitory component or *vice versa* [60], as well as mixed synapses of the same kind, which are crucial in determining the overall rhythm of the network [108]. What are the properties of networks of neural oscillators with mixed time scale coupling?

4.4.2 Model Dynamics

We study two oscillators coupled by both slow and fast inhibition, and show that the presence of multiple time scales in the coupling leads to varied behavior. We represent each oscillator by the following set of differential equations:

$$\begin{aligned}\frac{dv}{dt} &= -I_{ion}(v_i, n_i) - g_{ji}s_j(v_i - V_{syn}) \\ &\quad - g'_{ji}q_j(v_i - V'_{syn}) + I_{app},\end{aligned} \tag{4.27}$$

$$\frac{dn}{dt} = \frac{n_\infty(v) - n}{\tau(v)}, \tag{4.28}$$

$$\frac{ds}{dt} = \frac{s_\infty(v) - s}{\tau_s}, \tag{4.29}$$

$$\frac{dq}{dt} = \frac{q_\infty(v) - q}{\tau_q}, \tag{4.30}$$

where $I_{ion} = g_{Na}m^3_\infty(v)(v - v_{Na}) + g_K n^4(v - v_K) + g_L(v - v_L)$, represents the voltage activated currents (sodium and potassium) and the leakage current. n is the gating variable for the potassium current activation s_j, is the probability of channel opening and g_{ji} specifies the maximal conductance for the fast synapse. q_j does the same for the slow synapse. V_{syn}, V'_{syn} are the reversal potentials for the synaptic current. We assume that the sodium activation is instantaneous and achieves steady state

immediately. These equations are a reduced version of the familiar Hodgkin-Huxley equations [61]. The functions $n_\infty(v),\ s_\infty(v),\ \tau(v)$, and q_∞ are the usual sigmoidal activation functions for the HH model. We give the functional forms in Appendix A. The time scale τ_s is equivalent to the fast timescale of the spike mediated $GABA_A$ inhibitory synapse, while τ_q is the long timescale associated with the slow rise and fall of the slow inhibition. We take the slow inhibition to be one single aggregate process as the exact mechanisms of the slow synapse are not known [108].

Rinzel and Frankel [109] studied the model (Eqns. 4.27-4.30) with slow inhibition only. Note that for $1/\tau_q \ll 1$, the oscillators become a singularly perturbed dynamical system. Upon taking the singular limit $\tau_q \to \infty$, we can treat q_j as a parameter. The fast variables $\{v_i, n_i\}$ have a stable rest state for large values of q_j. This rest state destabilizes via a subcritical Hopf bifurcation at $q_j \sim 0.106$. Since the period of the membrane oscillations is much smaller than the time scale of the variation of q_j, the averaging theorem [9] simplifies the dynamics of the coupled neurons [109, 102, 99]. Averaging over the fast variables, only the synaptic activation variables remain. This procedure drastically reduces the number of dimensions of the problem. The averaged equations for the slow subsystems are:

$$\dot{\bar{s}}_i = \bar{s}_\infty(\bar{s}_j) - \bar{s}_i,\ i \neq j. \tag{4.31}$$

The subcritical Hopf bifurcation of the rest state of each neuron implies that the neurons are bistable for a small range of q_j. For multiple oscillatory branches, we must average the slow variables over each oscillatory solution. Note that the steady states of Eqn. 4.31 are analogous to an input-output transfer function, denoting the response of $q_j(\{q_i\})$. We show the steady states of $q_1(q_2)$ in Figure 4.5.

Rinzel and Frankel used a clever graphical construction to study the stable steady states of Eqn. 4.31. Figure 4.5 represents the steady states for a network with a unidirectional connection, cell 2 inhibiting cell 1. By plotting the steady states of

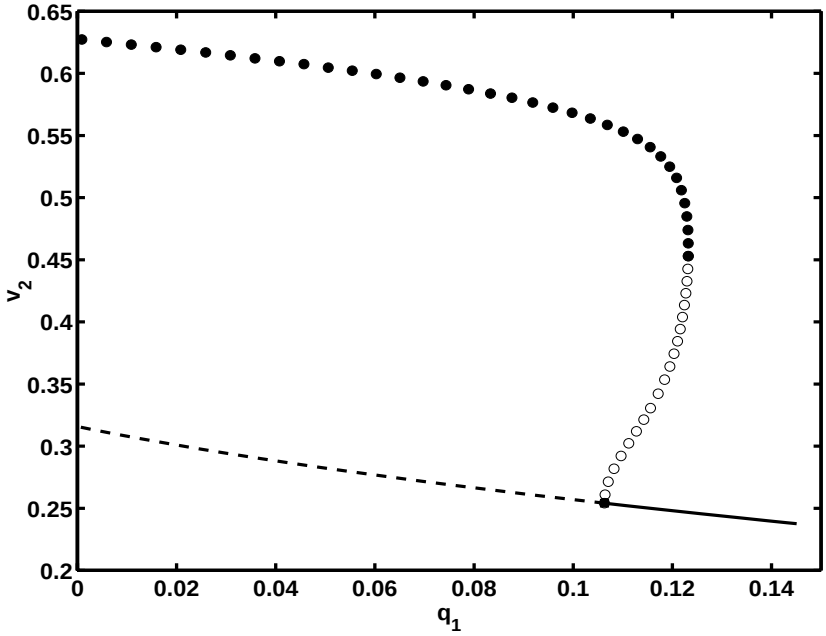

Figure 4.5. Bifurcation diagram for the modified Hodgkin-Huxley equations driven by an unidirectional, slow inhibitory synapse. q_1 is the activation variable of the slow synapse from cell 1 onto cell 2. Solid lines indicate stable rest states, dashed lines indicate unstable rest states, open (filled) circles denote maximum amplitudes of unstable (stable) oscillations. The square at $q_1 = 0.106$ is the point of a subcritical Hopf bifurcation.

$q_1(q_2)$ and $q_2(q_1)$ on the same graph, we can obtain the steady states of the network with reciprocal inhibition. The intersections of the two steady state curves are the steady states of the network. We see 4 intersections of the steady state curves (Figure 4.6: cell 1 at rest and cell 2 active, its symmetric counterpart, with cell 2 at rest and cell 1 active, both cells active and both at rest. The latter two states being intersections of unstable branches are unstable. Therefore, the network is bistable, with either cell 1 or cell 2 active and the other at rest. A strong current pulse to the active cell can switch the network between the two states.

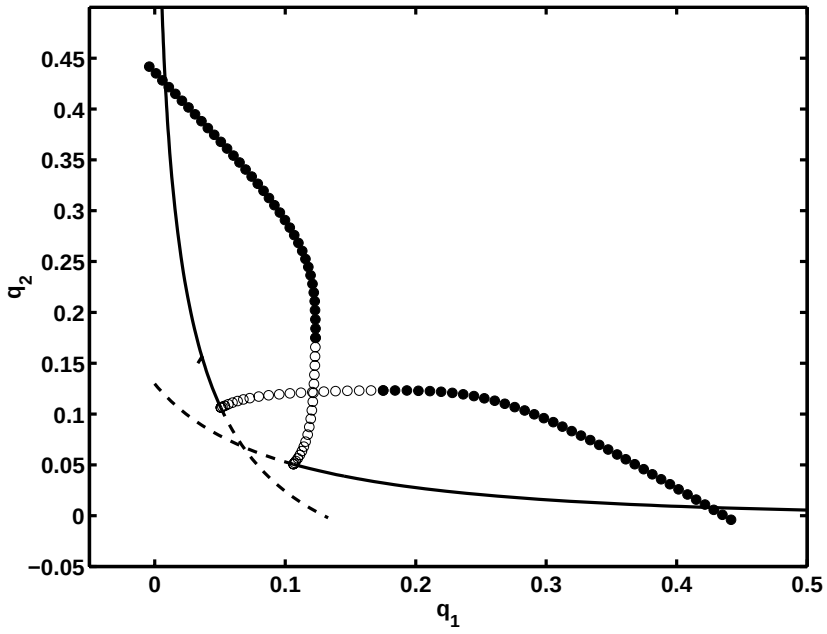

Figure 4.6. Steady states of the averaged equations for the slow variables. Solid lines indicate stable rest states. Dashed lines indicate unstable rest states. Open (filled) circles denote maximum amplitudes of unstable (stable) oscillations. The intersections of the curves are the steady states for the equations.

Now consider a mixed synapse with fast and slow components. The fast component has a time scale comparable to the time scale of the oscillations and cannot be

eliminated by averaging. We show the time course of the two cells for $g_{12} = g_{21} = 0.3$ in Figure 4.7, with all the other parameters fixed. If the slow synaptic variables q_i are initially close, the network bursts in synchrony. The spikes within the burst are anti-phase and the amplitudes are slightly unequal. The initial conditions set both cells at rest. We apply a constant current I_{app} to both cells to model an external stimulus. We also apply an additional small, brief current pulse to one cell as a small perturbation to break the symmetry.

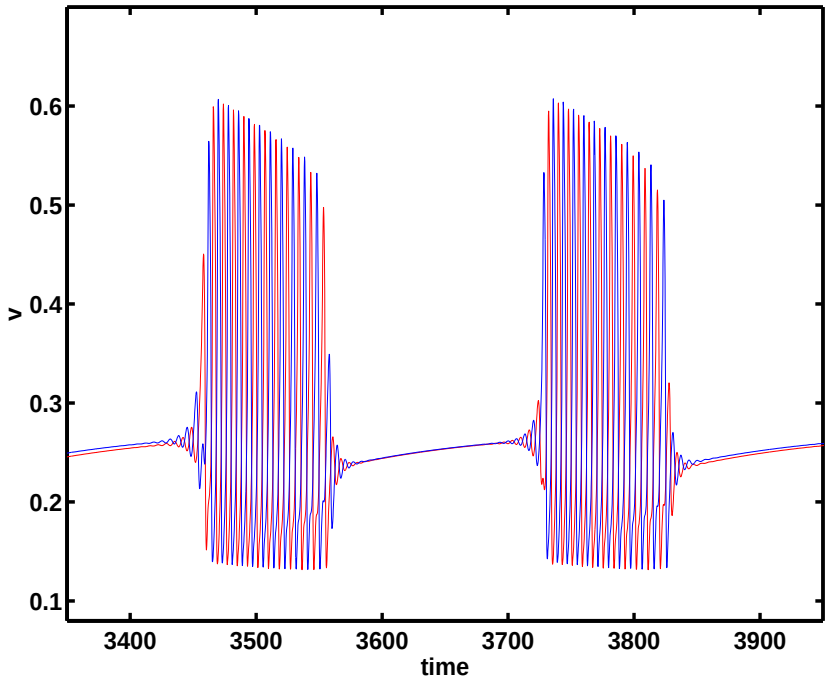

Figure 4.7. Numerically integrated trajectories for Eqns. 4.27-4.30 shows a synchronous bursting solution with antiphase spikes.

If the current pulse is too high or long, the network settles into an *on-off* state, in which either cell 1 or cell 2 spikes with a large amplitude, while the other oscillates about the rest state with very small amplitude, as the spiking cell strongly inhibits it. These *on-off* fixed points are small perturbations of the original fixed points for slow mutual inhibition which persist (as they should according to invariant manifold

theory). The synchronous bursting solution is a new stable solution for mutual inhibition with mixed time scales. We have numerically confirmed that the burst solution is stable. Brief current pulses (pulse widths less than τ_q) do not affect the bursting solution. Longer pulses switch the network to an *on-off* state depending on the cell to which the current pulse is applied. The network can also be switched from the *on-off* state to a bursting state. The burst state is characterized by slow growing oscillations before the onset and slow damped oscillations upon the termination of the active phase. The frequency of the oscillations along the burst remains nearly constant. This pattern of active phase oscillations differs from the active phase oscillations for square wave bursting, where the frequency decreases logarithmically as the slow parameter approaches the homoclinic orbit. Also, there is no delay in the last spike in the active phase, unlike the square wave burster.

Extensive numerical simulations show that the synchronous bursting solution has $q_1 \sim q_2$. We recall a similar dynamics for the slow variables for coupled square wave bursters, and use the same geometrical method [110, 62] to analyze bursting in Eqns. 4.27-4.30. Since the slow variables q_i are of $\mathcal{O}(1/\tau_s)$ close, we can treat them as identical. Therefore, we can construct a one parameter bifurcation diagram for the coupled fast subsystem (Figure 4.8).

We can use this picture to understand the nature of bursting geometrically. The fast inhibition introduces a second Hopf bifurcation from the steady state which represents anti-phase oscillations of the two cells. The anti-phase Hopf bifurcation of the network is subcritical, similar to the subcritical Hopf bifurcation in a single cell driven by a slow unidirectional synapse. We recall that fast inhibition for the HH network (Figure 4.4) has a stable antiphase solution. Hence, the spikes within the burst are π radians out of phase. Initially, as the external current drives the two cells from rest, they begin to oscillate since the slow inhibition is zero. The

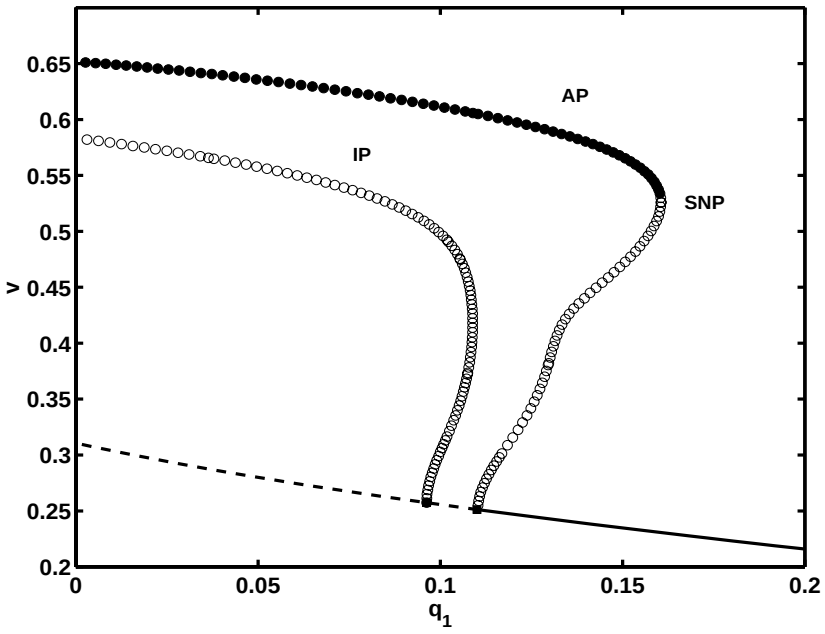

Figure 4.8. Bifurcation diagram for the fast subsystem of Eqns. 4.27-4.30. The symbols are as before. The parameter values have been slightly shifted to move the in-phase Hopf bifurcation to $q_1 = 0.096$. AP denotes the anti-phase branch, IP denotes the in-phase branch and SNP denotes the Saddle Node of Periodics.

activity of the cells causes the slow inhibition to increase and the cells track the stable periodic branch. As q_i crosses the saddle-node-of-periodics point (where the stability of the periodic solution changes), the rest state becomes the only stable state and the oscillations terminate. Now the synaptic variables begin to decrease slowly as the voltage switches below the q_i nullcline and the cells track the steady state branch. Interestingly, the slow ramping of the control variable (in this case, the synaptic variable) causes the cells to track the steady state even when it has lost stability, due to the delayed loss of stability at the Hopf bifurcation [68, 111]. A small noise term (uniformly distributed between $[-0.005,0.005]$) added to the voltage equations causes the cells to leave the rest state and jump to the unstable in-phase oscillation branch. As q_i begins to increase, the oscillators now track the stable anti-phase branch and the burst cycle repeats. This type of bursting, which starts at a subcritical Hopf point and ends at a saddle-node of periodics is termed type III bursting [112], and is characterized by slow ramping and small growing and damped oscillations prior to and after the active phase (Figure 4.9).

The burst solution is remarkable because the analysis of the averaged equations do not predict it. If we repeat the graphical construction in Figure 4.6, the only intersections of stable branches are the *on-off* states. Moreover, neither cell is an endogenous burster. Bursting is peculiar to the coupled network with mixed time scales. This network illustrates that synchronous solutions are possible in networks with inhibitory synapses, contrary to the usual dogma that inhibition leads to antiphase solutions. van Wreeswijk *et al.* also studied a model network of integrate and fire neurons (Type I oscillators according to the terminology of Section 3.3) and showed that fast, mutual inhibition led to synchrony in the network. However, their conclusions were based on the fact that the coupling strength was weak, and the methods of Section 3.3 apply [113]. Wang and Rinzel [104] studied the case

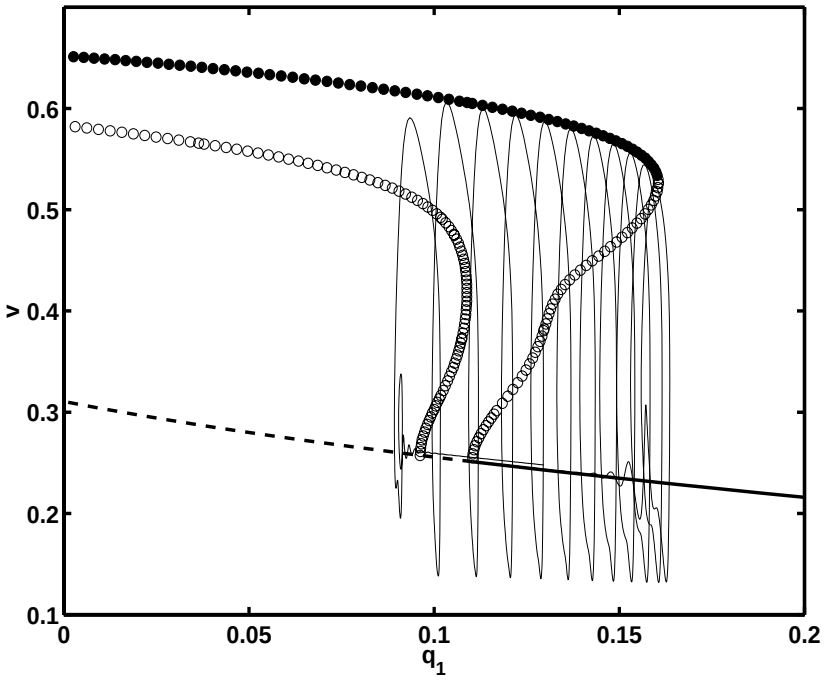

Figure 4.9. A phase portrait of the bursting trajectory for cell 1 overlaid on the bifurcation diagram.

of a network with slow inhibition which also synchronized. Terman *et al.* clarified the mechanisms of synchrony due to slow inhibition in relaxation oscillators. However, our model is remarkable in that it requires a mixed fast-slow inhibition for synchronization. The fast spike generating currents are as important as the slow averaged variables. Though, we have inferred the stability of the bursting solution numerically, we do not have a proof along the lines of Terman's [114] proof of a stable bursting solution for a square wave burster. The high dimensionality of the equations and the strong nonlinearity of the terms make any analytic progress difficult.

We might be able to address some questions concerning the stability of these bursts by constructing a simplified, canonical form for the full equations. The bifurcation diagrams clearly indicate that the subcritical Hopf bifurcation governs the bursting dynamics. Thus we can study the dynamics of the network by considering the normal forms for a subcritical Hopf bifurcation. We can use a theorem of Hoppensteadt and Izhikevich [98] to show that the equations can be written as:

$$\begin{aligned} z_i' &= (b_i + A_i v_j) z_i + d_i z_i |z_i|^2 + \sum_{j=1}^{n} c_{ij} z_j + \text{nonlinear coupling terms} \\ &\quad + \mathcal{O}(\varepsilon), \end{aligned} \tag{4.32}$$

$$v_i' = \hat{\mu}(R_i + S_i |z_i|^2 + T_i v_i) + \mathcal{O}(\hat{\mu}\varepsilon), \tag{4.33}$$

where $z_i \in \mathbb{C}$, $v_i \in \mathbb{R}$, b_i, c_{ij}, d_i, and A_i are complex coefficients. R_i, T_i, S_i are real matrices, and $\hat{\mu} = \mu/\varepsilon$. Kuramoto [74] and Aronson *et al.* [73] have formally outlined the reduction procedure that transforms a vector field near a Hopf bifurcation to the z equation which can be used to calculate the coefficients for Eqns. 4.27-4.30. This reduction results in a canonical form for a Hopf bifurcation, where the bifurcation parameter v_i is fixed. If $\mu \sim \mathcal{O}(\varepsilon^k)$, $\hat{\mu} \ll 1$, and v_i varies slowly and consequently, Eqns. 4.32-4.33 is singularly perturbed. The coupling terms must take into account

that the synaptic interaction has nonlinear components that enter into the equation at $\mathcal{O}(\sqrt{\varepsilon})$. Note that the bifurcation parameter for z_i is the slow variable v_j, as for the slow synapses. Since the bifurcation is subcritical, the rest state and the oscillations are bistable for a range of v_i. Frankel and Kiemel [102] considered a model of slowly coupled oscillators, similar to the normal form equations, with coupling only via the slow variables and showed that the generic solutions are either phase locked or phase trapped ones. However, their model did not include the fast coupling terms and they did not study the case of singular perturbations, although they did correctly include the amplitude effects for weakly coupled oscillators.

As we increase the coupling strength associated with the fast inhibition, we see a qualitative change in the oscillations. The periodic bursting solution is no longer stable, and the oscillators irregularly alternate between episodes of antiphase spiking and in-phase bursting with anti-phase spikes (Figure 4.10) . The length of the episodes appears to be chaotic. There is a narrow region of parameters where the two cells spike continuously rather than burst. The mechanism of transition to irregular bursting for this network is not clear.

A commonly observed feature in CPG networks is the lack of mutual, chemical excitation between cells. Excitatory chemical synapses are usually unidirectional. Instead, gap junctions or electrical coupling provide mutual excitation. One example of a mixed electrical and slow inhibitory synaptic coupling is in the cells of the somatogastric ganglion of the lobster, which controls the rhythmic movement of the internal teeth that masticate food in the animal's foregut [6]. Abarbanel *et al.* have studied a network of intrinsic bursters with electrical and instantaneous, inhibitory chemical coupling. We can extend our model by incorporating an electrical coupling term and leaving out the fast inhibitory synapse. The HH equations with mutual, electrical coupling have parameter regimes where both the in-phase and anti-phase

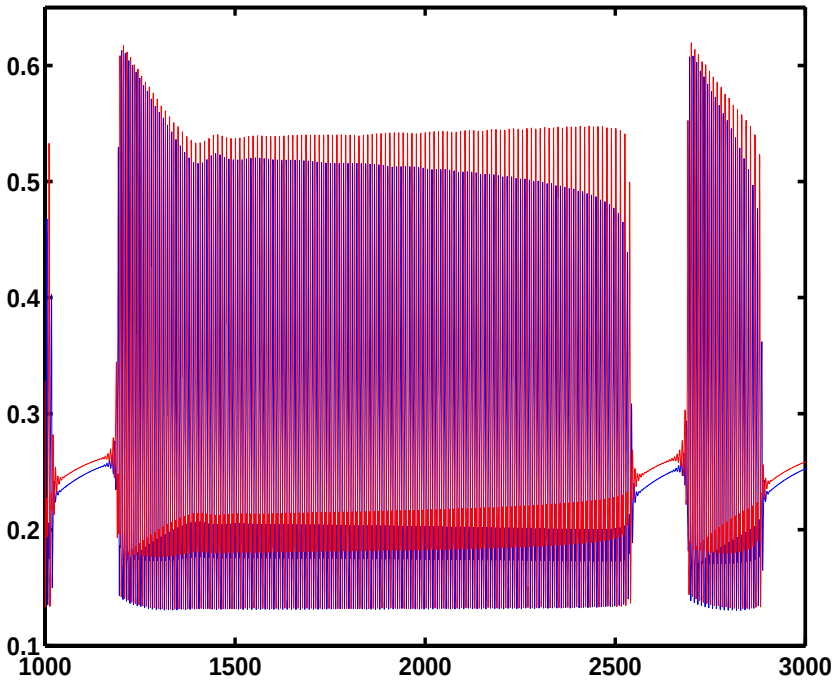

Figure 4.10. Irregular alternation between antiphase spiking and in-phase bursting for g_{ji}=0.06

solutions are simulataneously stable, which should lead to interesting dynamics for the network.

A model network of HH neurons with gap junctions replacing the fast inhibition also shows qualitatively similar behavior to the network with mixed inhibitory synapses. The synchronous bursting state persists, with somewhat enlarged stability boundaries. The spikes within the burst are in-phase, unlike in the network with fast inhibition. The duration of the active phase is shorter, with 5-6 spikes per burst. Also, large gap junctional coupling does not lead to chaotic bursting behavior.

Finally, we note that we have completely left out the case of mixed, mutual excitation, which does not occur in CPG networks, but is widespread in the cortex of mammalian brains. Pyramidal cells in the cortex are make fast (AMPA) and slow (NMDA) synapses onto the same targets [**?**]. However, NMDA synapses are much more complex than their faster AMPA couterparts. In addition to the aforementioned voltage dependence (pre and postsynaptic), NMDA synapses also open slow calcium channels in the post-synaptic cell, which completely change its excitability and firing characteristics. The slow activation kinetics of the Ca^{2+} channels result in a steady depolarized membrane voltage, that leads to repetitive bursting which has been observed experimentally. NMDA mediated bursting is a new class of coupling induced bursting, whose characterization must include the complex Ca^{2+} kinetics of the cell. Traven *et al.* [105] simulated a network with unidirectional NMDA and AMPA type synapses, and showed that the post-synaptic cell does indeed burst repetitively, and the number of spikes in a burst is related to the NMDA activation kinetics.

Most neurons in CPG networks are much more complicated than the simple Hodgkin-Huxley type model considered here, with additional slow currents and spatial properties. The spatial effects of dendrites must be studied using coupled PDE-

ODE systems, which makes analytic solutions very hard to come by, as dendritic proerties of neurons are not completely classified experimentally. The slow currents are more amenable to analysis. Two typical slow currents in CPG neurons are the "sag" current, which activates when the membrane is hyperpolarized, and the T-type calcium current, which allows the neuron to fire upon release from inhibition. Both these currents have slow activation variables, allowing the use of singular perturbation methods for their analysis. These models are usually simplified by including only the slow currents, while the slow and fast synaptic interactions are retained, by implicitly assuming that the averaging fast, spike generating variables is legitimate [115, 116, 117]. While averaging techniques can reduce biophysical models such as the HH model to a Hopfield like description, it can also mask potentially interesting dynamical modes of the network. Averaged approximations are qualitatively accurate however, if interactions between neurons have only a single time scale.

Finally, we note that even though the CPGs operate autonomously, they are under the control of external influences through the influence of chemicals called neuromodulators [95]. These chemicals, such as acetylcholine, serotonin or adrenaline alter the intrinsic and synaptic properties of CPG neurons (as well as cortical neurons). This level of control renders the temporal patterns of CPGs labile, and several different temporal patterns can be established, without any extensive rewiring of the circuits. A simple example of neuromodulation in our model would be a chemical that altered the strength of the fast synapse, switching the network from a bursting to an *on-off* mode or changing the length of the bursts.

CHAPTER 5

CONCLUSIONS AND OUTLOOK

5.1 Coupled Logistic Maps

The study of randomly coupled maps has not received much attention in the literature. We have studied a coupled logistic map that interpolates smoothly between the locally coupled and the globally coupled regimes. The observation that the dendritic structure of neurons is fractal over a certain spatial length scale which implies that the connection architecture is scale invariant, motivates this connectivity. So we now have an additional control parameter, the connectivity exponent.

As the connectivity increases, the lattice undergoes a transition from a disordered state to a globally synchronous state due to the appearance of a gap in the eigenvalue spectrum of the connectivity matrix. We explained the origin of this gap using theorems from stochastic matrix theory and the eigenvalue statistics of random matrices. The fractally coupled network of logistic maps also exhibits macroscopic order, with the appearance of low dimensional collective motion of the mean field. The collective motion of the mean field, $\langle x_i \rangle$, implies that the dynamics of the individual elements is no longer ergodic.

While we have discussed networks with discrete time dynamics, we expect that most of these results also hold for continuous time dynamics as well. For example, a Rössler oscillator could govern the flow of each site instead of the logistic map. A sufficient condition for synchrony in a network of chaotic continuous time oscillators

is that the product of the Lyapunov exponent of the local oscillator and the second largest eigenvalue of the connectivity matrix be less than 1. Further analysis of macroscopic behavior of these continuous time networks should reveal interesting features.

Brunnet *et al.* [118] have studied a large two-dimensional sheet of diffusively coupled Rössler oscillators and found signatures of collective behavior. Pikovsky *et al.* [119] have shown that a globally coupled population of non-identical Rossler oscillators frequency locks as the coupling strength is increased. We would expect similar frequency locking for our fractally coupled model, although this hypothesis remains to be checked.

Nontrivial, low dimensional collective motion in spatially extended models has attracted considerable interest recently. A careful characterization of the low dimensional attractors of the fractal network holds much promise for clarifying the relationship between connectivity and macroscopic dynamics of a network of identical, coupled dynamical elements.

We showed that the synchronization transition crucially depends on the distribution of the eigenvalues of the connectivity matrix that is drawn from a particular sparse random matrix ensemble (SRME). A comprehensive study of the eigenvalue statistics of the SRME would be useful for our understanding of dynamics of spatially structured networks.

5.2 Diffusively Coupled Bursters

We analyzed the dynamics of coupled square wave bursters using bifurcation methods and singular perturbation theory to clarify the role of gap junctional (or diffusive) coupling for models of bursting. We analyzed a simple, polynomial model for bursting using methods developed by Sherman [62] for analyzing a related model of

coupled bursters. Our geometrical approach was only applicable for weak coupling, where the slow variables of the single bursters are close for all time.

We proposed that the generic types of solutions near the Hopf bifurcations can be inferred from an analysis of the coupled fast subsystems alone. Differences in the slow parameters can be incorporated in this framework, which would be a possible extension to our analysis. Aronson *et al.* [73] have analyzed a similar model of coupled oscillators, with a different type of coupling and showed that exotic solutions exist, where one or both oscillators cease to oscillate as the unstable rest state becomes stable. The polynomial model of bursting has many other types of bursting solutions, in addition to square wave bursting, which are seen experimentally. The geometric approach can be applied to understand the nature of bursting in coupled networks to different types of burst solutions.

We studied a spatially extended model of coupled bursters to study the effect of experimentally measured gap-junction strengths on the oscillations. We showed that singular perturbation methods reduce the continuum model to a reaction-diffusion equation, with a slowly varying parameter. The reaction-diffusion equation is bistable between a limit cycle (the active phase oscillations of the burst) and a low voltage, rest state. Spatial diffusion of the voltage abolishes the burst oscillations, replacing them with a high voltage plateau. Notably, in variance with recent results of Argentina and Coullet [3], who studied a similar model, we do not find spatiotemporal chaos in the fast subsystem. These results are generic for most bursting models with one slow variable.

5.3 Weakly Coupled Neural Oscillators

We have analyzed a network of biophysically modeled neurons with reciprocal inhibition on two time scales, to understand how the rates of onset and decay of

inhibition interact with the intrinsic oscillations of the neurons to produce complex temporal patterns. For coupled neural oscillators, conventional views suggest that excitation promotes synchrony while inhibition leads to antiphase behavior. This view is in variance with several recent studies, which suggest that the time scale of the onset and decay of inhibition determines whether synchrony or anti-phase behavior is possible.

Our model of coupled neural oscillators with mixed time scales highlights some important features of real neural networks where synapses operate on multiple time scales. CPGs critically depend on delicately balanced phase relationships between different neurons in the network. The component neurons of these CPG networks are usually more complex than the neurons we have considered, with several additional slow currents present. A important extension of our work with H-H neurons would be to study the interplay between the fast dynamics of the spike generation, and the slow dynamics of the synapses and the intrinsic currents.

The phase equation reduction of Section 3.3 is not restricted to a small network of oscillators, and can be extended to model large, randomly coupled networks as well as spatially structured populations of coupled oscillators. Ermentrout has proved some basic results for discrete and continuum arrays of phase oscillators [120], but did not explore the case of random connectivity. Crook [121] has applied some of Ermentrout's results to an array of model cortical excitatory neurons. It would be interesting to apply some of the results of Chapter 1 to study networks of weakly coupled neurons with fractal connectvity.

BIBLIOGRAPHY

[1] E. Doedel, Cong. Num **30**, 265 (1981).

[2] J. Rinzel and X.-J. Wang, in *The Handbook of Brain Theory and Neural Networks*, edited by M. A. Arbib (MIT Press, Cambridge, Cambridge, MA, 1995), pp. 686–691.

[3] M. Argentina and P. Coullet, Phys. Rev. E **56**, R2359 (1997).

[4] C. Huygens, in *Oeuvrès Complètes de Christian Huygens*, edited by M. Nijhoff (Société Hollandaise des Sciences, Amsterdam, 1893), Vol. 5.

[5] A. Goldbeter, *Biochemical Oscillations and Cellular Rhythms* (Cambridge University Press, Cambridge, 1996).

[6] R. M. Harris-Warrick, E. Marder, M. Moulins, and A. Selverston, *Dynamic Biological Networks: The Stomatogastric Nervous System* (MIT Press, Cambridge MA, 1992).

[7] R. May, Nature (London) **261**, 459 (1976).

[8] H. Goldstein, *Classical Mechanics* (Addison Wesley, New York, 1980).

[9] J. Guckenheimer and P. Holmes, *Nonlinear Oscillations, Dynamical Systems and Bifurcations of Vector Fields*, Vol. 42 of *Springer Series in Applied Mathematical Sciences* (Springer-Verlag, Berlin, 1983).

[10] H. Bai-lin, *Elementary Symbolic Dynamics* (World Scientific, Singapore, 1988).

[11] G. Iooss, *Bifurcation of Maps and Applications* (North Holland, London, 1979).

[12] P. Manneville, *Dissipative Structures and Weak Turbulence* (Prentice-Hall, New York, 1990).

[13] K. Kaneko, in *Theory and Applications of Coupled Map Lattices*, edited by K. Kaneko (John Wiley, New York, 1994), pp. 1–50.

[14] R. Kapral, in *Theory and Applications of Coupled Map Lattices*, edited by K. Kaneko (John Wiley, New York, 1994), pp. 135–168.

[15] Y. Oono and S. Puri, Phys. Rev. Lett. **58**, 836 (1986).

[16] J. Miller and D. A. Huse, Phys. Rev. E **48**, 2528 (1993).

[17] V. S. Afraimovich and M. I. Rabinovich, in *Theory and Applications of Coupled Map Lattices*, edited by K. Kaneko (John Wiley, New York, 1994), pp. 117–134.

[18] P. Hadley, M. Beasley, and K. Weisenfeld, Phys. Rev. B **38**, 8712 (1988).

[19] S. H. Strogatz, C. H. Marcus, M. Westervelt, and R. E. Mirollo, Phys. Rev. Lett. **61**, 2380 (1988).

[20] K. Wiesenfeld, C. Bracikowski, G. James, and R. Roy, Phys. Rev. Lett. **65**, 1749 (1990).

[21] F. Mertens, R. Imbihl, and A. Mikhailov, J. Chem. Phys. **101**, 9903 (1994).

[22] K. Kaneko, Physica D **41**, 137 (1990).

[23] K. Kaneko, Phys. Rev. Lett. **63**, 219 (1989).

[24] M. Golubitsky and I. Stewart, *Bifurcations and Groups in Bifurcation Theory* (Springer-Verlag, Berlin, 1988).

[25] R. Eckhorn *et al.*, Biol. Cybern. **60**, 121 (1988).

[26] C. M. Gray and W. Singer, Proc. Natl. Acad. Sci. USA **86**, 1698 (1989).

[27] D. J. Felleman and D. C. van Essen, Cerebral Cortex **1**, 1 (1991).

[28] V. Braitenberg and A. Schüz, *Anatomy of the Cortex: Statistics and Geometry* (Springer-Verlag, Berlin, 1991).

[29] A. Schüz, in *The Handbook of Brain Theory and Neural Networks*, edited by M. A. Arbib (MIT Press, Cambridge, Cambridge, MA, 1995), pp. 622–626.

[30] A. Nicoll and C. Blakemore, Neural Comput. **5**, 665 (1993).

[31] F. Caserta *et al.*, Phys. Rev. Lett. **64**, 95 (1990).

[32] C. Mohr, S. Raghavachari, S. K. Boyd, and J. A. Glazier (unpublished).

[33] B. G. Szaro and R. Tompkins, J. Comp. Neurol. **258**, 304 (1987).

[34] C. Skarda and W. Freeman, Behav. Brain Sci. **10**, 161 (1987).

[35] T. Bohr, G. Grinstein, Y. He, and C. Jayaprakash, Phys. Rev. Lett. **58**, 2155 (1987).

[36] I. S. Aranson, D. Golomb, and H. Sompolinsky, Phys. Rev. Lett. **68**, 3495 (1992).

[37] H. Minc, *Nonnegative Matrices* (John Wiley, New York, 1988).

[38] H.-J. Sommers, A. Crisanti, H. Sompolinsky, and Y. Stein, Phys. Rev. Lett. **60**, 1895 (1988).

[39] P. M. Gade, Phys. Rev. E **54**, 64 (1996).

[40] P. Erdi and J. Toth, J. theor. Biol. **137**, 137 (1990).

[41] E. P. Wigner, in *Proceedings of the Fourth Canadian Mathematical Congress*, edited by R. S. MacPhail (University of Toronto Press, Toronto, 1959).

[42] R. M. May, Nature (London) **238**, 413 (1972).

[43] M. C. Cross and P. C. Hohenberg, Rev. Mod. Phys. **65**, 853 (1993).

[44] H. Chaté and P. Manneville, Prog. Theor. Phys. **87**, 1 (1992).

[45] N. Nakagawa and Y. Kuramoto, Prog. Theor. Phys. **89**, 313 (1993).

[46] V. Hakim and W.-J. Rappel, Phys. Rev. A **46**, R7347 (1992).

[47] K. Kaneko, Phys. Rev. Lett. **65**, 1391 (1990).

[48] A. S. Pikovsky and J. Kurths, Phys. Rev. Lett. **72**, 1644 (1994).

[49] M. Mezard, G. Parisi, and M. A. Virasoro, *Spin Glasses: Theory and Beyond* (World Scientific, Singapore, 1987).

[50] A. Crisanti, M. Falcioni, and A. Vulpiani, Phys. Rev. Lett. **76**, 612 (1996).

[51] D. J. Watts, Ph.D. thesis, Cornell University, 1997.

[52] H. Chaté and P. Manneville, Europhys. Lett. **14**, 409 (1991).

[53] J. Hemmingsson and H. J. Herrmann, Europhys. Lett. **23**, 15 (1993).

[54] J. Hemmingsson, A. Sorensen, H. Flyvbjerg, and H. J. Herrmann, Europhys. Lett. **23**, 629 (1993).

[55] H. Chaté, G. Grinstein, and L.-H. Tan, Phys. Rev. Lett. **74**, 912 (1995).

[56] N. Mousseau, Europhys. Lett. **33**, 509 (1996).

[57] S. Raghavchari, H. Chaté, and J. A. Glazier, 1998 (unpublished).

[58] G. M. Shepherd, *Neurobiology* (Oxford University Press, New York, 1994).

[59] E. R. Kandel and J. C. Schwartz, *Principles of Neural Science* (Elsevier, New York, YEAR).

[60] P. Getting, in *Methods in Neuronal Modeling*, edited by C. Koch and I. Segev (MIT Press, Cambridge, MA, 1988), pp. 191–194.

[61] A. L. Hodgkin and A. F. Huxley, J. Physiol. **117**, 500 (1952).

[62] A. Sherman, Bull. Math. Biol. **56**, 811 (1994).

[63] A. Sherman, J. Rinzel, and J. Keizer, Biophys. J. **54**, 411 (1988).

[64] S. Wiggins, *Intorduction to Applied Nonlinear Dynamical Systems and Chaos* (Springer-Verlag, Berlin, 1990).

[65] M. Pernarowski, SIAM J. Appl. Math **52**, 1627 (1992).

[66] G. de Vries, Ph.D. thesis, University of British Columbia, 1996.

[67] F. A. Salam, SIAM J. Appl. Math. **47**, 232 (1987).

[68] A. I. Nejshtadt, Diff. Eqns. **23**, 1385 .

[69] J. Guckenheimer (unpublished).

[70] R. J. Field and M. Burger, *Oscillations and Traveling Waves in Chemical Systems* (John Wiley, New York, 1985).

[71] M. Pernarowski, SIAM J. Appl. Math. **54**, 814 (1994).

[72] N. Fenichel, Indiana Univ. Math. J **21**, 193 (1971).

[73] D. G. Aronson, H. Othmer, and E. J. Doedel, Physica D **27**, 20 (1987).

[74] Y. Kuramoto, *Chemical Oscillations, Waves and Turbulence* (Springer-Verlag, Berlin, 1984).

[75] P. Smolen, J. Rinzel, and A. Sherman, Biophys. J. (1992).

[76] M. Perez-Armandriz, C. Roy, D. C. Spray, and M. V. L. Bennett, Biophys. J. **59**, 76 (1991).

[77] J. D. Murray, *Mathematical Biology* (Springer-Verlag, Berlin, 1993).

[78] P. Grindrod, *Patterns and Waves: The Theory and Applications of Reaction-Diffusion Equations* (Clarendon Press, Oxford, 1991).

[79] N. F. Britton, *Reaction-Diffusion Equations and Their Application to Biology* (Academic Press, London, 1986).

[80] W. van Saarloos and P. C. Hohenberg, Physica D **56**, 303 (1992).

[81] R. Kapral and K. Showalter, .

[82] G. B. Ermentrout, X. Chen, and Z. Chen, Physica D **108**, 147 (1997).

[83] E. Ben-Jacob *et al.*, Physica D **14**, 348 (1985).

[84] J. H. Merkin, V. Petrov, S. K. Scott, and K. Showalter, Phys. Rev. Lett. **76**, 546 (1996).

[85] H. Chaté, Nonlinearity **7**, 185 (1994).

[86] J. L. Hindmarsh and R. M. Rose, Proc. Roy. Soc. London B **221**, 87 (1984).

[87] B. Shraiman *et al.*, Physica D **57**, 241 (1992).

[88] S. K. Han, C. Kurrer, and Y. Kuramoto, Phys. Rev. Lett. **75**, 3190 (1995).

[89] M. Pernarowski, SIAM J. Appl. Math. (in press). (1998).

[90] X.-J. Wang, Physica D **62**, 263 (1993).

[91] F. Dumortier, R. Roussarie, J. Sotomayor, and H. Zoladek, *Bifurcations of Planar Vector Fields: Nilpotent Singularities and Abelian Integrals*, Vol. 1480 of *Lecture Notes in Mathematics* (Springer Verlag, Berlin, 1991).

[92] .

[93] J. Tuckwell, *Mathematical Neurobiology* (Cambridge Press, Cambridge, 1987).

[94] A. Destexhe, Z. Mainen, and T. Sejnowski, J. Comput. Neurosci. **1**, 195 (1994).

[95] E. Marder, in *The Crustacean Stomatogastric Nervous System*, edited by A. I. Selverston and M. Moulton (Springer-Verlag, Berlin, 1987), pp. 263–300.

[96] J. A. Glazier and A. Libchaber, IEEE Trans. Circuits and Systems **35**, 790 (1988).

[97] G. B. Ermentrout and N. Kopell, J. Math. Biol. **29**, 195 (1991).

[98] F. Hoppensteadt and E. M. Izhikevich, *Weakly Connected Neural Networks* (Springer Verlag, Berlin, 1997).

[99] G. B. Ermentrout, in *Neural Modeling and Neural Networks*, edited by F. Ventriglia (Pergammon Press, Oxford, 1993), pp. 79–110.

[100] D. Hansel, G. Mato, and C. Meunier, Europhys. Lett. **23**, 367 (1993).

[101] L. Abbott and C. vanWreeswijk, Phys. Rev. E **48**, 1483 (1993).

[102] P. Frankel and T. Kiemel, SIAM J. Appl. Math. **53**, 1436 (1993).

[103] P. Getting, Annu. Rev. Neurosci. **12**, 185 (1989).

[104] X.-J. Wang and J. Rinzel, Neural. Comput. **4**, 84 (1992).

[105] H. G. Traven *et al.*, J. Neurophysiol. **70**, 695 (1993).

[106] D. Perkel and B. Mulloney, Science **200**, 181 (1974).

[107] S. Nurse and J. C. Lacaille, Can. J. Physiol. Pharmacol. **75**, 520 (1997).

[108] R. C. Elson and A. I. Selverston, J. Neurophysiol. **74**, 1996 (1995).

[109] J. Rinzel and P. Frankel, Neural. Comput. **4**, 534 (1992).

[110] J. Rinzel and Y. S. Lee, in *Mathematical Topics in Population Biology, Morphogenesis and Neurosciences*, Vol. 66 of *Lecture Notes in Biomathematics*, edited by H. G. Othmer (Springer-Verlag, Berlin, 1986), pp. 19–33.

[111] S. M. Baer, T. Erneux, and J. Rinzel, SIAM J. Appl. Math. **49**, 55 (1989).

[112] R. Bertram, M. J. Butte, T. Kiemel, and A. Sherman, Bull. Math. Biol. **57**, 413 (1995).

[113] G. B. Ermentrout, Neural Comput. **8**, 979 (1996).

[114] D. Terman, SIAM J. Appl. Math. **51**, 1418 (1991).

[115] X.-J. Wang and J. Rinzel, Neuroscience **53**, 899 (1993).

[116] D. Golomb, X.-J. Wang, and J. Rinzel, J. Neurophysiol. **72**, (1994).

[117] D. Terman, N. Kopell, and A. Bose, Physica D **57**, 252 (1998).

[118] L. Brunnet, H. Chaté, and P. Manneville, Physica D **78**, 141 (1994).

[119] A. S. Pikovsky, M. G. Rosenblum, and J. Kurths, Europhys. Lett. **34**, 165 (1996).

[120] G. B. Ermentrout, SIAM J. Appl. Math. **52**, 1665 (1992).

[121] S. M. Crook, Ph.D. thesis, Univeristy of Maryland, 1996.

APPENDIX A

This section contains the rate functions for the Hodgkin-Huxley equation (Chapter 2), the SRK equation (Chapter 2) and the modified Hodgkin-Huxley equation (Chapter 3).

The Hodgkin-Huxley Model

The Hodgkin-Huxley equations are:

$$C_m \frac{dV}{dt} = -g_{Na} m^3 h(V - V_{Na}) - g_K n^4 (V - V_K) - g_{leak}(V - v_{leak}) + I_{app}, \quad (1)$$

$$\frac{dm}{dt} = \frac{(m_\infty(V) - m)}{\tau_m(V)}, \quad (2)$$

$$\frac{dh}{dt} = \frac{(h_\infty(V) - h)}{\tau_h(V)}, \quad (3)$$

$$\frac{dn}{dt} = \frac{(n_\infty(V) - n)}{\tau_n(V)}. \quad (4)$$

The rate functions $x_\infty(V),\ \tau_x(V),\ x = m, h, n$ are:

$$\alpha_m(V) = 0.1\frac{V+40}{1-\exp(-(V+40)/10)}, \tag{5}$$

$$\beta_m(V) = 4\exp(-(V+65)/10), \tag{6}$$

$$m_\infty(V) = \frac{1}{1+\alpha_m(V)/\beta_m(V)}, \tag{7}$$

$$\tau_m(V) = \frac{1}{\alpha_m(V)+\beta_m(V)}, \tag{8}$$

$$\alpha_h(V) = 0.07\exp(-(V+65)/20), \tag{9}$$

$$\beta_h(V) = \frac{1}{1+\exp(-(V+35)/10)}, \tag{10}$$

$$h_\infty(V) = \frac{1}{1+\alpha_h(V)/\beta_h(V)}, \tag{11}$$

$$\tau_h(V) = \frac{1}{\alpha_h(V)+\beta_h(V)}, \tag{12}$$

$$\alpha_n(V) = 0.01\frac{V+55}{1-\exp(-(V+55)/10)}, \tag{13}$$

$$\beta_n(V) = 0.125\exp(-(V+65)/80), \tag{14}$$

$$n_\infty(V) = \frac{1}{1+\alpha_n(V)/\beta_n(V)}, \tag{15}$$

$$\tau_n(V) = \frac{1}{\alpha_n(V)+\beta_n(V)}. \tag{16}$$

The parameters are $g_{\bar{Na}} = 120$ mS/cm^2, $g_{\bar{K}} = 36$ mS/cm^2, $g_{Leak} = 0.3$mS/cm^2, $C = 1$ μF/cm^2. $V_K = -77$ mV, $V_{Na} = 50$ mV, and $V_{Leak} = -54.4$mV.

Modified Sherman-Rinzel-Keizer Model

The SRK equations are:

$$\tau\frac{dV}{dt} = -g_{Ca}m_\infty(V)(V-V_{Ca}) - g_K n(V-V_K) - g_S S(V-V_K), \tag{17}$$

$$\frac{dn}{dt} = \frac{n_\infty(V)-n}{\tau_n}, \tag{18}$$

$$\frac{dS}{dt} = \beta\frac{S_\infty - S}{\tau_S}. \tag{19}$$

The rate functions are given by:

$$m_\infty(V) = \frac{1}{1+\exp((-20-V)/12)}, \tag{20}$$

$$n_\infty(V) = \frac{1}{1+\exp((-16-V)/5.6)}, \tag{21}$$

$$S_\infty(V) = \frac{1}{1+\exp((-45-V)/10)}. \tag{22}$$

The parameter values are (in non-dimensional units) $g_{Ca} = 3.6$, $g_K = 10$, and $g_S = 4$, $\beta = 1$.

Modified Hodgkin-Huxley Equations

The modified HH equations are obtained by setting the Na activation and inactivation to be instantaneous. The voltage dependent time constant for the potassium activation n is modified, and the voltages are divided by the Na reversal potential. The equations are:

$$\begin{aligned}\frac{dv}{dt} &= -I_{ion}(v_i, n_i) - g_{ji}s_j(v_i - V_{syn}) \\ &\quad - g'_{ji}q_j(v_i - V'_{syn}) + I_{app}\end{aligned} \tag{23}$$

$$\frac{dn}{dt} = \frac{n_\infty(v) - n}{\tau(v)} \tag{24}$$

$$\frac{ds}{dt} = \frac{s_\infty(v) - s}{\tau_s} \tag{25}$$

$$\frac{dq}{dt} = \frac{q_\infty(v) - q}{\tau_q}, \tag{26}$$

with $I_{ion} = g_{Na}m^3_\infty(v)(v - v_{Na}) + g_K n^4(v - v_K) + g_L(v - v_L)$. The rate functions are:

$$m_\infty(v) = \frac{1}{1+\exp((0.3-v)/0.12)}, \tag{27}$$

$$n_\infty(v) = \frac{1}{1+\exp((0.1-v)/0.10)}, \tag{28}$$

$$\tau_n(V) = \frac{\bar{\tau_n}}{\cosh((0.2-v)/0.3)}, \tag{29}$$

$$s_\infty(v) = \frac{1}{1+\exp(2(0.43-v)/0.12)}, \tag{30}$$

$$q_\infty(v) = \frac{1}{1+\exp(2(0.43-v)/0.12)}. \tag{31}$$

The parameter values are $g_{Na} = 4$, $g_K = 4$, $g_L = 0.0333$, $g'_{ji} = 5.55556$, $V_{syn} = V'_{syn} = -0.1$, and $\bar{\tau_n} = 4.5$.

The particular choice results in a subcritical Hopf bifurcation and a current-frequency relation similar to the full HH equations.